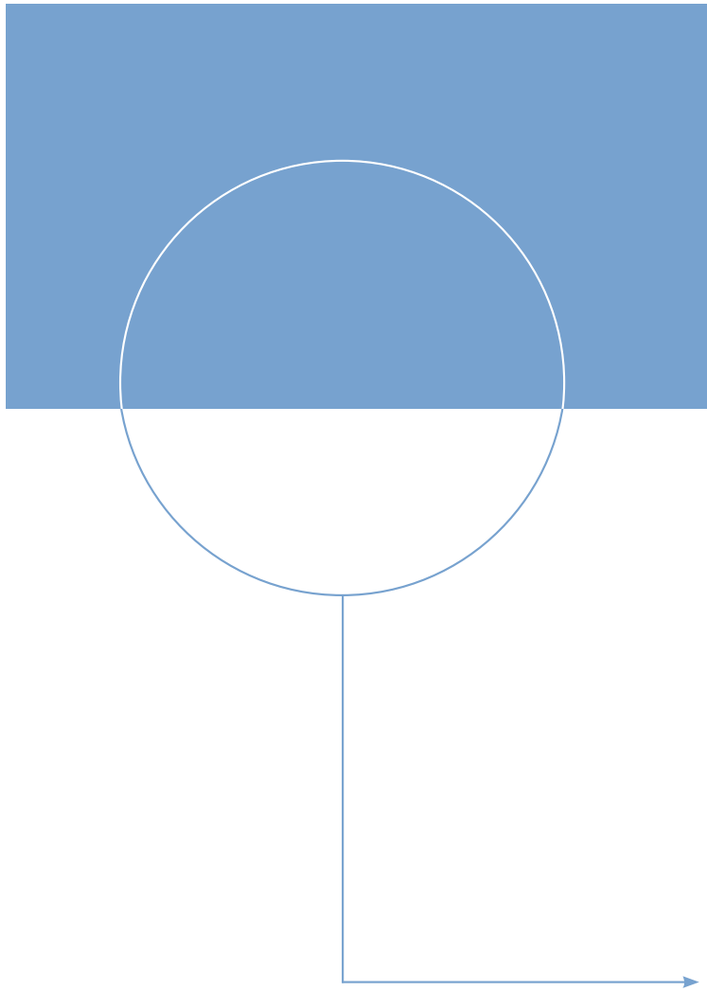

Master's thesis

2019

Diogo dos Santos Silva

NTNU
Norwegian University of
Science and Technology
Faculty of Information Technology and Electrical
Engineering
Department of Electric Power Engineering

Diogo dos Santos Silva

A DC-Grid Proposal for Deep Sea Mining Focusing on Power Quality Aspects

July 2019

NTNU
Norwegian University of
Science and Technology

NTNU
Norwegian University of
Science and Technology

NTNU

Norwegian University of
Science and Technology

A DC-Grid Proposal for Deep Sea Mining Focusing on Power Quality Aspects

Diogo dos Santos Silva

Energy and Environmental Engineering
Submission date: July 2019
Supervisor: Elisabetta Tedeschi
Co-supervisor: Santiago Sanchez Acevedo

Norwegian University of Science and Technology
Department of Electric Power Engineering

NTNU – Trondheim
Norwegian University of
Science and Technology

A DC-Grid Proposal for Deep Sea Mining focusing on Power Quality Aspects

Diogo dos Santos Silva

Master of Energy and Environmental Engineering
Submission Date: July 2019
Supervisor: Elisabetta Tedeschi
Co-Supervisor: Santiago Sanchez Acevedo

Department of Electrical Power Engineering
Norwegian University of Science and Technology

Summary

Over the last years, DC grids have become a significant trend topic as a solution for better power distribution systems reducing losses and increasing the efficiency significantly. The technology of HVDC transmission is a reality among wind farms far from land as well as the LVDC grids are under continuous development as an optimum solution for electrical ships reducing fuel consumption drastically.

Looking over these examples of success, the author in this thesis investigates the utilization of a radial DC grid to supply power to typical subsea loads employed by the embryonic, however promising, Deep Sea Mining industry.

The thesis briefly presents the benefits of this technology and appraises the main challenges related to power quality in the DC grids. The issue of harmonic DC currents, in the MVDC transmission, between topside and a subsea converter and in the subsea DC-bus are investigated in this thesis. The converters are connected back to back by a short distance umbilical cable. The focus of the modeling and simulation is, to evaluate the power quality aspects of the interaction between both converters, while the subsea converter maintains a stable DC voltage level for other subsea consumers.

The simulations are performed using the software MATLAB/Simulink. The base case takes into consideration a possible Deep Sea Mining application, where the entire spectrum of possible consumers, such as control systems and motor pumps, are concentrated as a single load fed by a subsea DC-DC converter. This converter shall provide a stable voltage, independently of fluctuations in the power transmission from topside.

The power system is modeled based on the disclosure information published by the company Nautilus Minerals. The subsea consumers are located at a maximum water depth of 3500 meters. However, the power transmission considered is 5000 m, enabling at least 1500 m locomotion to the mining vehicles. A topside converter is responsible for controlling the power to the subsea grid while the subsea converter is responsible for maintaining the voltage in the DC-link stable, assuring a secure operation of the mining vehicles. The results reveal that the line reactances installed upstream the topside converter can eliminate the DC-harmonics at high frequencies in the subsea DC-links while the passive LC filters have a marginal benefit regarding the harmonic

reduction in the DC-grid. They also expose that the voltage in the subsea DC-bus can be very stable if the voltage step-down is sufficiently high in the DC-DC converter.

Preface

This master thesis is my final assignment as a student at the Department of Electric Power Engineering at The Norwegian University of Science and Technology (NTNU). The project has been elaborated during the first semester of 2019 in Trondheim, Norway.

This master thesis has its origin in the specialization project from the fall of 2018. During the elaboration of specialization project, I had the opportunity to learn about the Deep Sea Mining technology, based on a literature review, when the knowledge regarding this technology has been consolidated. A power system topology has been proposed as the starting point for this thesis, and its power quality evaluated. The writing of this report has been found challenging. Due to time constraints sharing my days between work and academic life, and rewarding, due to the exponential learning process by reading and implementing several technical aspects in the simulation models. Building the entire simulation system by debugging each block at the time can be frustrating and tiresome eventually. However, observe the complete system working is a great achievement.

I want to state my gratefulness to the remarkable persons who assist me in concluding this report. Professor Elisabetta Tedeschi for her support and guidance during my entire final year as a student, Santiago Acevedo and Anders Holvik for assistance with modeling and troubleshooting of the Simulink model, and my friend and co-worker Beatrix Weiss which assist me both with report review and stability issues in the Simulink model. I shall also remember my lovely wife, Aloma Goda, who supports me even debilitated due to illness. And my adorable daughter Sofia Silva, to whom was deprived of my presence, much more than should have.

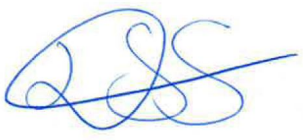

Trondheim, July 22th 2019
Diogo dos Santos Silva

Contents

List of Figures

List of Tables

Abbreviations

ABS	American Bureau of Shipping
AC	Alternating current
AuxC	Auxiliary Cutter
avg	average
BC	Bulk Cutter
CM	Collector Machine
DC	Direct current
DNV	Det Norske Veritas
DSM	Deep Sea Mining
EMC	Electromagnetic Compatibility
EMI	Electromagnetic Interference
FFT	Fast Fourier Transform
HV	High Voltage
IEC	International Electrotechnical Commission
IEEE	Institute of Electrical and Electronics Engineers
IGBT	Insulated Gate Bipolar Transistor
MV	Medium Voltage
pk-pk	peak-to-peak
PSV	Production Support Vessel
pu	Per-unit
PCB	Printed Circuit Board
PWM	Pulse Width Modulation
RALS	Riser and Lifting System
RMS	Root Mean Square
ROV	Remote Operated Vehicle
SCR	Silicon-Controlled Rectifier
SMS	Seafloor Massive Sulfides
SPT	Seafloor Production Tools
SSLP	Subsea Lift Pump
THD	Total Harmonic Distortion
UPS	Uninterrupted Power Systems
VSI	Voltage Source Inverter
VSC	Voltage Source Converter
VSD	Variable Speed Driver

Chapter 1

Introduction

1.1 Background and Motivation

The next industrial revolution will be hinged on the availability of metals and minerals indispensable for manufacturing of goods from smartphones to satellites. Anticipating that such raw materials will become rare overtime some nations, and pioneer enterprises, initiate projects to seek for minerals in the seafloor. Such emerging industry is called Deep Sea Mining (DSM).

Several academic essays and technical reports describe ideas to promote the feasibility of such exploration, reference [1] studies the feasibility of Deep Sea Mining (DSM) in the Norwegian Jurisdiction, [2] describes a concept based on flexible risers and self-propelled mining machines, while in [3] and [4] the experiences and plans for mining extraction of the company DeBeers are presented, and [4] also explains its plan to mineral extraction. However most of the actual projects are either under development or in prototyping test phase [5]. Nonetheless exploiting the seafloor to obtain minerals is not a straightforward task.

In order to achieve this accomplishment companies as Nautilus, in close cooperation with their partners, such as Soil Machine Dynamics, are developing Subsea Production Tools [6] capable to pre-treat, select and collect the mineral nodules to Production Support Vessel, and subsequently convey them to land.

The vehicles involved in DSM have a substantial power demand. The total minimum amount of power to operate the vehicles on the seabed is 6.3 MW [7] or 14.1 MW in case adding the Subsea Lift Pump (SSLP) as a subsea load. Moreover there are several options to bring the power to such machines on the seafloor. The authors in [9] investigate the possible configurations to the grid in order to supply power to the seafloor. The models concentrate the rationale on the arguments of having an AC or DC system, and how the power will be delivered to the seafloor.

Indeed, there are a few possibilities to deliver power to subsea mining vehicles, as explained

in [10] and [11]. The utilization of DC distribution systems makes it possible to overcome the issues faced by traditional AC grids in subsea applications. Such as excessive voltage drops on the power umbilicals, better power transfer capability, elimination of skin effects, and proximity effects, enhancing of voltage insulation capability for the same thickness of insulation in the cables, and elimination of reactive power.

1.2 Relation to Specialization Project

Throughout the second semester of 2018 the author of this thesis wrote a specialization project entitled "Power Quality Evaluation for Power System Design for Deep Sea Mining Application" [6] where the author performed a literature review to investigate the deep sea mining power demands, the power quality affecting the grid and which power system configuration would perform better regarding costs and viability.

1.3 Objective

The objectives of this master thesis are:

1. Propose and test a DC power system for DSM based on possible different topologies available in the literature, using the engineering tool Matlab/Simulink.
2. Evaluate the performance of the proposed system regarding the control system reaction when load disturbances occur.
3. Evaluate the power quality aspects in the grid, such as resonances, AC and DC harmonics.

1.4 Scope of the work and its limitation

In order to achieve the objectives mentioned above, this thesis will propose and implement the AC-DC and DC-DC converters and their control system. The topside system is modeled initially as a stiff source, and replaced by a "soft source" [34] posteriorly. The modeling of the generators is not be cover in this essay.

The power system consists of a radial system which converts the AC power to DC in the topside branch and distributes to subsea loads using DC power. The topside converter controls the active power while the subsea converter controls a constant voltage at the subsea DC-bus. The grid is modeled in Matlab/Simulink where the topside converter control is performed using two-level voltage source converter technique. The subsea converter is a step-down (buck) converter and its control uses PWM technique.

Once the system is modeled and stable, the deterioration of power quality and how it can affect the system is evaluated, in terms of both AC and DC harmonics. Abrupt variations in the load and the power quality for different power levels are also verified.

Despite aspects as short-circuit protection, circulating ground currents, and Electromagnetic Interference are related to power quality in DC-grids they will not be cover in this report.

1.5 Thesis Outline

This section shortly presents the content of each chapter.

- **Chapter 2** gives an overview of the concept of DSM, i.e. how the DSM system is expected to operate, what are the power consumption demand from the subsea loads, what type of electric loads will be employed, and the environmental boundaries and constraints.
- **Chapter 3** outlines the different aspects of AC and DC power distributions in the subsea environment which serves as a baseline to the selection of the topology to be employed in this thesis.
- **Chapter 4** describes how the single blocks of the power system are modelled in this essay, i.e. the converters, the power cable, the load and the source.
- **Chapter 5** explains why power quality issues are so relevant and introduces ways to solve them.
- **Chapter 6** depicts the results and discussions.
- **Chapter 7** presents the conclusion observed from the results and proposes future work.

Chapter 2

Deep Sea Mining Technology

The definition of deep sea mining technology has been done in details by the author in the reference [6]. The chapter 2 of this report aims to bring essential information related to this technology, enabling the reader to understand why the evaluation of power systems for DSM is deemed relevant.

2.1 Overview

The deep sea mining comprises the profiteering of seafloor searching for minerals in a similar process than the mineral exploration performed on land.

The raising of metal request and the reduction of metal grades are outstanding causes which motivate the deep sea mining industry foment, some supplementary reasons and opposing forces for marine mining are presented in [8] and summarized in table 2.1 from [6]

Table 2.1: Summary of the drivers for deep sea mining industry [6].

	Society	**Industry**
Primary drivers	- Global economic growth. - States securing access to resources, hence increase independence with respect to mineral supply.	- Innovative and risk tolerant actors. - Increasing difficulty and complexity of terrestrial mining.
Secondary drivers	- Increased focus on, and support to environment and social sustainability. - Emerging appliances and markets.	- Technological improvements and scalable applicability.

The subsea mining has benefits when comparing to land mining. The conveying of minerals by the seawater is more affordable regarding distribution; the pre-existed seaport facilities for

setting up supply hubs and delivery of mineral products; and has fewer expenditures of logistics during the onshore process thanks to the market nearness.

2.2 Minerals

There are three types of minerals with commercial interest in deep sea mining. More information regarding their characteristics can be obtained in [8], and; they are epitomized in [1] as showed below:

- "Seafloor massive sulfides (SMS) originate from active and extinct hydrothermal vents at mid-ocean ridges, intra-plate hotspots, and at plate boundaries including volcanic/island arcs and back-arc basins located at depths of 1500-5000 m [8] p. 12;
- Polymetallic nodules are rich in rare earth elements (REE), and are found on the seafloor at 4000-6000 m water depth;
- Cobalt-rich ferromanganese crusts are present at seamounts and around flanks of volcanic islands at 400-4000 m water depth."

Table 2.2: Showing the types of minerals and their characteristics [26].

Marine Mineral	**Typical water depth [m]**	**Characteristic Metals**
Seafloor massive sulfides (SMS)	1400 - 3700	Copper,Lead, Zinc, some Gold and Silver
Polymetallic nodules	4000 - 2400	Copper,Cobalt, Manganese and Nickel
Cobalt-rich ferromanganese crusts	800 - 2400	Mainly Cobalt, some Vanadium, Molybdenum and Platinum

2.3 Seafloor Production System

The mining processes both in subsea and in land use the same concept; they function with a stream of single unit operations, the downstream unit relies upon the unit located upstream. Thereby any potential fault in a unit will affect the complete process in that specific chain. To mitigate the impact of such incidents, it is critical that every single machine functions at high performance and utilizing its utmost capacity. This chain operation requires a clamped operation plan for the mining site, which will be analogous to the plan applied to open-pit sites, the four main stages required in this process are site settlement, slash and gather, transport, and clean-out.

The author explains in [6] that "*the subsea mining system is developed with the concept of disaggregating the minerals on the seafloor using excavators remotely operated from the topside*

system, before vertically transporting an ore-seawater slurry to the topside vessel. The slurry is dewatered, i.e., all solid particles are retained, and the mineral-rich ore is stored and later shipped to shore for further processing in a land facility."

Appurtenant references, such as the Nautilus Minerals reports [16], depict the Seafloor Production System in the ensuing components:

- Production Support Vessel (PSV)
- Riser and Lifting System (RALS), adding the Subsea Lift Pump (SSLP)
- Seafloor Production Tools (SPTs)

The SMS material will be scooped using SPTs; the metal will be bombed to the PSV as a mud via the lifting system. Aboard the PSV the mud is dewatered, and the solid particles discharged into massive ships for transportation to shore for additional treatment.

The Fig. 2.1 elucidates the components of the seafloor production system; all elements of the presented figure are described throughout this chapter.

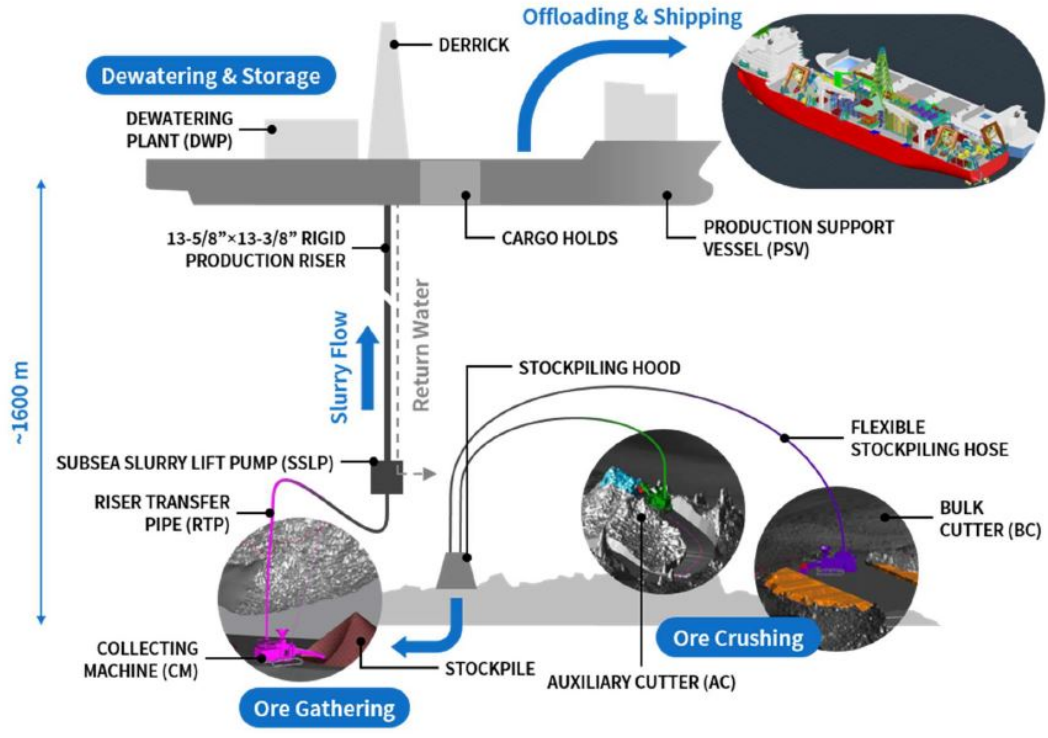

Figure 2.1: Seafloor resource production system [1].

2.4 Seafloor Production Tools

The SPTs are in charge of the excavation of the SMS deposits. The equipment uses the characteristics of world-class ROVs, with land mining well-known technology and the track shoes for locomotion. The enterprise Nautilus Minerals is one of the companies that has divulged more information concerning the SPTs designed to the company´s project, and thus their configuration will be used as the basis to develop the power system in this report.

The DSM process is resembling the land mining procedure. A movable and pliant machine prepares the mining zone followed by a devoted large production system [1]. Because of the topography (maximum 20° slopes) of the Solwara 1 project, the seabed operation is divided into three sequential tasks, and a dedicated vehicle performs each of them.

2.4.1 Auxiliary Cutter (AuxC)

As stated in [16], "the AuxC is a track-mounted primary rock cutting tool." The machine must prepare appropriated platforms for the Bulk Cutter operation. The equipment has the dimensions 16.4 m x 6.9 m x 7.6 m (L x W x H), the weight is around 250 t in the air. The AuxC is analogous in many aspects to the vehicles used in subsea pipeline trencher, operated by oil & gas industry. A 650 kW electric motor (direct drive) supplies power to the cutter's pump of the Auxiliary Cutter. The dredging system of the machine is designed to pump a 4.6 % mud with an outflow of 3206 m^3/h and can deliver up to 472 t per hour. The Auxiliary Cutter has the following functions, listed in [16]:

- "Remove sediments overlying mineralized rock by side casting.
- Cut ramps and stockpile areas.
- Prepare benches that are suitable for the bulk cutter.
- Remove edge sections of benches that cannot be accessed by the bulk cutter."

Aiming to accomplish its functions, the AuxC demands additional systems responsible for locomotion and positioning, communication, and sensors, all these systems along with the motor portrays a total power demand estimate of 2 MW [7]. The machine is depicted in the Fig. 2.2.

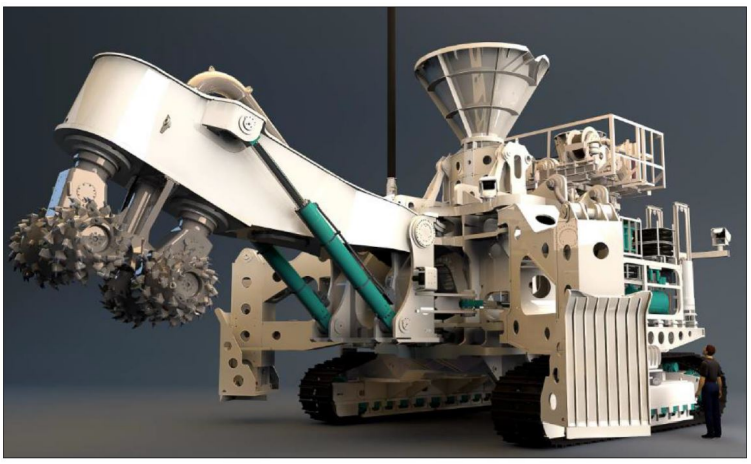

Figure 2.2: Auxiliary Cutter designed by the company SMD Ltd [16].

2.4.2 Bulk Cutter (BC)

The Bulk Cutter (BC) is equally a track-mounted rock cutting equipment. The BC is the main production unit. The machine has the dimensions 15.5 m x 4.2 m x 6.8 m (L x W x H), it has approximately 275 t in the air. The vehicle is able to track over soft ground and a substantial static bearing pressure of 300 kPa [16]. The BC employs a transversely orientated 4.2 m wide cylindrical drum. Two 600 kW electric motors supply power to the drum. The motors can deliver up to 900 kW together, of cutting power, by using two gearboxes that will be installed inside the cutter drum. The design of the drum has a restriction of cut rock capability of 100 MPa. Nonetheless, Nautilus report [16] states that the maximum hardness of SMS will be 52 MPa. The BC will operate in benches created by the AuxC. A collection drum will gather the excavated material with a grizzly device mechanism with a suction mechanism. A 650 kW electric motor supplies power the bulk cutter's pump. The dredge system of the vehicle is designed to pump a 4.6 % slurry with an outflow of 3,206 m^3/h providing up to 472 t per hour. The total power required for the BC is 2.5 MW [7]. The vehicle is shown in the Fig. 2.3.

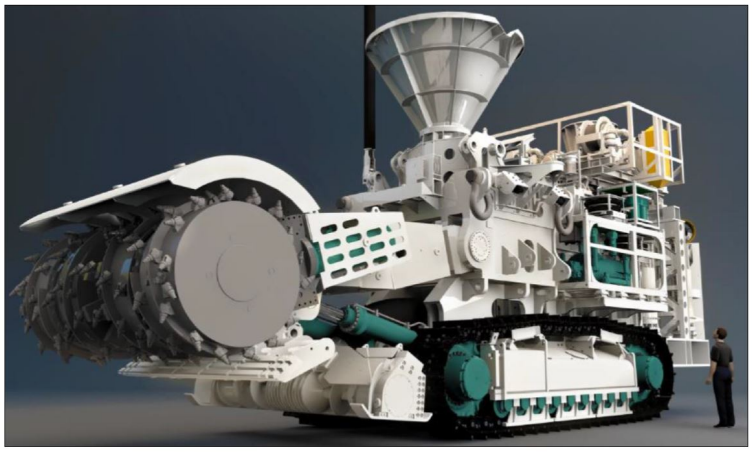

Figure 2.3: Bulk Cutter designed by the company SMD Ltd[16].

2.4.3 Collection Machine (CM)

The Collection Machine (CM) is equally a track-mounted machine; it recuperates splintered material from seabed stockpiles and bombs it in a mud form to the subsea slurry lift pump. The dimensions of the CM are 17 m x 6 m x 7.6 m (L x W x H) and the machine weights 185 t air approximately. Ian Lipton [16] clarifies that the CM is outfitted with a three-stage slurry pumping system, responsible for handing over the slurry to the subsea slurry lift pump. A 330 kW electric motor drives every handing over. Each motor has a drive, in principle topside, to regulate the pump flow and rotation speed. The CM possess a riser transfer pipe connected to it, responsible for transport the collected material to the subsea slurry lift pump. The estimated power demand from the Collection Machine is 1.8 MW [7]. Fig. 2.4 shows the machine.

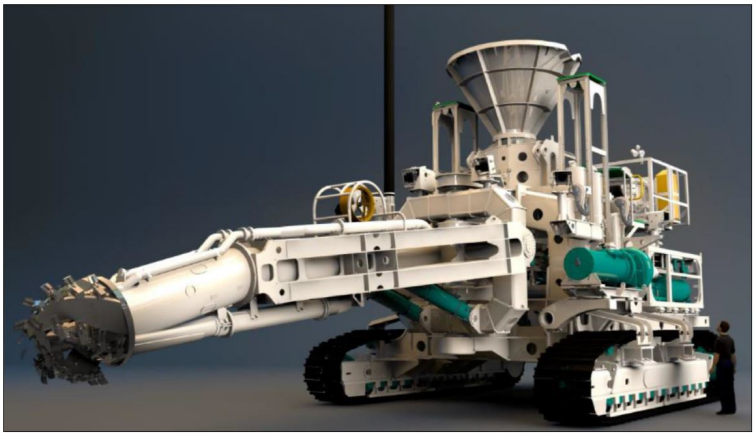

Figure 2.4: Collection Machine designed by the company SMD Ltd[16].

2.5 Riser and Lifting System

The Riser and Lifting System (RALS) is accountable for lifting the mineralized material to the PSV using the vertical riser system and the Subsea Lift Pump (SSLP). The slurry is pumped by a gravity tensioned riser hanged to the PSV from the SSLP situated in the base of the riser. The system demands a large pump installed on the vessel and a rigid riser pipe, hanging from the PSV. The SSLP is a 10-chamber positive displacement pump, where the displacement pump prompts the direct slurry feed from the CM and boosts, via a riser, to the PSV [5]. The Fig. 2.5 illustrates the location of the SSLP and RALS in the production system. The entire SSLP system demands 7.8 MW [11].

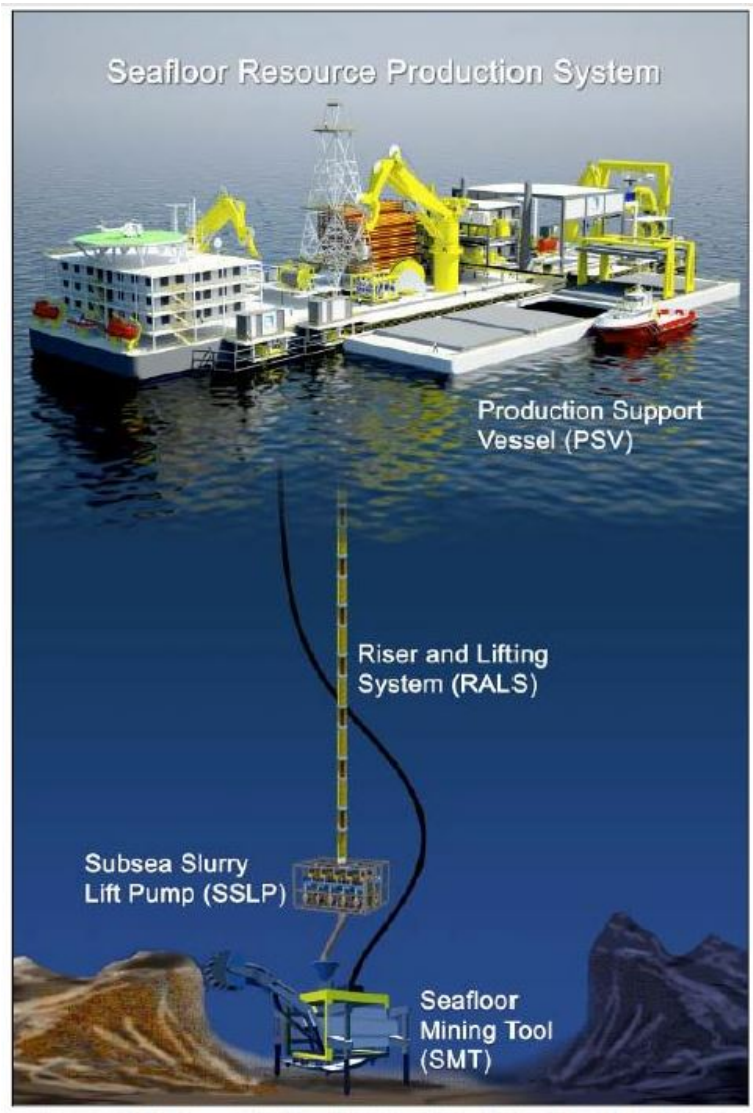

Figure 2.5: DSM Production System [19].

2.6 Production Support Vessel

The Production Support Vessel (PSV) yields a solid base for sea mining operations. It is responsible for deployment of equipment, their operation, storing minerals, and assembling of mining sites. The vessel has dynamic positioning technologies to guarantee that it stays on location against severe natural forces as strong winds and wave conditions. The vessel holds a storage system with a capacity of 45000 t and an ore dewatering plant in the vessel's hull. The PSV will hold the position during the entire mining operation; an extra bulk carrier will transport the ores stored to shore about each 5 to 7 days. The PSV is geared with a moonpool responsible for deploying the riser system and the Subsea Slurry and Lift Pump (SSLP). The maximum ship generation is 31 MW, provided by six diesel-generators with the same capacity, the vessel can accommodate 180 persons and is 227 m in length and 40 m in width [1].

Chapter 3

Power System Description for DSM

This chapter aims to outline the critical aspects and characteristics related to the design and operation of a subsea grid powered from offshore to DSM application. Even though the deep sea mining is in the embryonic stage, the electric grids for this application have similarities with offshore drilling regarding operation environment, power, and energy demands.

Therefore, looking into offshore drilling systems is a good starting point to a deep sea mining electric grid design. Typical offshore drilling platforms are in the range of 5-300 MW [12], in general, supplied by gas turbines or diesel generators [12, 20]. Which is similar to Nautilus pilot project where a vessel with diesel generators with 31 MW capacity will be used [1]. The platform electric power distribution is portrayed as weak electric grid, i.e., it presents power quality issues, for instance, high reactive power demand/low power factor, current and voltage harmonics and voltage notches [23]. Such characteristics eventually increase the losses compromising the operating conditions and reducing lifetime. The author in [22] estimates that the financial loss for incidents originated from poor power quality in the oil & gas sector is about 250,000-750,000 € per day.

Aiming at reducing the losses, a new trend in the oil & gas industry can be observed. The platform operators started to remove as many processing systems and components as possible from the floating production units and to install them on the seafloor. In general, such systems which correspond to gas compression, boosting and water injection and separation have a dedicated umbilical supplying power using medium voltage (normally voltages around 6.6 kV) which is controlled by topside variable speed drives. Indeed, in the first subsea mining project Solwara 1, the conceptual idea is to provide power to the heavy work-class Remotely-Operated Vehicles (ROVs) using the same configuration, i.e. one dedicated umbilical for each load.

When it comes to the operation of mining machines, they must be monitored and controlled continuously from the PSV. The full-control on the cutting process provides the specific quantity of power to the rocks based on their physical properties employing changes to the motor speed

and torque of the cutter heads. Whether not, the stones may turn into fine particles during crushing or they can stay unaffected (no crack appears) [17]. Thereupon, Variable Speed Drivers (VSDs) are required for the head motors in the vehicles responsible for breaking the rocks. Moreover, VSDs should drive all system pumps, avoiding clogging in the slurry transferring tubes and providing a constant flow rate of density varying slurry.

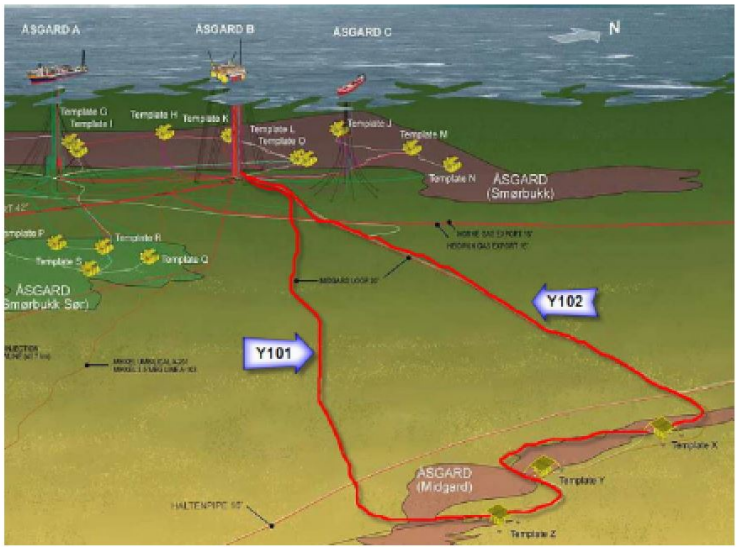

Figure 3.1: Asgard field, typical subsea distribution [32].

3.1 Different power distribution alternatives

There are several possible topologies to supply power to subsea equipment. In this chapter, five alternatives are presented, which are either based on AC or DC distribution systems. Aspects such as power losses, voltage drop, and reactive power generation are considered and compared among the options [9, 11], the subsea volume grade, and efficiency are also taken into account [10]. Finally, the rationales of the distribution topology chosen in this study will be presented and described in details in section 3.2.

3.1.1 AC distribution

The AC distribution is similar to systems used in oil & gas industry. Since the distance between the vessel and the loads are relatively short, less than 5 km; it may be justifiable to install the VSDs on the vessel feeding the subsea loads individually, see Fig. 3.2. Although it is considered a common practice nowadays in the oil & gas industry [15, 18], the solution presents excessive voltage drop in the power umbilicals (12 %) and substantial power losses (10 %) [11]. These values can be reduced by increasing the distribution voltage level over 6 kV. However, the excessive amount of umbilical cables represents a significant drawback due to their weight and cost.

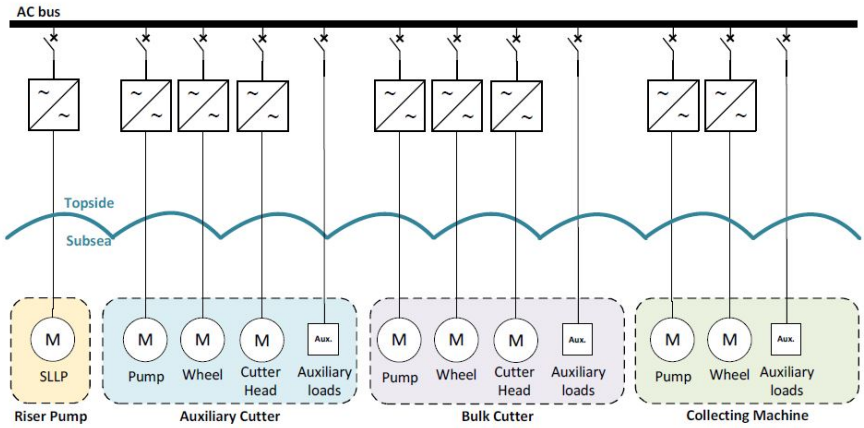

Figure 3.2: First configuration: Individually AC power cable to subsea loads. Mostly of the equipment installed in the vessel.

The second configuration is to use subsea VSDs (installed in pressure compensated environment [47]) on each mining vehicle, Fig. 3.3. The number of power umbilicals will be reduced by 3 or 4, depending on the type of load, which is an advantage compared to configuration 1. There are improvements in power loss and voltage drop. Such a solution has the benefit of facilitating the starting process of the motors, and furthermore moving the converters to seabed will enhance the available space for ore's storage in the vessel.

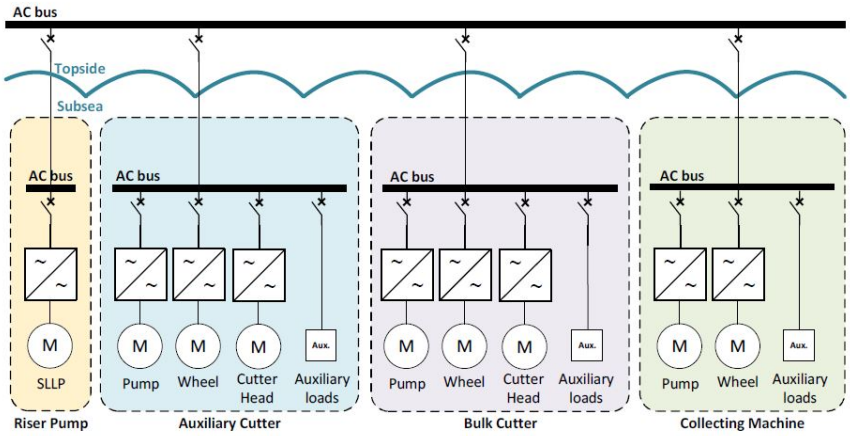

Figure 3.3: Second configuration: Separate AC bus and subsea converters installed on the subsea mining vehicles.

The third configuration uses a subsea AC bus to connect to the subsea loads; the solution requires a subsea transformer and subsea protection to each load individually, see Fig. 3.4. This scheme is more suitable for high power demands. It is stated in [11] that the voltage drop can be less than 2 % and the power loss in the cable less than 1%. However, the reactive power exchange will be considerably high, 1100 kVAr, due to the cables and subsea transformer. The technology

required for this topology started to become achievable. The oil & gas industry started to bring the offshore electric grids one step further. Companies such as Siemens and ABB started the process of installing power-distribution stations on the seabed, allowing more production of wells and higher efficiency [46]. The technology uses VSDs, transformers, and switchgears designed in a pressure compensated environment completely able to operate up to 3000 m water depth, see Fig. 3.5. This technology brings the debate of how much power electronics is possible to implement in such an environment without downturns in the reliability of the equipment.

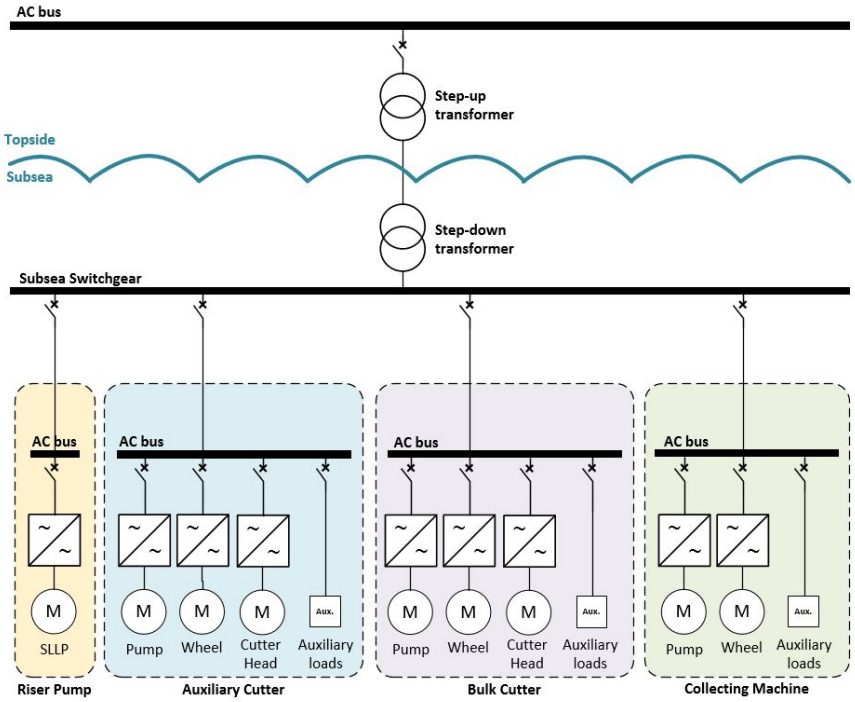

Figure 3.4: Third configuration: One main subsea power hub.

(a) Siemens Subsea Power Grid during the shallow water test. Power generation in the platform and a subsea grid fed by an MVAC umbilical [46].

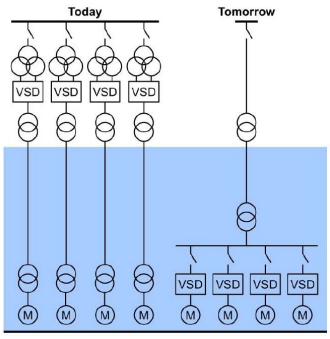

(b) Topology to supply power to subsea loads [47].

Figure 3.5: Subsea distribution with one main subsea power hub.

3.1.2 DC distribution

DC distribution has become attractive in the ship industry [28, 29]. The development in this technology turns it attractive to deep sea mining utilization. The DC cables enable more efficient systems [11], because there is no demand for reactive power generation or consumption. Furthermore, the insulation of DC cables considers the peak value of the applied voltage. Therefore, the size, weight, and cost of the insulation material will be reduced. The DC distribution allows cost and size savings due to less employment of conversion stages since fewer stages of AC-DC conversion are required on each load.

However, DC distribution systems also have drawbacks, such as galvanic insulation and protection against short circuit currents, the solutions for these contraints are still under development [27, 30], and represent a challenge to DC distribution technology.

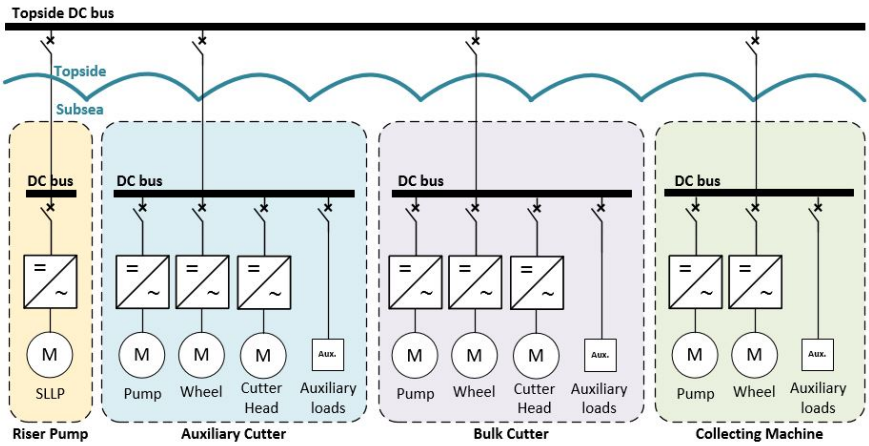

Figure 3.6: Fourth configuration: DC bus on topside and DC-AC converters installed in the mining vehicles.

Another possibility for DC distribution is to supply power to the subsea loads using a centralized DC bus fed from two medium voltage DC cables, see Fig. 3.7. This configuration becomes more attractive when the power demand per load is high, for instance, between 10-20 MVA. Although the voltage drop and power losses in this configuration are similar to the previous configurations [11], the DC bus provides the following advantages:

- Considerable cost reduction on the umbilical power cables, since the connections between subsea equipment are less complex than the structure of the umbilicals; only three subsea jumpers, between the DC bus and subsea loads, are required for power distribution.
- Reduction of cost due to the modularity. The equipment can be deployed one by one and connected posteriorly. In case of failure of one equipment its replacement and intervention schedule will be less complex.

- No need for synchronism. By using DC transmission, the topside and the subsea grids are decoupled regarding the frequency of the grid. Therefore, a failure in one of the motors will not affect the stability of the grid upstream. Besides that, the independence of synchronism allows the subsea loads to receive an additional auxiliary power, for instance, an Uninterrupted Power System (UPS) installed locally. This UPS can be connected in addition to the main power, protecting the emergency systems of the ROVs in case of voltage outage.

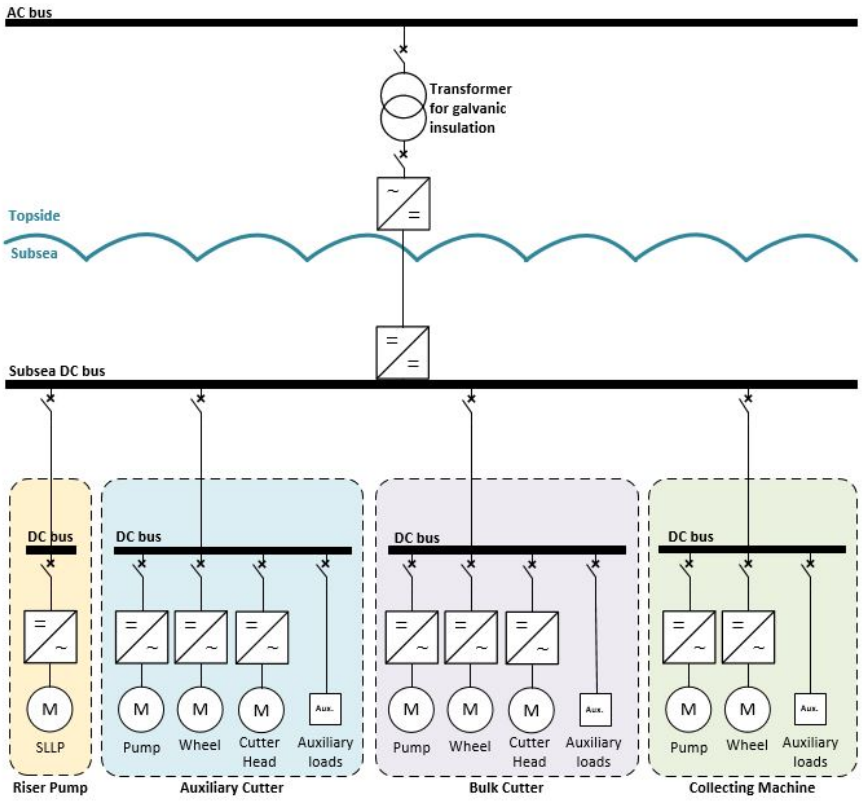

Figure 3.7: Fifth configuration: Common DC bus represented by a DC-DC converter supplying power to DSM equipment.

3.2 Subsea distribution using DC-bus topology

Evaluation of the subsea distribution using DC-bus topology will be the focus of this work. The power quality of the DC-bus is one of the critical requirements for DC distribution design. The voltage must comply with voltage tolerances and acceptable voltage ripple. The standard [14] clearly states "*In a dc distribution system, the fundamental frequency is zero and the concept of harmonic distortion does not apply. Previous definitions of power quality typically involving harmonic distortion limits are not applicable. However, a comparison of average dc current to rms value of current ripple might be of value in setting a power quality standard for dc distribution*

systems."

Fig. 3.8 depicts the configuration studied in this report. It consists of a topside system with a two level voltage source converter, controlling the power delivered to the subsea system, and a subsea DC-DC converter, which provides DC power, the desired voltage level, to the mining vehicles. On the vehicles, a DC-AC takes place, to supply power to the motor-pumps installed in each SPT. For the sake of simplicity, only a single bus representing the system upstream the transformer is showed in the figure.

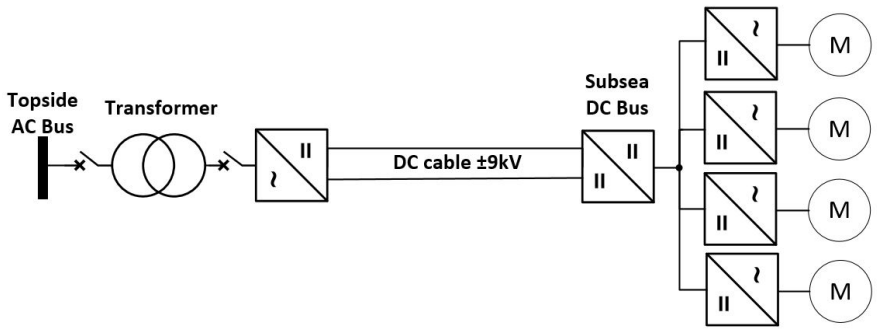

Figure 3.8: Schematic of the topology investigated in this work.

Chapter 4

System Modeling

This chapter focuses on the design of the elements of the power systems proposed. The assumptions for the modeling of each equipment are explained. For the converters mathematical modeling and control loops are designed. The performance for the control can be observed in the appendix D. Fig. 4.1 illustrates the power system modeled and evaluated in this report.

The system consists of the topside system, represented by an AC source; the topside AC-DC converter, which transmits power to subsea by bipole MVDC distribution to a subsea hub. The subsea hub is a DC-DC converter which steps down the voltage to the final subsea loads. The DC-DC converter is responsible for maintaining the DC voltage stable in the subsea environment, at last, the subsea loads, mostly DC-AC inverters, are represented by a single load connected to the DC-link.

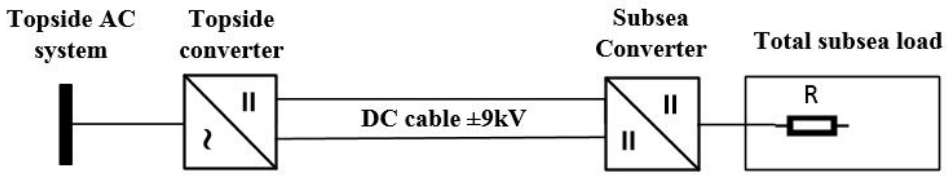

Figure 4.1: Schematic of the model implemented in Matlab/Simulink.

4.1 Loads

The DSM loads consist of low voltage DC auxiliary systems, i.e. by sensors and actuators, and medium voltage induction motors, used for the mining tools. The motors require DC-to-AC inverters to control voltage and frequency, i.e. speed and torque. These inverters must use the

controlled DC-bus voltage to provide sinusoidal voltages to the AC induction motors. In this chapter, when the word inverter is used, it is related to the 2-level Voltage Source Inverters (VSIs), well used in the industry to control motors. It is also considered that the VSIs belong to the PWM category to control both magnitude and frequency of the output voltage.

No further details related to the internal power system of these inverters will be covered in this report, more details regarding the converter can be found in [54] . It is considered that each of these equipment will require a DC voltage with a specific power demand, which is specified in chapter 2 and summarized in table 4.1. It is assumed that the power to the subsea lift pump system (SSLP) will also be provided by the DC-hub, represented by the subsea converter. This equipment corresponds to more than 50 % of the total power consumption of the subsea system. Therefore, it is worth evaluating the efforts of the system to handle different types of load.

Table 4.1: Load list corresponding to the subsea loads [6].

Equipment	**Load**
Auxiliary Cutter (AuxC)	2.0 MW
Bulk Cutter (BC)	2.5 MW
Collection Machine (CM)	1.8 MW
Subsea Lift Pump (SSLP)	7.8 MW
TOTAL	**14.1 MW**

The auxiliary systems are made up of different power supplies stepping down the DC-link voltage to any desired voltage to the auxiliary systems. Differently, the motors require a specific AC voltage to operate. Since no data has been confirmed regarding the voltage level of the motors in DSM applications, a well-known voltage value, employed by offshore drilling industry, is utilized as a reference. The voltage of 6.6 kV is a typical input voltage to the motors used in oil & gas applications [15]. Thus, this value will be also considered for the motors in the DSM vehicles.

Three-phase inverters are regularly used to supply power to the induction motors. By using the pulse width modulation technique (PWM), the inverter can control and shape the voltage magnitude and frequency to the motor from a constant input voltage V_d, which will be supplied from the subsea DC-DC converter hub.

Now, in order to define the output DC voltage required to obtain 6.6 kV in the motor terminals, the amplitude modulation ratio must be defined. The amplitude modulation ratio (m_a) is defined as:

$$m_a = \frac{V_{control}}{V_{tri}} \tag{4.1}$$

Where the control signal $V_{control}$ is applied to modulate the duty cycle ratio and the wanted output frequency (f_{out}) of the inverter output voltage has the wanted fundamental frequency

f_{fund} of the inverter voltage output. Also, V_{tri} is the amplitude of the triangular signal of the PWM, which is usually kept constant. In the linear range, ($m_a \leqslant 1$) the relation between V_d and V_{LL}, which is the AC phase-to-phase voltage, is depicted below:

$$V_{LL} = 0.612 m_a V_d \tag{4.2}$$

The modulation m_a can present values above 1; in this case, the inverter will operate in the overmodulation zone, which motor drives commonly use. The overmodulation generates many more line harmonics in the inverter output voltage. The harmonics appear centered around the harmonic frequencies (m_f) and its multiples. Nevertheless, the dominant harmonics cannot be as high as the amplitudes seen in the linear zone ($m_a \leqslant 1$). Thus, the power loss originating from the harmonic frequencies will be lower [54]. Fig. 4.2 exemplifies the difference between the harmonic spectrum of the linear and overmodulation cases.

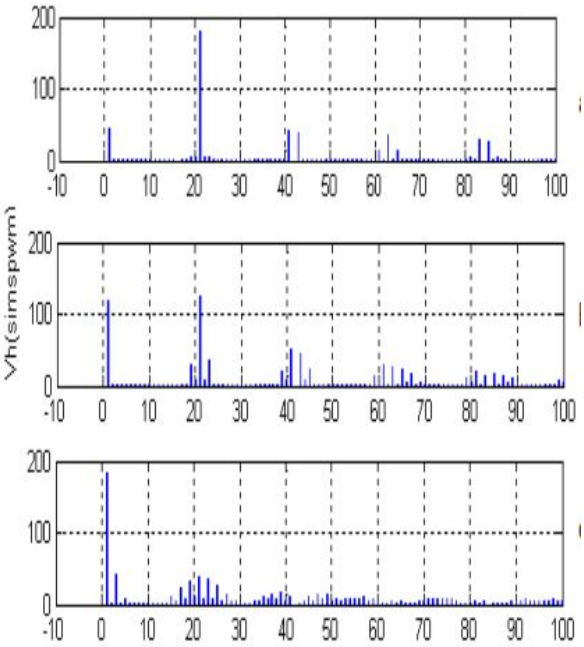

Figure 4.2: Harmonic spectrum for the line voltage of an inverter with a switching frequency of 4.5 kHz and m_a equal to 0.3 (upper graph), 0.8 (middle graph) and 2.0 (lower graph) [55].

Fig. 4.3 depicts the regions of linear modulation, overmodulation, and square-wave for the inverter. The region of overmodulation is not-linear and depends on the value of m_f. Therefore, the linear zone will be used to model the load, since the linear zone does not depend on m_f values.

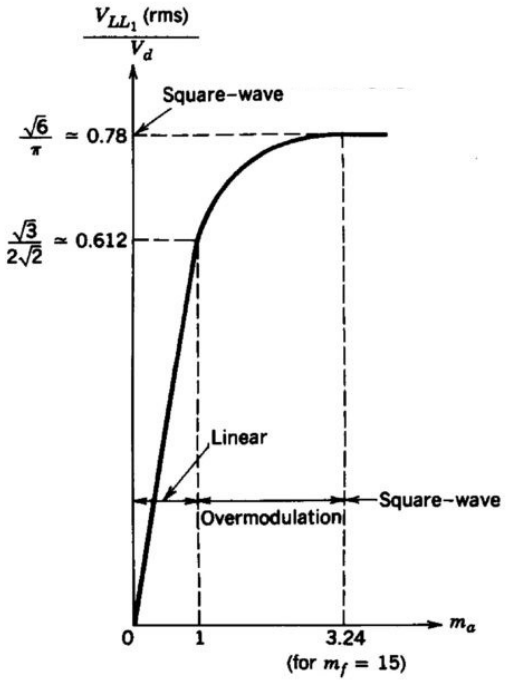

Figure 4.3: Three-phase inverter $V_{LL_{RMS}}/V_d$ as function of m_a [54].

Table 4.2 presents the possible values for the output voltage of the DC-DC converter to be able to deliver 6.6 kV to the subsea motors, based on different m_a values. It is relevant to highlight that the greater the m_a, the higher the harmonic content [54]. So $m_a = 0.8$ will be chosen, since $m_a = 0.6$ will lead to the output distribution voltage of the DC-DC converter holding the same voltage as the desired value for the DC transmission voltage of 18 kV (±9 kV), which will limit the voltage regulation of the device. Consequently, the subsea DC-link will operate at 13 kV (±6.5 kV).

Table 4.2: Possible V_d based on $V_{LL} = 6.6$ kV

$\mathbf{m_a}$	$\mathbf{V_d}$
0.2	54 kV
0.4	27 kV
0.6	18 kV
0.8	**13 kV**
1.0	11 kV

Once established the voltage level and the power demand, the load can be modeled in Simulink now. Simulink is graphical programming environment used for modeling and simulating dynamic systems. In the system studied in this report, the entire subsea load will be represented as an active load connected to the subsea DC-link from the DC-DC converter. Since the system has a DC distribution, the reactive power downstream the subsea inverters are not relevant. Thus, assuming $P_{load,base} = 14$ MW. The resistance at the subsea DC-link will be.

$$R_{load} = \frac{V_{DC-bus}^2}{P_{load}} = \frac{(13\text{k})^2}{14\text{M}} = 12.07\Omega \tag{4.3}$$

4.2 Subsea DC-DC converter

The subsea distribution requires a DC-hub in order to provide the proper DC voltage to the DSM equipment. Supplying DC power directly from the DC umbilical to each equipment may lead to poor quality voltage, due to extensive voltage and current ripples in the 5 km power cable. Despite a target distance of 5 km is considerable to be short for power transmission from topside to subsea, a DC-hub will allow to DSM design projects utilize distances further than 5 km.

The DC-hub must eliminate any disturbances in the input transmission voltage, providing a stable distribution voltage to the subsea consumers. Aspects as short-circuit protection and wet-mate disconnection of loads are wanted features of this equipment, with regard to DC power quality issues. However, they will not be covered in this report.

The DC-DC converter must step-down the transmission voltage to the distribution voltage level of 13 kV (±6 kV). The technology enabling a high power MV DC-DC converter is still not available in the market; however, with the constant development of DC-grids, such converters will become a reality in the near future. Power electronics prototypes using components with silicon carbide (SiC) in the range of 2 kV-35 kV have been under development in the past 20 years by accredited research institutions [56]. They are called Solid-State Transformers (SST) and are presented in a variety of topologies in order to reduce switching losses or footprint or even increase the power capability substantially. The non-isolated DC-DC converters topologies do not present a transformer in the circuit, consequently, they reduce demerits like high costs, excessive power loss, bulkiness and core saturation, aspects imposed by the isolated DC-DC converters.

Regarding the topology, the non-isolated DC-DC converters present five classic types:

- Step-down (buck) converter
- Step-up (boost) converter
- Buck-boost converter
- Cúk converter
- Full-bridge converter

In DSM applications, the energy needs only to be transferred in one direction, from the topside vessel to the subsea loads. Therefore, a full-bridge topology, which enables transferring power

in both directions is not deemed necessary. Among the remaining four topologies, the buck and boost converter are the options with the best switch utilization factor (P_o/P_i) [54], and, since the topology studied in this essay needs to reduce the voltage level to connect the subsea loads, the step-down topology will be implemented.

Fig. 4.4 presents the buck circuit diagram with its control method. In DC-DC converters, the average output voltage shall be controlled to stay constantly at the wanted voltage level, although the input voltage and the output current can fluctuate. The desired output voltage is obtained by controlling the switch on and off duration (t_{on} and t_{off}). It is worth mentioning that, despite the Fig. 4.4 only shows one switch; it may have several switches in parallel, enabling higher currents through the converter.

The method for controlling the output voltage applies to switch at a constant frequency, and fine-tune the duration of the switch to control the average output voltage. Such method is called Pulse-Width Modulation (PWM) switching, and the switch duty ratio *(D)* varies during operation. The deviation signal between the measured voltage and the reference voltage goes through a PI controller, and the amplified error is compared with a sawtooth voltage, see Fig. 4.5.

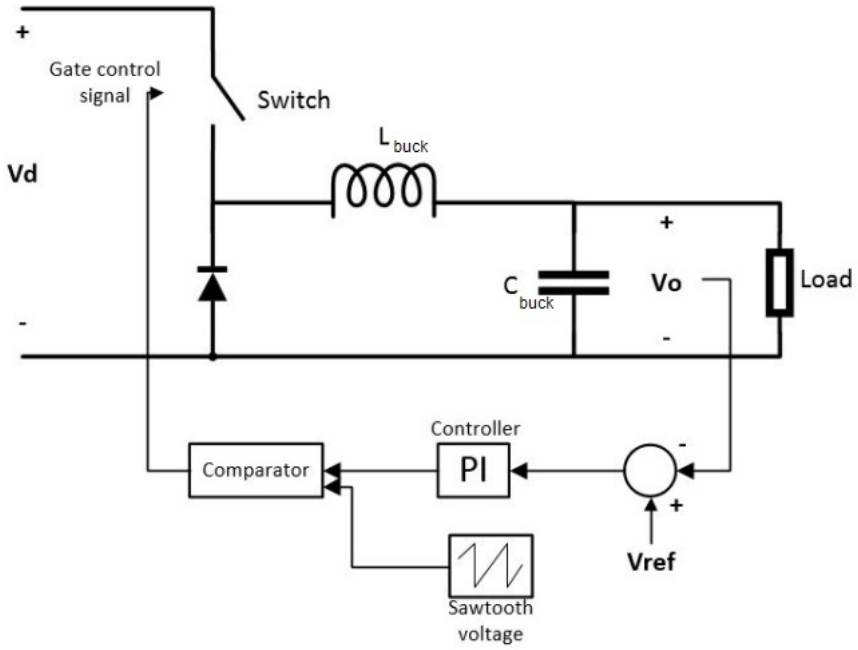

Figure 4.4: DC-DC buck converter diagram with its control loop.

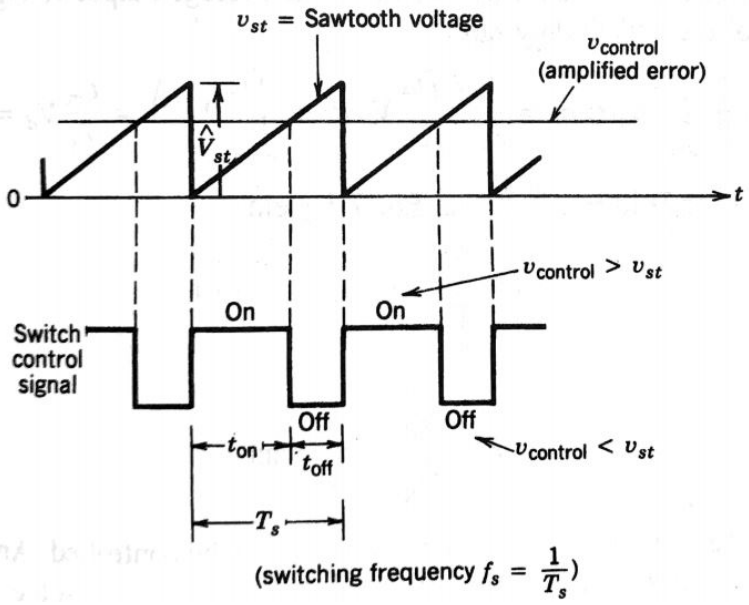

Figure 4.5: Comparator signals for the DC-DC buck converter [54].

Since the output filter capacitor is at zero voltage during the initial phase, two phenomena arise during startup. First, the control loop system will compel the duty cycle to the maximum to push maximum current to build up the output voltage as fast as possible. Second, during on-time, the driving voltage for the inductor current will initially be the total input voltage, which is larger than the steady-state value of the input voltage minus the output voltage. Hence, the inductor current becomes large during the start-up phase. Therefore, the use of a soft-start control circuit allows the duty cycle to build up gradually (while the capacitor charges), minimizing the inrush current until the output voltage is close to the wanted value.

4.2.1 DC-DC Converter parameters

The buck switching frequency f_{buck} is 20 kHz. The higher the switching frequency the faster the response time of the converter. Furthermore a higher switching frequency leads to significantly reduced storage elements in converters, such as inductors and capacitors [69]. Besides that, the considerably hard turn-on losses in the output capacitance limit the switching frequency to go higher [56].

The inductor in the buck converter is designed by the equation:

$$L_{buck} = \frac{(V_{in} - V_{out}) \cdot V_{out}}{V_{in} \cdot f_{buck} \cdot r \cdot I_{out}} \mu\text{H} \tag{4.4}$$

Where:

- L_{buck} is the buck converter inductor
- V_{in} is the input voltage from the power umbilical
- V_{out} is the output voltage of the subsea DC-link
- f_{buck} is the switching frequency of the buck converter
- I_{out} the total output load current
- r is desired ripple, which is 0.2 (20%) for this application [67]

Using the equation 4.4 with a load current of 260 A (aiming to have a maximum ripple of 20 % during operations with a light load, i.e. 25 % of the total load) the initial value of the inductor is depicted below. Based on the result the inductance value L = 3.5 µH is chosen.

$$L_{buck} = \frac{(18k - 13k) \cdot 13k}{18k \cdot 20 \cdot 0.2 \cdot 260}\mu H = 3.47\mu\text{H} \tag{4.5}$$

And, the capacitor can be calculated as follows:

$$C_{buck} = \frac{I_{out}(1 - D) \cdot 1000}{f_{buck}.V_{ripple}}\mu\text{F} \tag{4.6}$$

where

$$D = \frac{V_{out}}{V_{in} \cdot 90\%} \tag{4.7}$$

While assuming a converter efficiency of 90 %.

Using the parameters presented previously, and targeting to a ripple of 1 % (130 V) the value of the DC-link capacitance will be:

$$C_{buck} = \frac{260 \cdot 0.8 \cdot 0.2 \cdot 1000}{20 \cdot 130}\mu\text{F} = 16\mu\text{F} \tag{4.8}$$

Once the L and C parameters are obtained a final check must be done. The corner frequency (f_c) of the low-pass filter of the DC-DC converter must be considerably smaller than the switching frequency, otherwise it will affect the voltage ripple [54] in the DC-link.

$$f_c = \frac{1}{2\pi\sqrt{LC}} = 2.12\text{kHz} \tag{4.9}$$

Thus, the condition is verified $f_c \ll f_{buck}$.

Control loop design

The PI controller design is based on former experiences of the author and it was designed based on the system response during Matlab simulations.

The PI values are: $K_{P,buck} = 60$ and $K_{I,buck} = 160$.

Fig. 4.6 shows the converter performance when connected to an ideal 18 kV DC source. Two disturbances are added to the system, a load increase at t=0.4 second (increase of 220 %) and a load decrease at t=1 second (decrease of 45 %). The converter takes approximately 100 ms to reestablish the nominal voltage in the DC-link. The voltage ripple is approximately 160 V (1.2 %) while the current ripple is 20 A (1.5 %), both less than the target of 20 %.

Fig. 4.4 shows the control loop model for the DC-DC converter, however additional blocks are required for the system to run stable and time efficient in Simulink. Fig B.1, in Appendix B, shows how the control system is implemented in Simulink. The sawtooth signal must be stepped from (-1<signal<1) to (0<signal<1). After stepped the signal the block output signal is reaching the maximum level of 0.98, instead of the desired unity. So the signal also needs to be divided by 0.98 in order to cover the range from 0 to 1. This needed correction has been observed in Simulink R2019a version, and it may not be an issue in other versions.

Regarding the error signal before sending it to the comparator, it is necessary to assure that the error is in the range of the sawtooth signal. Otherwise the comparator will not work and, consequently, the IGBT will not switch. A saturation and a gain block are used to achieve this.

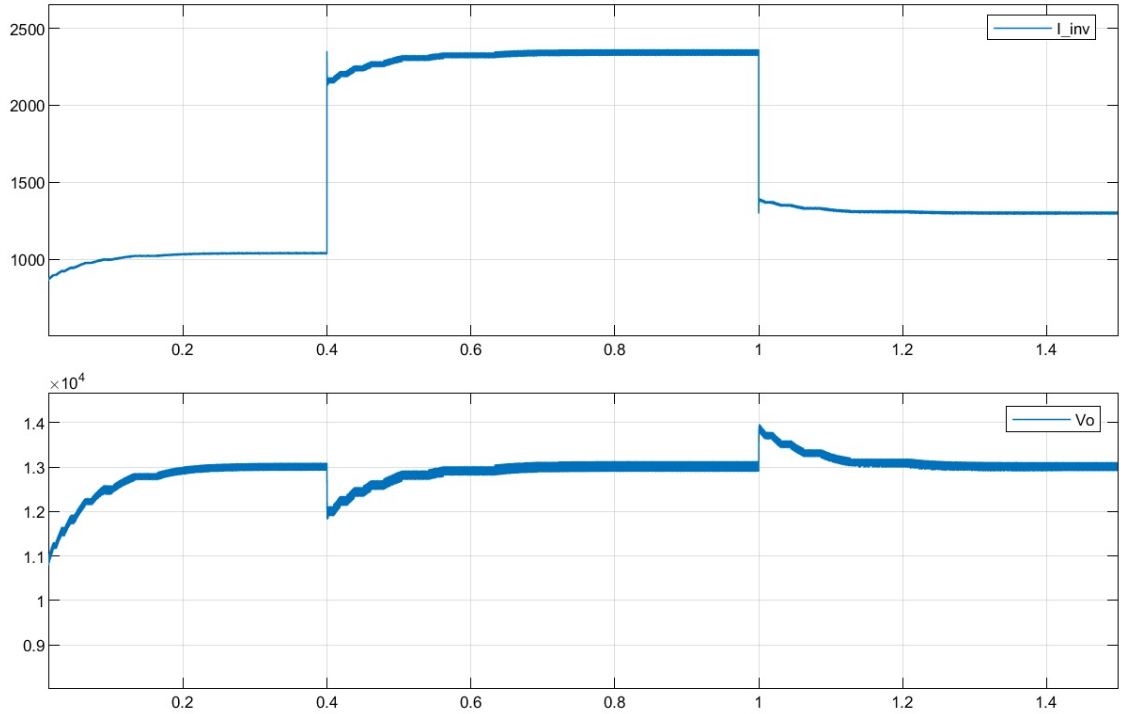

Figure 4.6: DC-DC converter response evaluation. The upper graph shows the converter current while the lower graph shows the converter output voltage.

Table 4.3: Buck converter parameters.

Parameter	**Symbol**	**Value**
Input voltage	V_i	13-18 kV
Output voltage	V_o	13 kV
Switching frequency	f_{buck}	20 kHz
Line Inductor	L_{buck}	3.5 µH
Output Capacitor	C_{buck}	16 µC
Proportional gain	$K_{p,buck}$	60
Integral gain	$K_{i,buck}$	160

4.3 Umbilical cable

The modeling of the subsea cable has a relevant role in the simulation. The chosen model can affect significantly both the simulation speed and the accuracy of the results.

4.3.1 Cable structure

The subsea cables have a considerably complex structure, for VSC-HVDC applications cables with XLPE (cross-linked polyethylene) insulation became popular due to its low cost compared to other materials. Furthermore, they show better robustness when compared to mass-impregnated cables [39].

Cables for VSC-HVDC seem suitable for a DC-grid for DSM application since both systems are subsea the cables will be submitted to the same environment stress. Among the differences between the applications it is worth highlighting the two most relevant to the cable structure:

- the voltage level - the DC-grid suggested intending to use only 18 kV in the power umbilical; consequently, the capacitance between the conductor and the insulation screen in a cable for DSM application will be higher than cables for HV applications, see appendix E.
- the cable termination - HVDC applications have both ends of the cable terminating above sea level, while in a DSM application one end will be terminated underwater.

Fig. 4.7 illustrates the general construction of the cable. The power transfer conductor is made by copper or aluminum. The XLPE insulation surrounding the conductor builds a barrier between the conductor and layers with ground potential preventing arc. The cable construction requires insulation screen and conductor screen, to protect the insulation from grooves/ridges. Such grooves/ridges are a result of extruding the insulation directly into the conductor [40]. The lead alloy sheath is made of a semiconducting material which is grounded and maintain the electric field in the cable homogeneous and with a radial pattern to prevent insulation breakdown and reduces leakage currents.

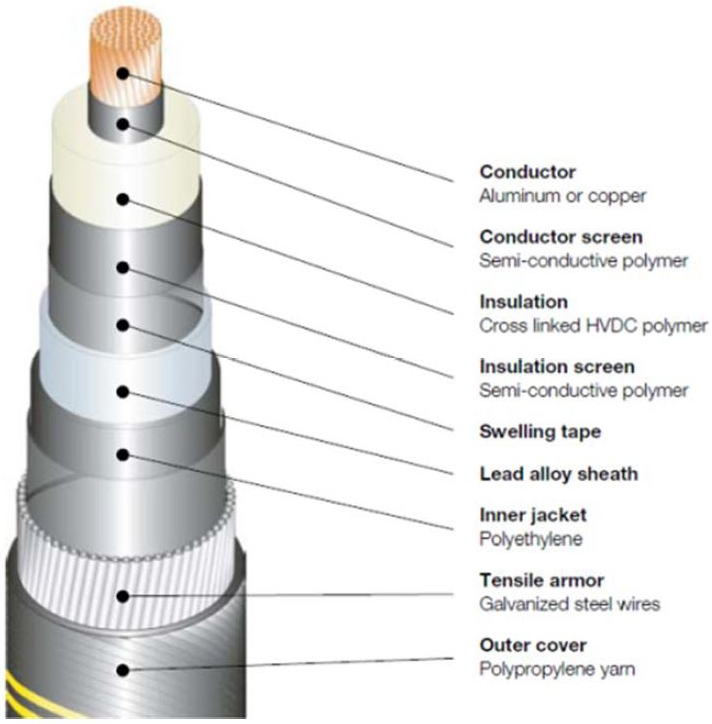

Figure 4.7: Subsea XLPE HVDC cable from ABB [38].

In the presence of any ridge/groove in the insulation may result in an enhancement of the electric field stress, which could lead to the reduction of the electric field strength of the insulation.

A swelling tape provides water sealing in the longitudinal direction; the tape absorbs humidity as well [40]. The inner jacket is responsible for corrosion prevention, and mechanical protection, and the tensile armor gives protection against possible abrasions and impacts. And, the outer layer prevents scratches in the zinc coating, present in the armor, avoiding damage in the anti-corrosion protection.

4.3.2 Cable modelling types

There are four main types of cable models used in literature:

1. **PI Model -** The concept is implemented in the lumped system. The model lumps the cable's parameters resistance, inductance and capacitance together forming N PI sections where $N \geqslant 1$. This model is appropriated to cases when the travel time of the wave propagation is smaller than the time step of the simulation. The author in [38] states that considering a time-step of 50 μs and the maximum speed of propagation in an ordinary an XLPE cable, the travel time will only be less than the time-step if the cable has a length shorter than 50 km. In this report, the maximum length is 5 km; therefore, the PI model

utilization is relevant.

2. **Bergeron Model -** is more sophisticated than the PI model by representing L and C accurately, however with a lumped R to calculate the cable losses. The reference [41] highlights that the model is accurate at a specific frequency and is more suitable when such specific frequency is crucial, as in relay studies, for instance. However, for harmonics and electromagnetic compatibility studies, the model will miss some frequency response information.

3. **Travelling Wave model 1, frequency dependent in Mode** - This model is obtained by a constant transformation matrix [42]. It represents the frequency dependence of all parameters of the cable. The model is based on modal techniques to resolve cable constants assuming a constant transformation [41].

4. **Travelling Wave model 2, frequency dependent in phase** - This model is similar to the one previously explained. However, it overcomes the problem of using a constant transformation matrix by implementing a formulation directly in the phase domain. It is worth mentioning that the frequency dependent models are not available in the Simulink version utilized for analysis by the author of this report.

Based on these four models authors have evaluated the impact of each model in simulations of VSC-HVDC applications. The author on [38] shows no significant changes in the response of the four models related to power consumption changing in a back-to-back grid using VSC. However, a change could be seen in the results for faults occurring in the DC side of the system. The model type 1 (PI mode) shows no propagation delay while the type 2 (Bergeron) shows approximately two times delay when compared to frequency dependent models (3, 4). For faults at AC side the PI-model and frequency dependent models showed similar results whilst the Bergeron showed a different trasient behavior.

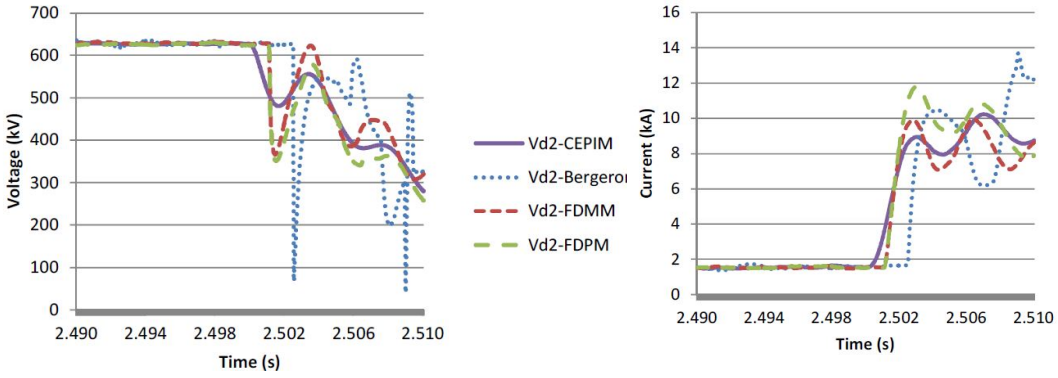

(a) Voltage response.

(b) Current response.

Figure 4.8: Response to a DC fault for the different models: PI model (CEPIM), Bergeron, frequency domain mode dependent (FDMM) and phase dependent (FDPM) [38].

The frequency dependent models suggest the best performance regarding studies involving

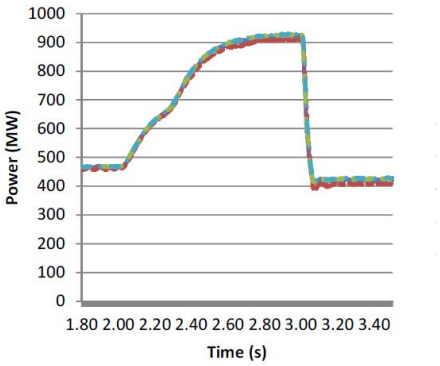

(a) Response to a power consumption increase.

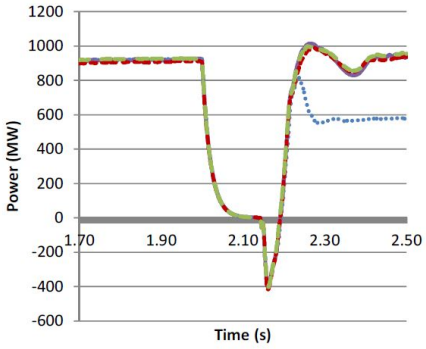

(b) Response to AC fault at the Point of Common Coupling (PCC).

Figure 4.9: Response to a AC fault for the different models: PI model (CEPIM), Bergeron, Frequency domain mode dependent (FDMM) and phase dependent (FDPM) [38].

HVDC applications and long lines. However a deep knowledge regarding the cable construction, and about the environment when it is installed is deemed necessary.

The power system proposed in this thesis has umbilical power cables much shorter than the ones employed in HVDC applications. The location of the application is not defined either. As well as the type of insulation that will be used in the cable. In addition, evaluating the results of the systems in [38] and [41], travelling wave mode will not add considerable further extra information to the system modelled in this thesis. Thus, the travelling wave models will not be employed in this study.

In most of the cases, lumped parameter models as the PI-sections are considered appropriate when the simulation time-step is smaller than the wave propagation travel time. By using a time step of 50 µs and the maximum propagation speed in a typical XLPE cable, the travel time can only be less than the simulation time-step for cables shorter than 10 km [38].

So, the lumped parameter model is suitable for this application. The proper number of Π sections will depend on the frequency range to be represented. Considering the switching frequency of the topside converter which is 10 kHz and the total cable length of 5km. The number of Π section is calculated as follows:

$$N = \frac{8 \cdot l_{cable} \cdot f_{sw}}{\sqrt{L_{cable} \cdot C_{cable}}} = 7 \tag{4.10}$$

Where f_{sw} is the switching frequency of the topside converter.

The frequency parameter in Simulink Π section line block is set to 5 Hz, as recommended in DC studies [38].

4.3.3 Cable parameters

The power umbilical cable must handle a maximum current of 777 A, based on a maximum load of 14 MW, related to the maximum power consumption of the subsea loads. The Fig. 4.10 depicts the current rating for single-core medium voltage submarine cables in dependence of the cable cross-section for AC applications.

The design of the cable must have some margin, avoiding overheating and increasing its lifetime. For the system designed in this report the 1000 mm^2 cross-section is chosen, assuming wide spacing installation the cable will have a maximum loading coefficient of 61%, if the ampacity of an AC application is considered. However, when operating in DC, the cable will have some extra allowance presenting even lower loading coefficient.

Cross section Cu conductor	Rated voltage 10 - 90 kV	
	Wide spacing	Close spacing
mm^2	A	A
95	410	315
120	465	355
150	520	395
185	585	435
240	670	495
300	750	545
400	840	610
500	940	670
630	1050	740
800	1160	805
1000	1265	870

Figure 4.10: Current rating for single-core submarine cables - Table 35 [36], attached to appendix E.

There are not many references for submarine cables conducting high currents at medium voltage, especially in a single cable configuration. The reference [36] presents electrical characteristics for MV submarine cables; however, only in a three-core configuration. The reference also depicts values for single core cables, but with an initial voltage level of 220 kV. The values for a single-core cable with 1000 mm^2 are shown below, the rated voltage level of the cable is far beyond the needed for the application in this report, however the conductor and cable configurations fit the needs for the system design.

Table 4.4: Cable data [36].

Parameter	Symbol	Values
Cross section		1000 mm^2
Capacitance	C_{cable}	0.19 μF/km
Inductance	L_{cable}	1.35 mH/km
Resistance*	R_{cable}	0.10 Ω/km
Cable length	$d_{\text{len\_cable}}$	5 km
No. of Π sections	N	7
Design frequency	f_{cable}	5 Hz

*Maximum resistance at 20 °C

4.4 Topside converter

The topology used for the topside AC-DC converter is the two-level voltage source converter (2L-VSC); this topology has been employed widely in HVDC systems. This type of converter operates at high frequency employing Pulse-Width Modulation (PWM) technique, by switching IGBTs. The VSC has benefits when compared to the classic thyristor-based converter, such as:

1. Faster dynamic response leading to filter size reduction and/or elimination [48].
2. Reduced footprint when compared to thyristor based [48].
3. Allows the control of the reactive power independently.
4. Considerably lower short circuit level [50].

Fig. 4.11 shows the circuit diagram of the VSC converter. The indices *abc* will be replaced by 123 during the analysis of the differential equations of the circuit in section 4.4.1.

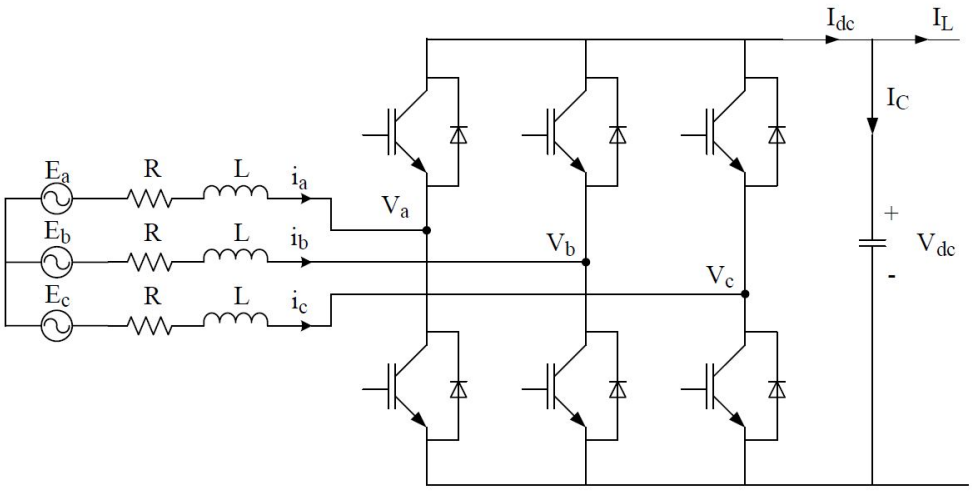

Figure 4.11: VSC electric diagram representation [48].

4.4.1 Converter Mathematical Model

There are different methods to control the VSCs, and a vast number of articles can be found in literature regarding such methods. The method implemented in this report is the vector control method.

The method consists of control independently the active and reactive power, using PI controllers with *dq* signals in the synchronous reference frame, obtained from the *abc* stationary coordinate of current and voltage from the input side of the VSC.

The method to obtain the needed equations is described in [70]. Assuming a balanced three-phase system with no connection to the neutral point and disregarding the resistance in the power switches, the converter can be modeled as follows:

$$C\frac{du_{dc}}{dt} = \sum_{k=1}^{3} i_k d_k - i_{dc} \tag{4.11}$$

$$L\frac{di_k}{dt} + Ri_k = e_k - u_{dc}\Big(d_k - \frac{1}{3}\sum_{k=1}^{3} d_n\Big) \tag{4.12}$$

$$\sum_{k=1}^{3} e_k = \sum_{k=1}^{3} i_k = 0 \tag{4.13}$$

where:

- k index for the phases
- i_k line currents
- d_k switching functions {0,1}
- e_k phase–to-neutral voltages
- u_{dc} DC voltage
- i_{dc} DC current
- R resistance of the converter reactor
- L inductance of the converter reactor

To transfer the quantities from phases 1,2,3 to *dq* coordinates the following relations are used:

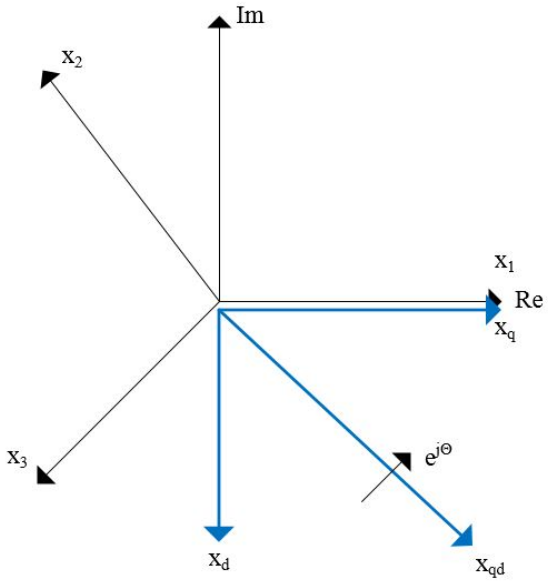

Figure 4.12: Three-phase and dq rotation frame superimposed.

$$x_q = \frac{1}{3}(2x_1 - x_2 - x_3) \tag{4.14}$$

$$x_d = \frac{1}{\sqrt{3}}(x_3 - x_2) \tag{4.15}$$

$$\bar{x}_{qd} = x_q - jx_d \tag{4.16}$$

Where $\bar{x}_{\mathrm{qd}}$ is a counterclockwise rotating complex vector.

Now, the equations representing the VSC converter can be written in the dq frame as:

$$C\frac{du_{dc}}{dt} = \frac{3}{2}(i_q d_q + i_d d_d) - i_{dc} \tag{4.17}$$

$$L\frac{di_q}{dt} + Ri_q = e_q - u_{dc}d_q \tag{4.18}$$

$$L\frac{di_d}{dt} + Ri_d = e_q - u_{dc}d_d \tag{4.19}$$

And, the equations can be rewritten using the complex notation

$$C\frac{du_{dc}}{dt} = \frac{3}{2}Re\left\{\bar{i}_{qd}\bar{d}^*{}_{qd}\right\} - i_{dc} \tag{4.20}$$

$$L\frac{d\bar{i}_{qd}}{dt} + R\bar{i}_{qd} = \bar{e}_{qd} - u_{dc}\bar{d}_{qd} \tag{4.21}$$

where * means the complex conjugate.

The eq (4.20) and (4.21) can be written using the two-phase synchronous reference frame:

$$\bar{x}^e_{qd} = \bar{x}_{qd}e^{-j\theta} \quad \theta = \int \omega dt \quad \omega = 2\pi f \tag{4.22}$$

Now it is possible to establish the equations (4.20) and (4.21) using (4.22), which is the dq synchronous reference frame notation.

$$C\frac{du_{dc}}{dt} = \frac{3}{2}Re\left\{\bar{i}^e_{qd}\bar{d}^{e*}_{qd}\right\} - i_{dc} \tag{4.23}$$

and

$$L\frac{d\bar{i}^e_{qd}}{dt} + R\bar{i}^e_{qd} + j\omega L\bar{i}^e_{qd} = \bar{e}^e_{qd} - u_{dc}\bar{d}^e_{qd} \tag{4.24}$$

Eq. (4.23) and (4.23) can be written in coordinates dq separately, then:

$$C\frac{du_{dc}}{dt} = \frac{3}{2}(i^e_q i^e_q + i^e_d i^e_d) \tag{4.25}$$

$$e^e_d - u_{dc}d^e_d = L\frac{di^e_d}{dt} - \omega L i^e_q + Ri^e_d \tag{4.26}$$

$$e^e_q - u_{dc}d^e_q = L\frac{di^e_q}{dt} + \omega L i^e_d + Ri^e_q \tag{4.27}$$

4.4.2 Converter Control System

Fig. 4.13 shows the control diagram of the VSC, the function of each block is described in detail later in this section.

PLL measurement

The block PLL corresponds to the Phase-locked loop; it is an essential feature of the converter control. The feature detects the phase angle of the grid voltage to synchronize the delivered power. In order to have a unity power factor, the algorithm synchronizes the output current of the inverter with the grid voltage [48].

The control block inputs are the three AC voltages measured upstream the converter and the output is the tracked phase angle θ, where θ=$\tan^{-1}(-v_d/v_q)$. The PLL transfers the abc coordinates

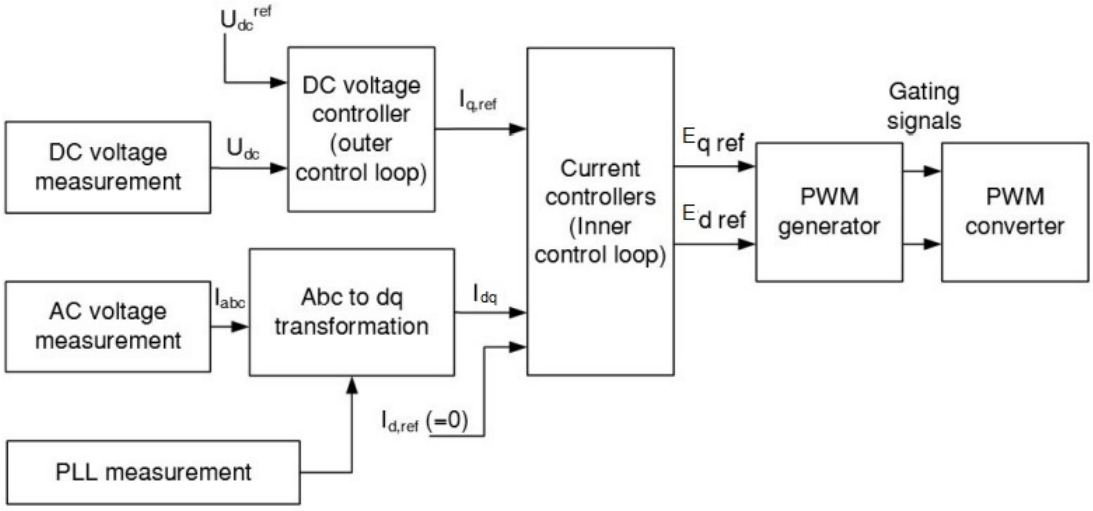

Figure 4.13: Functional control diagram of the VSC using *dq* rotating frame.

to the fixed *dq* reference frame using *abc* to *dq* transformation and, posteriorly phase-locking the system adjusting the q-axis voltage to zero. Thenceforth the *dq* reference frame changes from fixed to the synchronous reference frame.

PWM generator

In an analog PWM modulator, when there is a change in the modulating signal the duty cycle (output) reacts to the variation, therefore the reaction to the input variation happens in the same switching period. However, in digital modulation it will not occurs. There is a delay preventing that the variation in the duty cycle occur at the same period as the variation in the input signal. Thus, with digital PWM modulator there is a delay from 0 to T_{sw} in the response of the generator, which can be assumed as $T_{sw}/2$, where T_{sw} is the inverse of the converter switching frequency ($T_{sw} = 1/f_{sw}$).

Hence, transfer function representing the PWM has the expression:

$$Y(s) = \frac{V(s)}{V'(s)} = \frac{1}{1 + sT_a} \quad \text{where} \quad T_a = \frac{T_{sw}}{2} \tag{4.28}$$

4.4.3 Current control loop

The current control loop, also called the inner controller, handles the error between the measured current and the reference current. Once the currents are transformed to the synchronous reference frame, they turn to DC signals beneath balanced sinusoidal conditions and perfect synchronization [49]. The control system demands a decoupling in the control of i_d and i_q.

However, analysing the equations 4.26 and 4.27 it can be seen that the axis are coupled by the cross terms ωLi_d and ωLi_q. Therefore the feed-forward compensation is required to control the current components i_d and i_q independently, resulting in two decoupled systems having the same structure, which is depicted in Fig. 4.14.

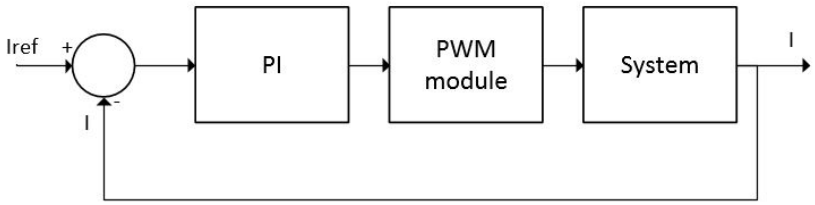

Figure 4.14: Block diagram of PI current control loop (in per unit), analogous for I_d and I_q.

The first block is related to the PI regulator, its representation in the Laplace domain is shown in the first fraction of equation 4.29.

The PWM modulation is taking into account as a simple delay represented by a 1^{st} order transfer function, see equation 4.29 where $T_a = T_{sw}/2$, when T_{sw} is $1/f_{sw}$, as mentioned previously.

And, the system transfer function is represented by the last part of the open loop transfer function 4.29, where pu stands for per unit valus.

$$G_{i,OL}(s) = \left(\frac{K_i + K_p s}{s}\right) . \left(\frac{1}{1 + s\tau_a}\right) . \left(\frac{1}{R_{pu} + sL_{pu}}\right) \tag{4.29}$$

Modulus Optimum

The modulus optimum is often used in the conventional controller tuning for low order controlled systems without time delay. When these plants have two time constants, one dominant and another minor time constant, the standard control function is achieved by the cancellation of the biggest time constant [48]. The goal of this method is to achieve a transfer function of the closed loop that is constant at 1 between the frequency zero and a frequency highest possible [53]. The requirements for this method are that one pole must be dominant and no poles can be in the origin. So, based on this method the further equations can be used for tuning the controller:

$$k_{ppu} = \frac{1}{2} . \frac{L_{pu}}{\omega_b \tau_a} \qquad k_{ipu} = \frac{k_{ppu}}{\tau_{ipu}} \tag{4.30}$$

where

$$\tau_{ipu} = \frac{L_{pu}}{\omega_b R_{pu}} \tag{4.31}$$

Assuming:

- ω_b is the base angular frequency
- R_{pu} converter line resistance in per unit
- L_{pu} converter line inductance in per unit

4.4.4 Voltage control loop

The voltage control loop, or outer control loop, is used to regulate the voltage in the converter DC-bus. It is determined using the transfer function between the current reference value and DC-link voltage of the converter using values in pu, see Fig. 4.15. The objective of the PI regulator is to keep the DC voltage $v_{DC_{ref}}$ following its reference $v_{DC_{ref}}$.

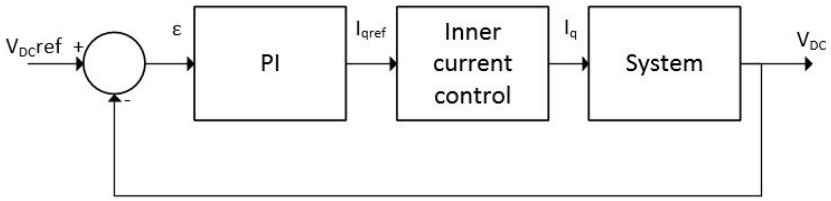

Figure 4.15: Block diagram of the voltage control loop (in per unit).

The PI controller structure is similar as the PI used in the current control loop, and the equation is depicted below.

$$\frac{I_{qref}(s)}{E(s)} = \frac{K_{P_{DC}} s + K_{I_{DC}}}{s} \tag{4.32}$$

Symmetrical Optimum

The method modulus optimum is genuinely efficient when the controlled system has one dominant time constant and other minor time constants, as seen in the current control loop system. However, when one of the poles is near the origin or in origin, the pole shift does not change the system condition reasonably [48]. Also, the open loop transfer function of the outer loop has already two poles in origin, consequently making the system unstable.

Furthermore, whilst the inner control loop regulated by modulus optimum pinpoints at a fast

response, the utilization of symmetrical optimum in the DC voltage loop is applied to improve disturbance rejection.

This method enables having the cross-over frequency where the phase margin is maximum, allowing the system to oppose to considerable delays without stability loss, that is very worthwhile for systems that can be subject to delays [53].

From the block diagram in Fig. 4.15, neglecting the feed-forward and disturbance input, the open loop transfer is considered as:

$$G_{v,OL}(s) = K_{pv.pu}.\left(\frac{1+sT_{iv}}{sT_{iv}}\right).\frac{1}{1+sT_{eq}}.\left(\frac{V_{dpu}}{V_{dcpu}}.\frac{\omega_b C_{pu}}{s}\right) \tag{4.33}$$

Introducing $K_{pv.pu} = V_{dpu}/V_{dcpu}$ and $T_c = 1/\omega_b.C_{pu}$, the transfer function becomes,

$$G_{v,OL}(s) = K_{pv.pu}.\left(\frac{1+sT_{iv}}{sT_{iv}}\right).\frac{1}{1+sT_{eq}}.\left(\frac{V_{dpu}}{V_{dcpu}}.\frac{1}{sT_c}\right) \tag{4.34}$$

For this method the tuning criteria is obtained by using Nyquist criteria of stability.

$|\mathrm{G_{V,OL}(j\omega)}| = 1$ and $\angle \mathrm{G_{V,OL}(j\omega)}$ = -180°+ $\phi^{\circ}_{\mathrm{M}}$ when ϕ_{M} is the phase margin.

The condition for maximum value of phase margin is obtained differentiating the angle criteria, which leads to:

$$\omega_d = \left(\frac{1}{\sqrt{T_{iv}T_{eq}}}\right) \tag{4.35}$$

which gives the tuning criteria for the time constant, as follows:

$$T_{iv} = T_{eq}.\frac{1+sin\phi_{\ M}}{1-sin\phi_{\ M}} \tag{4.36}$$

So, from the equation above it can be observed that ω_{b} satisfies to the geometrical average between $1/\mathrm{T_i}$ and $1/\mathrm{T_{eq}}$. Therefore, calling a the symmetrical distance between $1/\mathrm{T_{eq}}$ to ω_{b}, and $1/\mathrm{T_{iv}}$ to ω_{b}, by symmetry this equation can be written

$$T_{iv} = a^2.T_{eq} \tag{4.37}$$

So, now the gain of the controller can be found:

$$K_{pv,pu} = \frac{T_c}{K.\sqrt{T_{iv}T_{eq}}} = \frac{T_c}{a.K.T_{eq}} \tag{4.38}$$

Replacing T_{iv} and $K_{pv,pu}$ the transfer function for open and close loop become:

$$G_{v,OL}(s) = \frac{1 + sa^2T_{eq}}{s^2a^3T_{eq}^2(1 + sT_{eq})} \tag{4.39}$$

$$G_{v,CL}(s) = \frac{1 + sa^2T_{eq}}{1 + sT_{eq}a^2 + s^2a^3T_{eq}^2 + s^3a^3T_{eq}^3} \tag{4.40}$$

It can be demonstrated that s=-1/aT_{eq} is a solution for the equation, hence the denominator can be rewrite, as:

$$G_{v,CL}(s) = \frac{1 + sa^2T_{eq}}{(s + \frac{1}{aT_{eq}})(aT_{eq} + sa^2(a-1)T_{eq}^2 + s^2a^3T_{eq}^3)} \tag{4.41}$$

4.4.5 DC-link capacitor

The design of the capacitor of the DC-link is an crucial part of the system design. Due to the PWM switching, DC-harmonics will flow in the DC-side of the system, generating a voltage ripple. The magnitude of the ripple depends on the switching frequency and the DC-link capacitance. The capacitor time contant τ is usually utilized as a measure of the capacitor energy. The constant τ is defined as:

$$\tau = \frac{C_{DC}V_{DC}^2}{2S_{AC}} \tag{4.42}$$

Where:
C_{DC} is the capacitance
V_{DC} is the rated DC voltage
S_{AC} is the power supplied to the converter

So, considering τ being equal to 5 ms, the capacitance will be:

$$C = \frac{2 \cdot 14 \cdot 10^6 \cdot 0.02}{(18 \cdot 10^3)^2}\mu\text{F} = 432.1\mu\text{F} \tag{4.43}$$

Thus, C = 500 μF will be chosen for better performance.

Now, all converter parameters can be summarized. Table 4.5 depicts the parameters for the control loops, based on the method previously explained, and also the other parameters of the converter.

Table 4.5: VSC parameters.

Parameter	Symbol	Value
Switching frequency	f_{sw}	10 kHz
Line Inductor	L_{vsc}	4.1 mH
Output Capacitor	C_{vsc}	500 µC
Current Proportional gain	K_{p_vsc}	1.5915
Current Integral gain	K_{i_vsc}	33.33
Voltage Proportional gain	K_{pv_pu}	2.335
Voltage Integral gain	K_{iv_pu}	467

4.5 Topside system

Fig. 4.16 depicts a potential configuration for the topside grid upstream the PCC. As stated in chapter 2, the total generation in the first DSM application will be 31 MW. However no information related to the source impedance is disclosed.

For the matter of power quality analysis, the topside system designed in this thesis considers only the Thevenin's equivalent for the system located upstream the PCC. Initially, the AC source will be considered ideal, focusing the study in the design of the DC-grid. Posteriorly, the Thevenin impedance will be added considering the maximum short circuit level of the system and its X/R ratio.

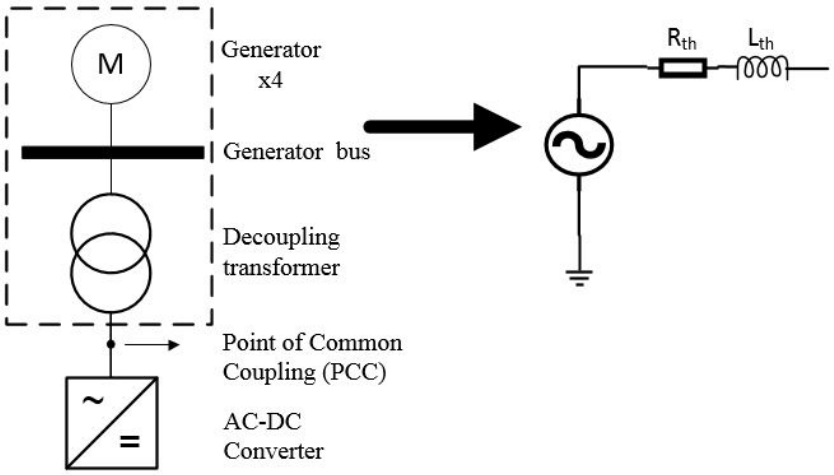

Figure 4.16: Topside system seen by the topside converter.

4.5.1 Influence of source impedance on harmonics

The power sources are usually categorized as "stiff" or "soft" related to harmonics [34], and both categories have relevant effects on the voltage and currents distortions.

The "stiff sources" are commonly associated with power transformers, the source impedance is in the range of 5 % - 6 %. Differently, the generators are often called "soft sources" whose the subtransient reactance, customarily used as source impedance, is in the range of 10 % - 18 % [34].

Stiff sources present high levels of short circuit capability, allowing the non-linear loads to draw substantial levels of harmonic currents for a given kW quantity of non-linear load, since the leakage reactance of the source does not restrict it. As a consequence, high current harmonic content will not distort the grid voltage. On the other the hand, soft sources likely have restricted short circuit capability, limiting the level of current harmonics drawn by nonlinear loads. However, this reduced level of harmonic current will generate substantial levels of voltage distortion.

Chapter 5

Power Quality Assessment

Power electronic devices as variable-frequency drives and AC-DC converters, despite of benefits to better control loads, introduce a reasonable amount of harmonics into the vessel's power network, which may lead to potential risks, if not controlled and predicted.

This chapter presents the power quality aspects that must be evaluated in the AC and DC-side of the converter, connected to the PCC in the DSM support vessel, in order to prevent potential failures.

As explained in section 4.5.1, the generators in marine vessels are quite susceptible to harmonics, due to their limited short circuit capability. This phenomenon is even more severe in diesel generators, leading to high levels of voltage harmonic distortion [35].

The power quality problem has become a relevant issue, leading to the creation of standards instructing the users to maintain the harmonic content of the grid below the recommended limits. The IEC 6100-2-4 states that the THD_v shall not exceed 8 %, while the individual harmonic order must be below 5 %. The American Bureau of Shipping (ABS) is even more severe, they state that the THD_v shall not go over 5 % while individual harmonic order must not exceed 3 % [34]. To fulfill such strict requirements some techniques can be applied.

5.1 AC harmonic mitigation

The voltage harmonic distortions occur when a distorted current from the supply is drawn by a non-linear load, going across all impedances between the power source and load. In a typical converter there are three locations where these harmonics can be mitigated.

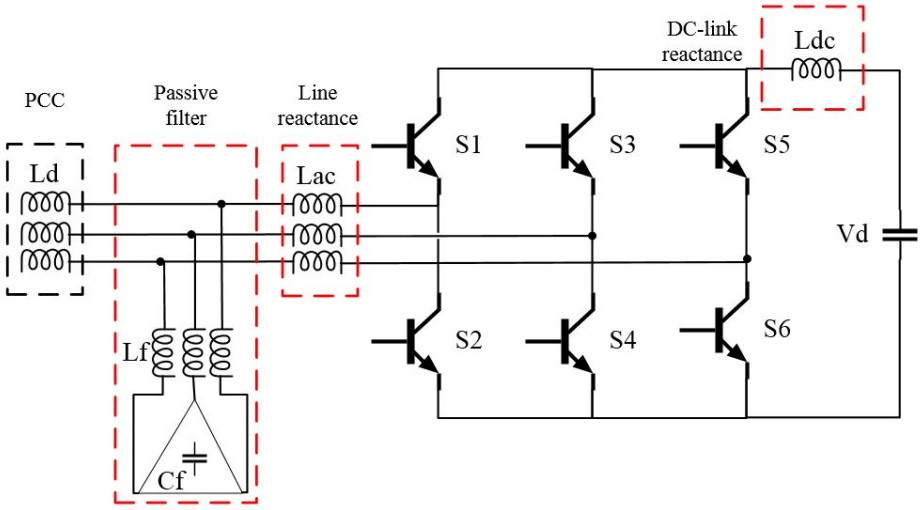

Figure 5.1: Typical Converter topology with three options for harmonic mitigation.

5.1.1 Option 1 - Line Reactance

The line reactors are used to reduce the rising rate of the currents ($\mathrm{d}i/\mathrm{d}t$), by inhibiting the rate of voltage rise, creating a voltage step change due to the voltage drop across the terminals. The inductance is calculated as follows:

$$L[\mathrm{H}] = \frac{\Delta_{\mathrm{V_{drop\%}}} \cdot \left(\frac{\mathrm{V_{LL}}}{\sqrt{3}}\right)}{\omega . \mathrm{I_L}} \tag{5.1}$$

It is worth mentioning that 5 % is commonly used as maximum design value avoiding unwanted high voltage drops across the reactance [35].

5.1.2 Option 2 - DC Reactance (choke)

DC reactances may be installed in the DC-link to avoid voltage drops associated with the line reactors. The choke value is calculated using the voltage drop desired from (5.1).

$$L_{DC}[\mathrm{H}] = \frac{\Delta_{\mathrm{Vdrop\%}} . \mathrm{V_{DC}}}{\omega . \mathrm{I_{DCavg}}} \quad \text{where} \quad \mathrm{I_{DCavg}} = \frac{\mathrm{P_M}}{\mathrm{V_{DCavg}} \cdot \eta_{\mathrm{M}} \cdot \eta_{\mathrm{inv}}} \quad \text{and} \quad \mathrm{V_{DC_{avg}}} = 1.35\mathrm{V_{LL}} \tag{5.2}$$

Where:
η_M is the efficiency of the motor in the inverter side
P_M is the motor power
η_M is the efficiency of the inverter

5.1.3 Option 3 - Passive filter

The use of passive filters in the AC-side is a common and efficient practice of the industry. The idea consists of connecting the LC filter in parallel with the non-linear load and tune the circuit to have minimum impedance at a desired resonant frequency. The formula to calculate the resonant frequency is depicted below:

$$f_{res} = \frac{1}{2\pi\sqrt{(L_f + L_d)C_f}} \tag{5.3}$$

Where:
L_f is the filter inductance
C_f is the capacitor inductance
L_d is the source inductance seen from the PCC

It may happen that while tuning the series resonance the filter may create a parallel resonance increasing the circuit impedance at low frequencies, which is an important drawback of this solution. However, it can be mitigated by adding more passive filters for other possible resonance frequencies.

It is relevant to highlight the existence of dynamic compensation, even though their price and footprint might be deterrent for a power system for DSM application. These filters employ another converter, based on PWM inverters with high-speed response to eliminate the harmonics.

5.2 DC Harmonics

It is common stated that DC systems do not experience voltage and current harmonics, since, by definition the fundamental frequency of the DC system is 0 Hz. However, practically speaking the oscillations of voltages and currents on a DC system make the discussion of DC harmonics relevant.

The so-called DC harmonics are related to the high frequency harmonics created by the switching frequency of the IGBTs in several converters connected to the DC grid. Such harmonics can reduce the lifetime of the DC-capacitors and over-stress the umbilical cables deteriorating their insulation due to the overlap of AC plus DC harmonics [72, 78], generating high partial discharge overtime and compromising the water-barrier characteristic of the cable. Such effects can grow considerably with the increasing of the switching frequency [79].

These harmonics can also generate resonances, that may affect both AC and DC side of the converters, but with different characteristics. The high and low frequencies are present in both AC and DC sides, and, can be reasonably filtered. On the other hand, the low frequencies generated by the interaction between the DC and AC grids may lead to issues in the rotating equipment, such as in propulsion systems [73] or the motors used in the DSM vehicles. Consequently this phenomenon must be evaluated.

There are several references in literature describing how to analytically calculate the current harmonic spectra by Double Fourier Analysis, relevant examples can be found here [74, 75]. However, to implement such method a sort of assumptions regarding the AC load is required, such as, the inverter modulation (M), the phase shift between the voltage and currents in the load side (ϕ), and the pulse ratio (p), which is the ratio between the load fundamental frequency and the carrier frequency.

Thus, the computational implementation of this complex method will require considerable effort and may not give valuable results, since it considers only one converter, in most of the analysis. And, there is no data available for the possible subsea inverters of the DSM vehicles. The Fast Fourier Transform analysis (FFT) and resonance tools will be used instead. They can give relevant information at system level, when varying the system parameters, which is the proposal of this report.

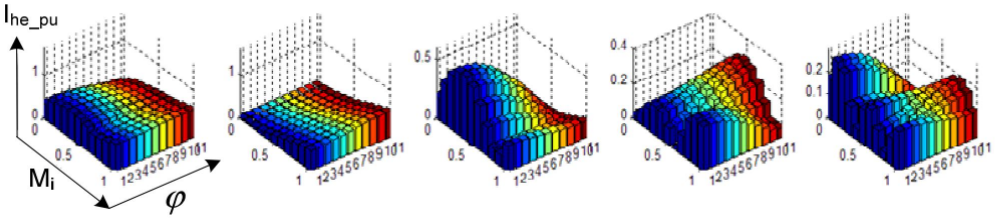

Figure 5.2: Double Fourier Transformation plot for normalized currents using sine PWM with different values of m and ϕ [76].

Chapter 6

Simulation Results

This chapter contains the results of the performance of the power system proposed in this thesis. Fig. 4.1 presented the main four blocks of the system which are:

1. The AC source representing the topside system until the PCC
2. The topside VSC converter, responsible to convert the energy from AC to DC to the DSM subsea grid
3. The power umbilical cable, responsible for the MVDC transmission to the subsea hub
4. The subsea buck converter responsible to distribute the power to four main DSM loads.

The further sub-chapters bring the results of the system evaluation regarding the cable resonance, the system response when load variations occur, the performance for different load levels, the benefits of a precharge system, and the power quality evaluation for four different topside systems scenarios.

The eight cases are summarized below:

- Section 6.1 - System resonance analysis
- Section 6.2 - Response to Disturbance
- Section 6.3 - Load Step Response
- Section 6.4 - Precharge Implementation
- Section 6.5 - Ideal Source with Lvsc = 1.05 mH
- Section 6.6 - Ideal Source with Lvsc = 4.1 mH
- Section 6.7 - Non-ideal Source
- Section 6.8 - Non-ideal Source with Passive Filter

6.1 System Resonance Analysis

The resonance analysis must be performed in order to identify any potential resonances in the system. This is done by analysing the impedances of the system components for a broad frequent range.

Fig. 6.1 depicts the umbilical cable impedance from 0 to 100 kHz, it can be observed that there is no high frequency resonances, however to use this cable for a AC 50 Hz application might be an issue, since there is a series resonance near the 50 Hz, precisely at 56 Hz.

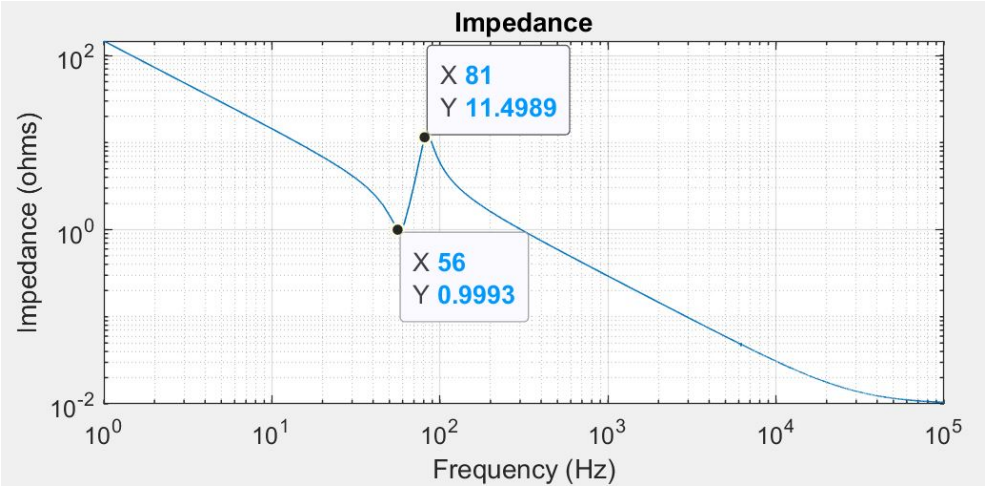

Figure 6.1: Bode plot of the cable impedance.

Fig. 6.2 shows the bode plot of the LC filter in the subsea converter. The plot shows that switching frequencies in the frequency band around 2 kHz should be avoided.

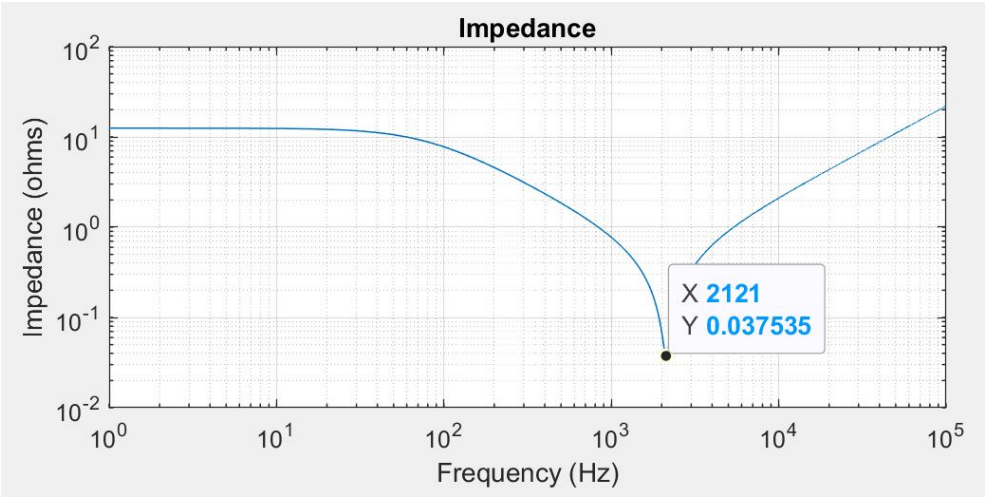

Figure 6.2: Bode plot of the LC circuit of the DC-DC converter.

6.2 System response to disturbances

This section describes the response of the system while disturbances such as abrupt overload and not planned load shedding occur. Two disturbances have been evaluated, a 25 % power increasing, happening at t=1 s, and a 25 % power reduction, which is simulated at t=1.5 s. The total load in the system during simulation is 50 % (7 MW).

The subsea DC-link, which provides the reference voltage to the subsea consumers, remains constant at 13 kV, while the transmission voltage presents an oscillation of 1800 V (10 %) during overload, and 1000 V (5 %) during load reduction, fig. 6.3.

The currents in the system behave as expected. During the overload the current in the power umbilical increases from 200 A to 580 A, and, after the 25 % load reduction the current drops from 580 A to 400 A. The variation of the output current of the subsea converter is an increase from 260 A to 780 A for the first event, and a decrease from 780 A to 520 A to the second event. It is worth mentioning that these results are applicable to the system with a stiff grid topside, and the variations (Δ) are related to the steady-state condition of the system loaded 50 % of S_{base} (7 MW).

Table 6.1: Voltage variation in the power umbilical.

Disturbance	$\mathbf{\lvert\Delta V\rvert}$	**Variation**
25 % Overload	1800 V	(17.8 - 16) kV
25 % Load Reduction	1000 V	(17.5 - 18.5) kV

Table 6.2: Current variation in due to disturbances.

Disturbance	$\mathbf{\lvert\Delta\rvert I_{umb}}$	**Variation**	$\mathbf{\lvert\Delta\rvert I_{sub}}$	**Variation**
25 % Overload	380 A	(200 - 580) A	520 A	(260 - 780) A
25 % Load Reduction	180 A	(580 - 400) A	260 A	(780 - 520) A

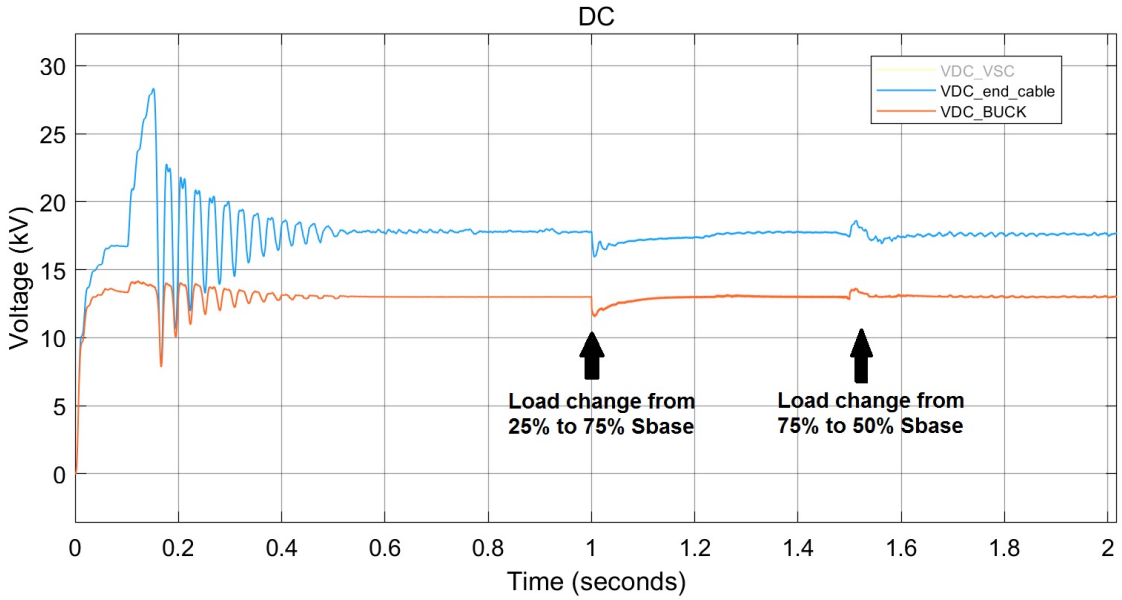

Figure 6.3: Voltages during disturbances in the system.
Signals: V_{DC} in the end of the umbilical (blue) and $V_{DC\text{-}link\ subsea}$(red).

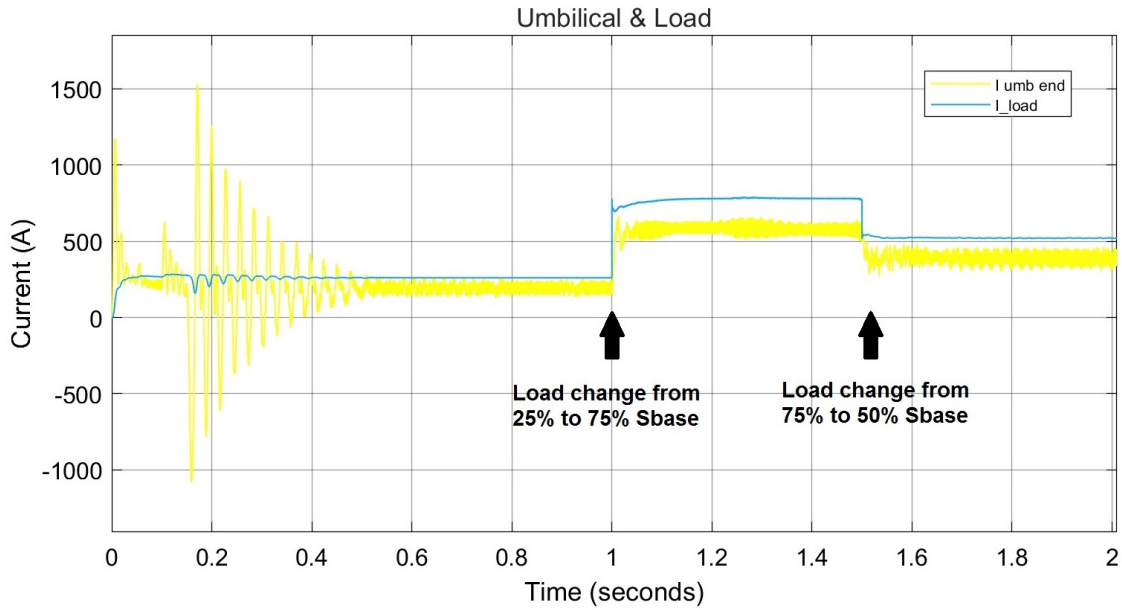

Figure 6.4: Currents during disturbances in the system.
Signals: $I_{umbilical}$(yellow) and I_{load}(blue).

6.3 System evaluation for different load demands

This section evaluates the system when the power demand increases. For this event a reduction of the THD_i is expected while the power increases. A total of 4 different scenarios are chosen for the evaluation, table 6.4 shows the response of the topside AC-side of the system based on the load increase, and, the table 6.5 lists the response in the subsea umbilical and the total current flowing from the DC-bus to the loads. The different power levels are changed based on the maximum R_{load} corresponding to the P_{base} of 14 MW, the impedance is changed in the simulation by changing the load factor *d*.

Table 6.3: Power consumption at the subsea DC-link.

Load factor	**R**	$\mathbf{P_{load}}$
25%	50 Ω	3.4 MW
50%	25 Ω	6.8 MW
75%	16.67 Ω	10.1 MW
100%	12.5 Ω	13.5 MW

The table 6.4 shows the general RMS current reduction with increasing load and increasing of the fundamental current, which benefits the reduction of losses in the circuit branch going to the subsea converters and load.

The table 6.5 shows that the subsea converter succeed in keep the quality of the voltage in the subsea DC-link. Despite of the variations occurring from the topside converter through the umbilical, the subsea converter manages to always deliver 13 kV to the loads.

Table 6.4: Topside system response to different load levels

Load factor	**Aparent Power**	$\mathbf{I_{AC}}$	$\mathbf{I_{fund}}$	$\mathbf{V_{AC}}$
25 %	18.8 MVA	1708 A	1259 A	6.36 kV
50 %	18.0 MVA	1633 A	1299 A	6.36 kV
75 %	17.1 MVA	1548 A	1358 A	6.36 kV
100 %	16.8 MVA	1521 A	1426 A	6.36 kV

Table 6.5: Subsea system response to different load levels

Load factor	**Load**	$\mathbf{I_{dc\ umbilical}}$	$\mathbf{V_{end\ umbilical}}$	$\mathbf{I_{dc\ link\ subsea}}$	$\mathbf{V_{dc\ link\ subsea}}$
25 %	3.38 MW	191 A	17.8 kV	260 A	13 kV
50 %	6.77 MW	390 A	17.6 kV	521 A	13 kV
75 %	14.14 MW	589 A	17.5 kV	780 A	13 kV
100 %	13.50 MW	795 A	17.1 kV	1035 A	13 kV

6.4 Precharge Evaluation

Similar to HVDC applications the MVDC grid studied in this report presents a high inrush current during the turn on of the converters, due to their high capacitive loads. After a DC voltage step response the capacitor in the DC-link starts to charge which results in a high transient current directly proportional to its capacitance. Such currents can damage the components and reduce its life span, and trip the system unintentionally if exceeding the protection setting limits.

Precharge circuits are applied to suppress these high current transients. The precharge current circuit aims to create a soft-start process of the system enabling a gradual charging process of the DC-link. A simple precharge circuit based on changing the impedance seen by the converter through the time is implemented in this report.

The precharge circuit consists of three resistances, and their respective switches, connected in parallel before the DC-link for the VSC. The buck converter only requires two resistors and switches. The system starts with the current passing only through R_1, after some milliseconds the R_2 switch is closed, reducing the resistance in the circuit by connecting R_1 and R_2 in parallel. The same happens to R_3 switch and, in the last stage, the upper switch is closed removing the precharge circuit from the original system. The resistance values are obtained based on the initial response of the converters without a precharge circuit. The detailed Simulink model is presented in Fig. 6.5. Table 6.6 shows the resistors and switching times used on the precharge circuits.

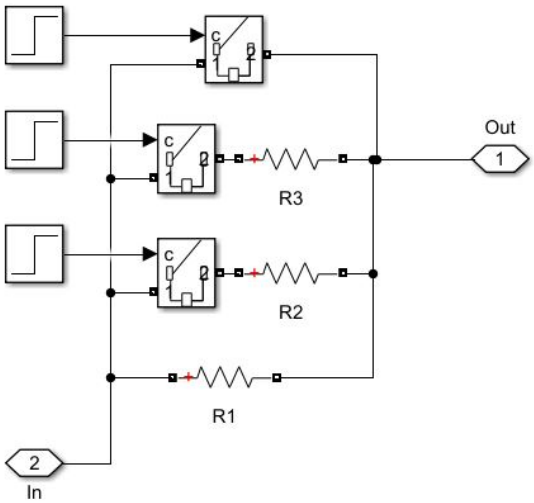

Figure 6.5: Simulink diagram of the precharge circuit of the VSC.

Table 6.6: Precharge circuit parameters.

Converter	Resistor	Value	Switch closing time
VSC	R_1	10 Ω	50 ms
VSC	R_2	7 Ω	100 ms
VSC	R_3	5 Ω	150 ms
Buck	R_1	10 Ω	250 ms
Buck	R_2	2 Ω	300 ms

Four cases of soft-start have been evaluated:

- case 1 - Topside and subsea converters starting at t=0 s without precharge.
- case 2 - Topside and subsea converters starting at t=0 s with precharge enabled in the topside converter.
- case 3 - Topside converter starting with precharge enabled at t=0 s and subsea converter starts at t=200 ms without precharge.
- case 4 - Topside converter starting with precharge enabled at t=0 s and subsea converter starts at t=200 ms with precharge enabled.

6.4.1 Case 1

Figs. 6.6a and 6.6b show the entire system turn-on at the instant t=0 s. Currents of 3400 A will flow in the umbilical power cable, which may lead to an undesired trip. Fig. 6.6a shows the current flowing in the power umbilical and the current from the subsea load. Fig. 6.6b shows the DC voltage in the VSC DC-link, the voltage in the end of the power umbilical and the voltage at the subsea DC-link. The plots for the other cases have the same structure.

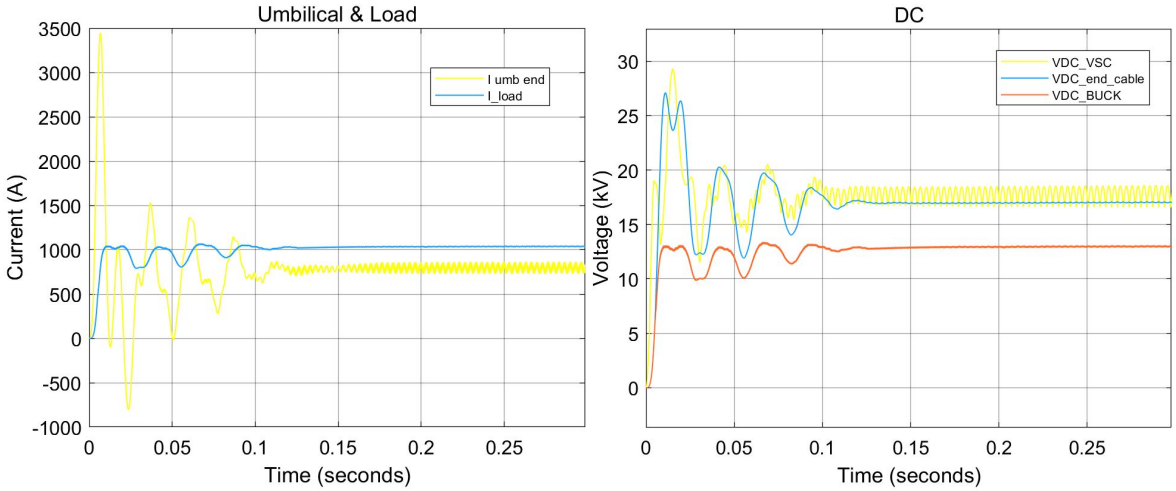

(a) $I_{umbilical}$(yellow), and I_{load}(blue).

(b) $V_{DC,VSC}$(yellow), $V_{end,cable}$(blue) and $V_{DClink,buck}$(red).

Figure 6.6: Currents and voltages for case 1.

6.4.2 Case 2

Figs. 6.7a and 6.7b show the system response for case 2. Both converters start conducting at t=0 s, with the precharge circuit implemented in the topside converter. The soft-start eliminates the inrush current in the topside converter, however start the topside converter, energize the power cable, and start the subsea system at the same instant is not realistic. It is reasonable to assume that the subsea loads will be only powered on after the control system receives feedback confirming that the total start-up process is safe to proceed.

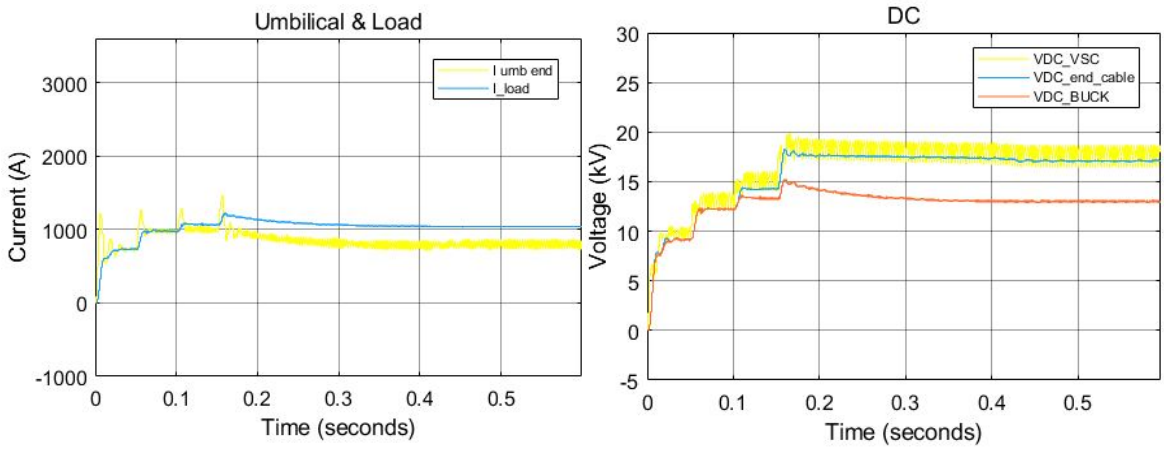

(a) $I_{umbilical}$(yellow), and I_{load}(blue).

(b) $V_{DC,VSC}$(yellow), $V_{end,cable}$(blue) and $V_{DClink,buck}$(red).

Figure 6.7: Currents and voltages for case 2.

6.4.3 Case 3

Results for case 3 are depicted in Figs. 6.8a and 6.8b. Based on what is stated in case 2 the subsea converter must start-up after the topside converter. The simulations of case 3 show that the subsea converter has a similar issue regarding the inrush current due to the DC-link capacitor in the load side of the buck converter. Thus, another precharge circuit in the buck converter is relevant.

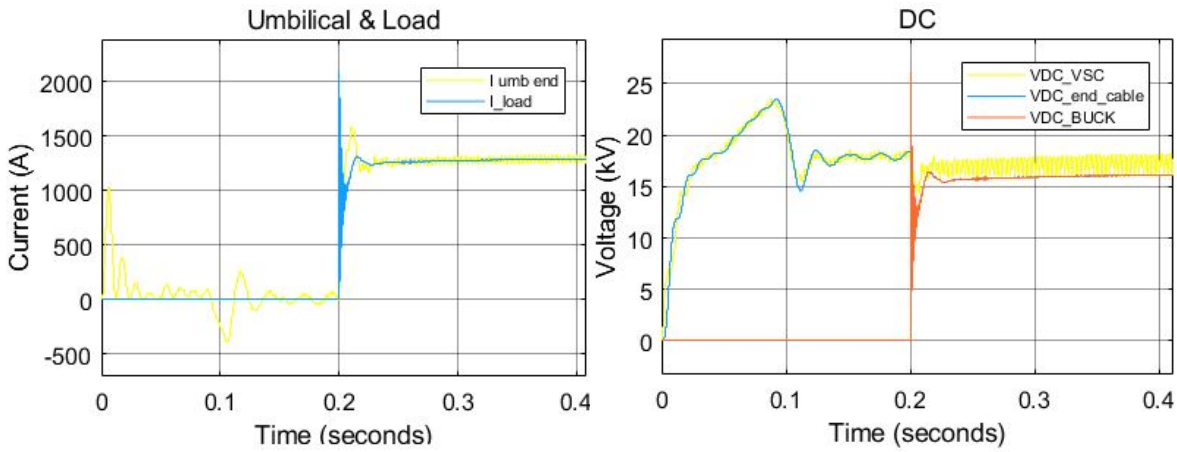

(a) $I_{umbilical}$(yellow), and I_{load}(blue).

(b) $V_{DC,VSC}$(yellow), $V_{end,cable}$(blue) and $V_{DClink,buck}$(red).

Figure 6.8: Currents and voltages for case 3.

6.4.4 Case 4

Case 4 presents a case closer to the real start-up of the systems, both converters have their own precharge circuit. The inrush currents are reduced avoiding damage to the equipment and any potential spurious trip of the protection system. The simulation results are depicted in Figs. 6.9a and 6.9b.

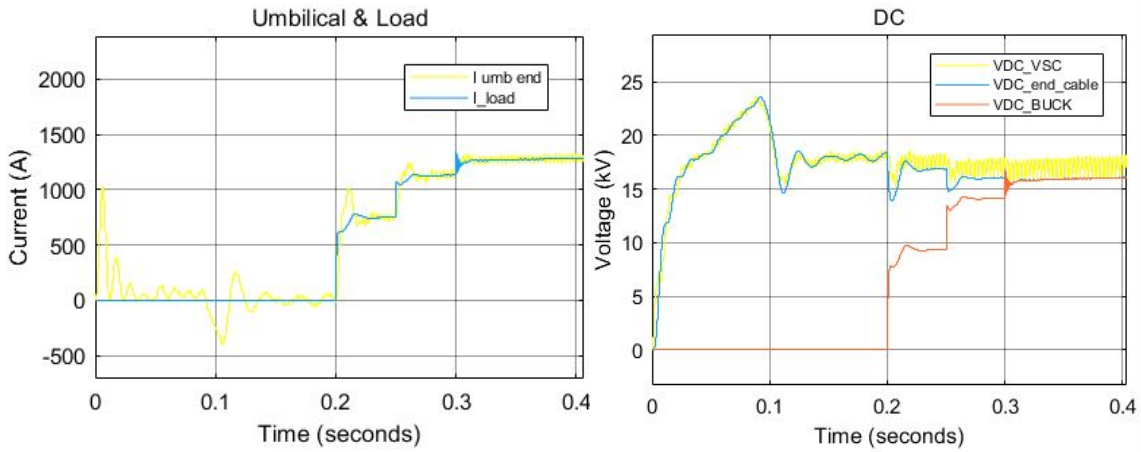

(a) $I_{umbilical}$(yellow), and I_{load}(blue).

(b) $V_{DC,VSC}$(yellow), $V_{end,cable}$(blue) and $V_{DClink,buck}$(red).

Figure 6.9: Currents and voltages for case 4.

6.5 Ideal Source and Lvsc = 1.05 mH

During the design of the VSC, the method explained in chapter 5.1.1 was used to define the line reactance of the converter. Using the equation 5.1 and considering that all converters and motors in the subsea loads have an average efficiency of 90%, as well as the converter, and with a target of 5% of voltage drop, the line reactance would be:

$$I_{\mathrm{DC}} = \frac{14\mathrm{M}}{18\mathrm{k} \cdot 0.9 \cdot 0.9} = 960\mathrm{A} \quad \text{and} \quad \mathrm{L_{VSC}} = \frac{0.05 \cdot 6350}{100\pi \cdot 960} = 1.05\mathrm{mH} \tag{6.1}$$

However, this reactance gives considerable poor results regarding the converter performance and power quality. The main three issues are listed below:

Excessive voltage ripple in the topside DC-link and power cable

Fig. 6.10 shows the DC voltages in the system. The ripple is 4800 kV peak-to-peak, almost the same value as the RMS voltage of 15 kV. The voltage ripple is reduced along the power cable, ending more stable at the input terminals of the subsea converter.

Fig. 6.11 depicts the DC currents in the power cable and the subsea load. The cable current has a ripple of 150 A, while the load current has a ripple of 35 A.

The plots of voltages and currents have the peak transients removed intentionally. The transient behavior of the signals was evaluated in section 6.4. The focus in the next four sections is in the steady-state value, and so, the scales are reduced to the better reading of the steady-state values.

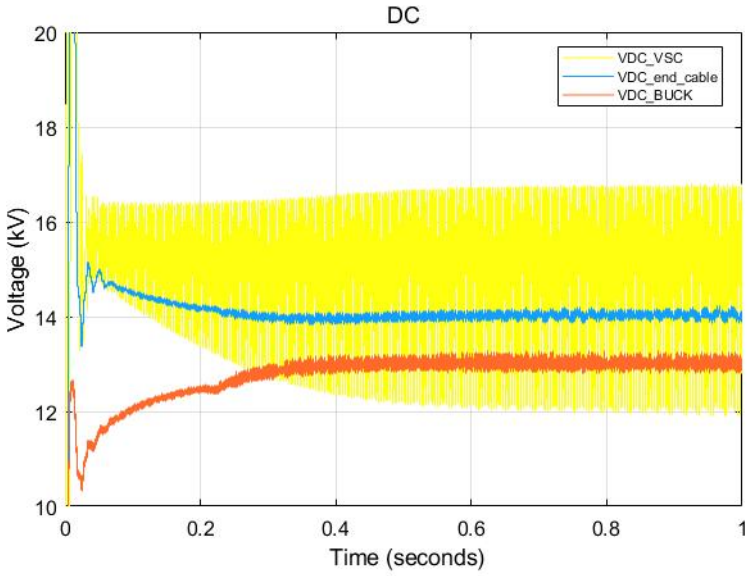

Figure 6.10: DC voltages with L=1.05 mH, topside DC-link voltage (yellow), voltage in the end of the power cable (blue), and subsea DC-link (red).

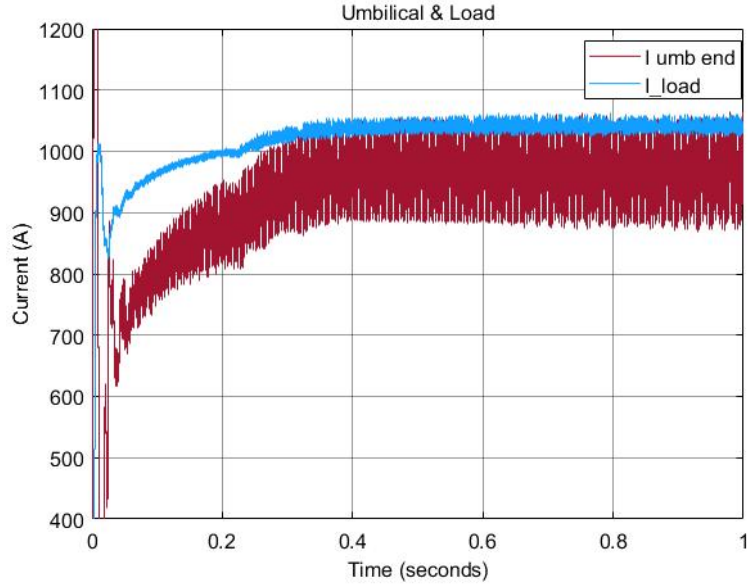

Figure 6.11: DC currents with L=1.05 mH, current in the power cable (red) and load current (blue).

Excessive DC-link capacitor current

Fig. 6.12 shows the current in the DC-capacitors. The capacitor current presents a large ripple with an RMS current of 2195 A. This current is not reasonable for the design of such capacitor, since such high current is more than two times the total current required to feed all subsea loads. All values for the DC system can be seen in table 6.7 below.

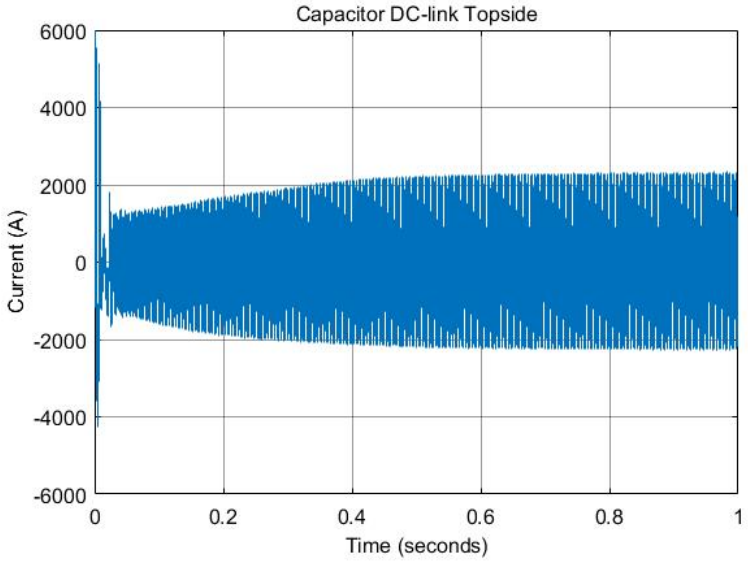

Figure 6.12: DC-link current with L=1.05 mH.

Table 6.7: Voltage and current measurements on the DC-side.

Parameter	**Value**	**Ripple (pk-pk)**	**Ripple (%)**
DC-link VSC voltage	15 kV	4390 V	29.2 %
VSC capacitor current ripple	2195 A	4446 A	-
Cable end voltage	14 kV	200 V	1.4 %
Cable current	1014 A	150 A	14.8 %
DC-link buck voltage	13 kV	400 V	3 %
Buck capacitor current ripple	530 A	2000 A	-
Buck load current	1043A	37 A	3.5 %

6.5.1 AC Harmonic Content

The system sends a substantial amount of harmonics back to the AC-grid, in Fig. 6.13 the FFT analysis shows a THD_i of 73.36 % with the 5^{th} and 7^{th} contributing the most, with approximately 70 % and 14 % of the fundamental current respectively. Such high harmonic content must be present due to the overmodulation in the VSC. The system probably would not become stable if connected to a non-ideal source. Components with a contribution lower than 5 % are not shown in the plot.

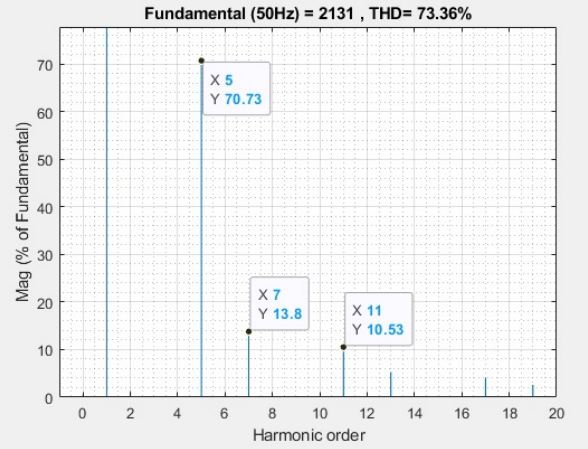

Figure 6.13: AC current harmonics with L=1.05 mH.

So, based on the exposed results, the line reactance used from this point onwards is 4.1 mH, which was obtained during the optimization of the topside converter.

6.5.2 DC Harmonic Content

The DC harmonics are shown using the modulation m_f as the fundamental component [74, 75]. The topside converter has a frequency carrier of 10 kHz and the AC grid frequency is 50 Hz, so the fundamental frequency will be $m_f = 10000/50 = 200$. Later, for the buck converter evaluation, the m_f is changed to 400, due to the frequency carrier of 20 kHz. The frequency range shown in the graphs adapts to the harmonic content of the signal, and, therefore it may slightly change from one to another signal.

Topside converter and power cable (m_f=200)

Fig. 6.14a shows the harmonic content of the voltage in the VSC DC-link. The plot shows a very small quantity of harmonics, the signal is mostly DC, with two main component at low frequencies: $V_{300Hz} = 2\,kV$ and $V_{600Hz} = 375\,V$.

It worth mentioning that the DC harmonic spectrum presents harmonic components at $300n$ Hz, where n is an integer. The same behavior occurs when an ideal current source replaces the buck converter. These harmonic components are directly related to the six IGBTs of the VSC and the AC network frequency. When the AC system is changed from 50 Hz to 60 Hz the DC harmonics are displaced to 360 Hz, 720 Hz, and so on. So, it is expected that the harmonics in the further cases follow the general formula below, for the 18 kV segment of the grid:

$$F_{DC}^{n} = k_{sw} \cdot n \cdot f_{AC} \tag{6.2}$$

Where:
F_{DC}^{n} is the DC harmonic frequency n, where n is an integer
$\mathrm{k_{sw}}$ is the number of switches in the converter, which is 6 in this report
f_{AC} is the AC frequency of the grid

Fig. 6.14b shows the result for the end of the power cable, at the input of the buck converter. It can be seen that the cable inductance acts as a filter, as expected, reducing the 300 Hz component from 13.5 % to 0.5 %, improving the the buck converter input voltage.

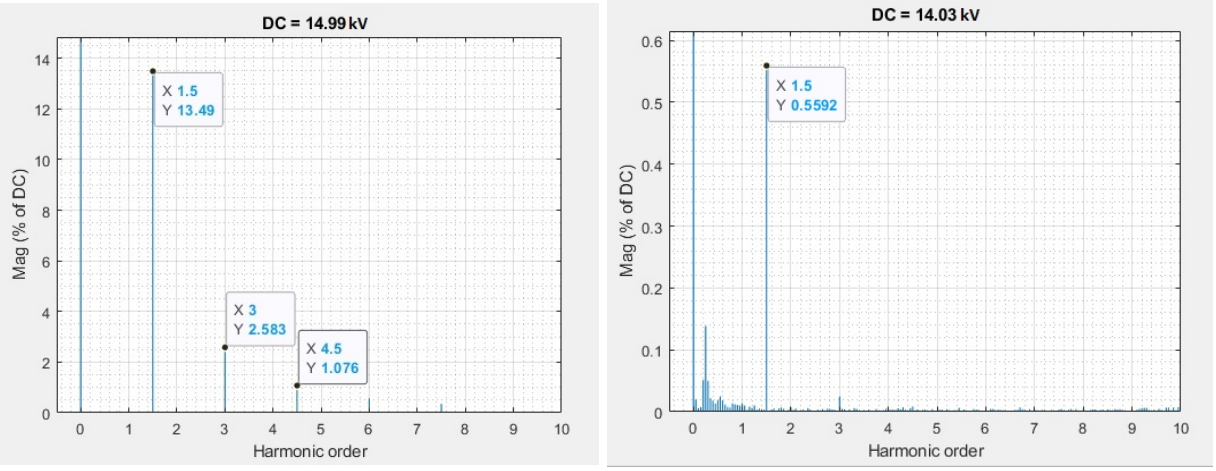

(a) VSC DC-link voltage.

(b) Voltage at the power cable end.

Figure 6.14: Harmonic spectrum of the DC voltages.

Fig. 6.15a shows the harmonic content for the current flowing in the power cable similar to the voltage the main harmonic component is the 300 Hz component, with 82 A. While Fig. 6.15b depicts the spectrum for the ripple current from the capacitor at the VSC DC-link. The values are presented in ampere, and not as a percentage of the DC component, since there is no DC component. The main contributions are at $300n$ Hz, with $1 \leqslant n \leqslant 5$.

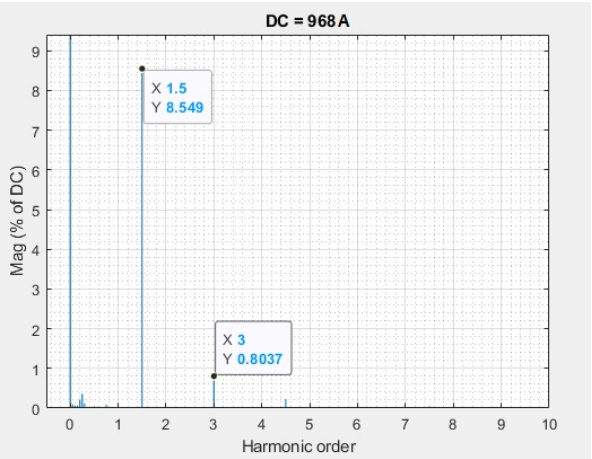

(a) Power cable current.

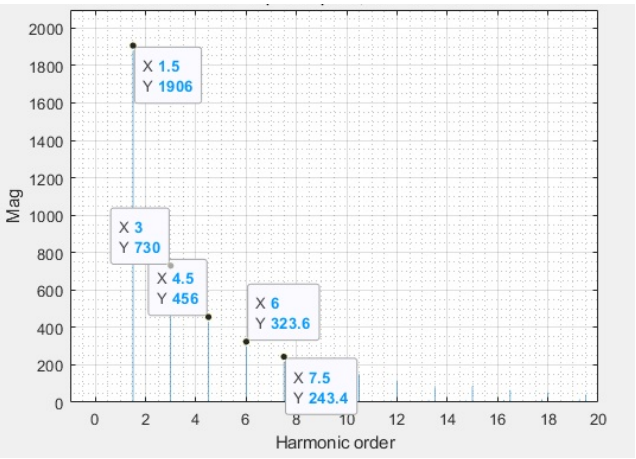

(b) VSC DC-link capacitor.

Figure 6.15: Harmonic spectrum of the DC currents.

Subsea converter (m_f=400)

Figs. 6.17a and 6.17b show the THD_v and THD_i for the output DC-link voltage and load current respectively. Differently from the the VSC the voltage and current of the buck converter present a considerabe contribution for several harmonics. The harmonics are concentrated around 3.6 kHz in both cases. The voltage spectrum shows also a contribution at a low frequency of 300 Hz with 2.8 kV, which is originated from the input side of the converter.

When the buck converter is simulated with an ideal DC source in the input side the main DC harmonics contributions occur at $1080n$ Hz, with $n \geqslant 1$, with negligible side bands, see Fig. 6.16, however such harmonics changed when the buck converter is inserted in the DC-grid.

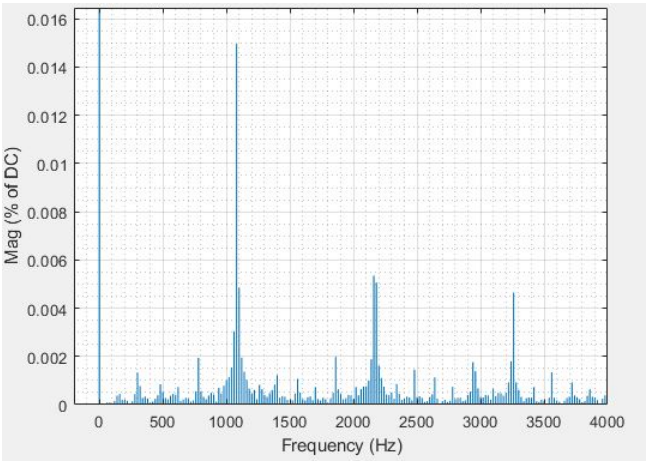

Figure 6.16: Example of harmonic spectrum of the buck converter voltage with an ideal DC input source.

Fig. 6.18 presents the spectrum of the capacitor current. Different from the topside DC capacitor the majority of the harmonics are at high frequencies. The behavior seen in Fig. 6.16 also occurs at the DC-link capacitor, however, when connected to the DC-grid, a completely new harmonic spectrum appears. Showing that the capacitors in the subsea DC-link will be influenced by the harmonics from the topside VSC.

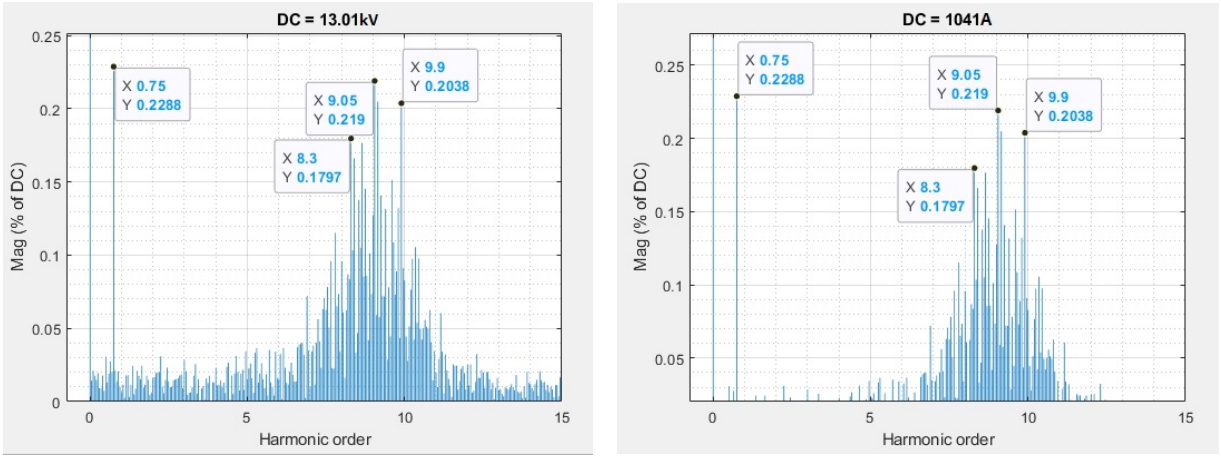

(a) Buck DC-link voltage.

(b) Load current.

Figure 6.17: Harmonic spectrum of DC voltage and current to the loads.

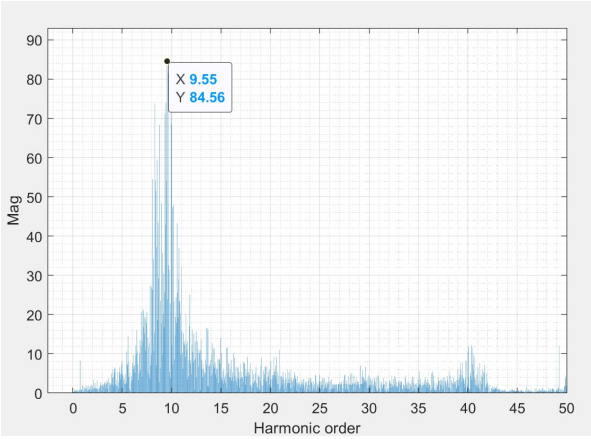

Figure 6.18: DC-link subsea harmonic currents in absolute Ampere values.

6.6 Ideal Source and Lvsc = 4.1 mH

This section presents the results of an increased line reactance of the VSC from 1.05 mH to 4.1 mH. Fig. 6.19 shows the plot of the DC voltages in the system, while Fig. 6.20 shows the DC currents.

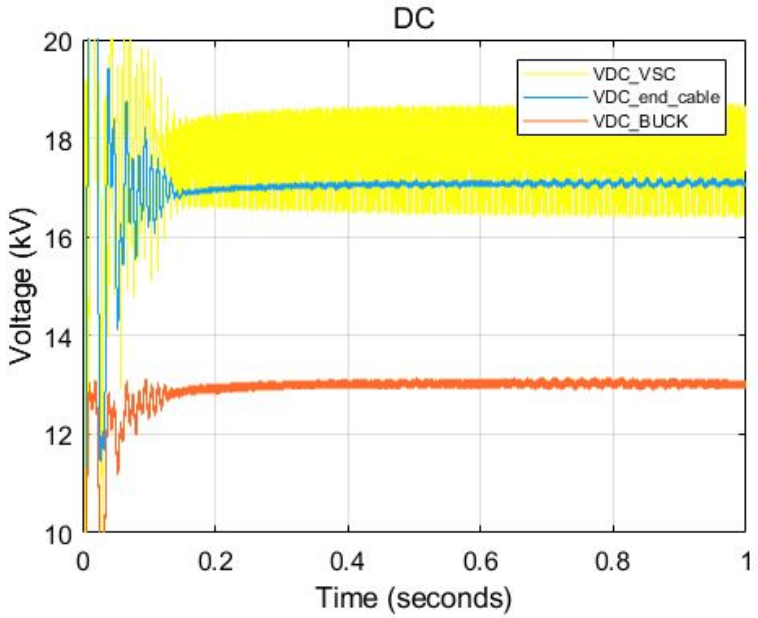

Figure 6.19: DC voltages with L=4.1 mH, topside DC-link voltage (yellow), voltage in the end of the power cable (blue), and subsea DC-link (red).

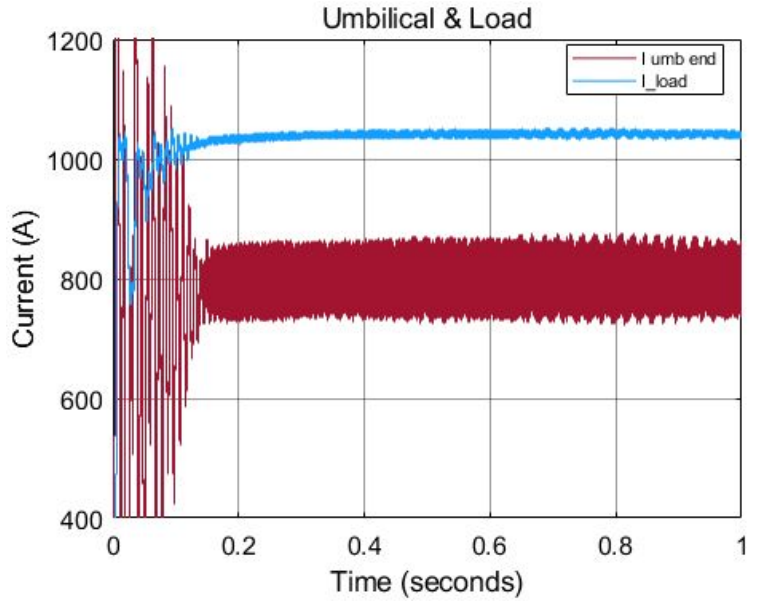

Figure 6.20: DC Currents with L=4.1 mH, umbilical current (blue) and load current (red).

Table 6.8 presents the values with the new reactance. It can be seen that the performance of the system has improved substantially in the DC-side. The output voltage in the DC-link cable increases to 17.8 kV. The voltage and current ripples decreased drastically, highlighting the voltage at the topside DC-link, where the ripple decrease from 29.2% to 12.2%.

Table 6.8: Voltage and current measurements on the DC-side.

Parameter	**Value**	**Ripple (pk-pk)**	**Ripple (%)**
DC-link VSC voltage	17.8 kV	2184 V	12.2 %
VSC capacitor current ripple	938 A	2518 A	-
Cable end voltage	17.2 kV	200 V	1.1 %
Cable current	807 A	142 A	17.6 %
DC-link buck voltage	13 kV	150 V	1.1 %
Buck capacitor current ripple	1837 A	2979 A	-
Buck load current	1048 A	25 A	0.9 %

6.6.1 AC Harmonic Content

Fig. 6.21 confirms the line reactance as a harmonic mitigation solution. The THD_i reduced from 73.36% to 22.57%, showing a relevant reduction in all harmonic components.

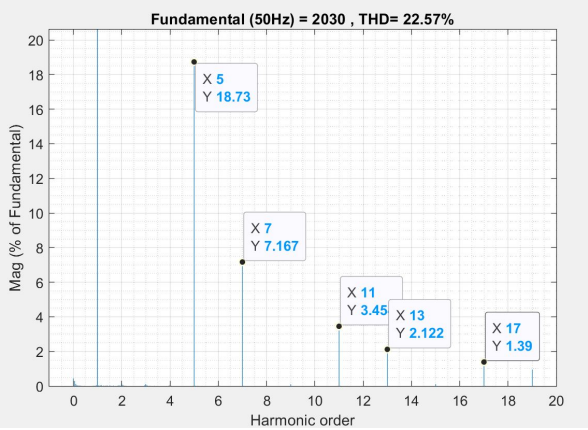

Figure 6.21: AC current harmonics with L= 4.1 mH.

6.6.2 DC Harmonic Content

The previous sections described the benefits of increasing the line reactance, however it is important to evaluate how the high frequency components of the currents and voltages will behave after this change.

Topside converter and power cable (m_f=200)

Fig. 6.22a shows the harmonic content for the most relevant harmonics in the VSC DC-link. The plot explains why the ripple has reduced considerably, all the harmonic components are reduced.

Fig. 6.22b depicts the analysis of the voltage in the end of the cable. The harmonics above 300 Hz have been reduced or eliminated, and some new components appeared at low frequencies. However they are possibly originated from numerical noise, since they are not present in Fig. 6.22a.

And Fig. 6.23a shows the results for the current frequency spectrum.

Fig. 6.23b depicts the harmonic spectrum for the capacitor current. The plot shows the same harmonics from the previous case (L=1.05 mH), as expected. But with a substantial reduction in the magnitude due to the increasing of the VSC line inductance.

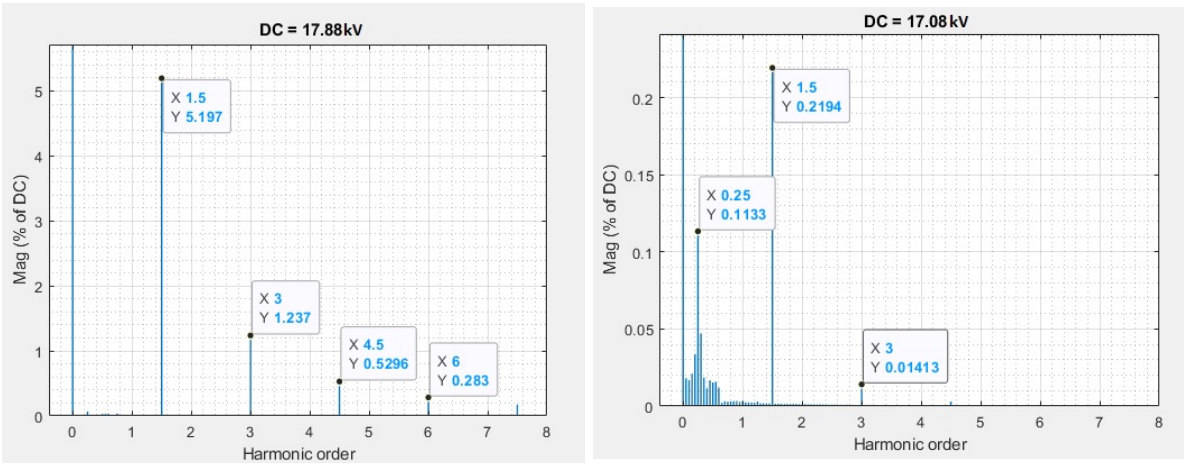

(a) VSC DC-link voltage.

(b) Voltage at the power cable end.

Figure 6.22: Harmonic spectrum of the DC voltages.

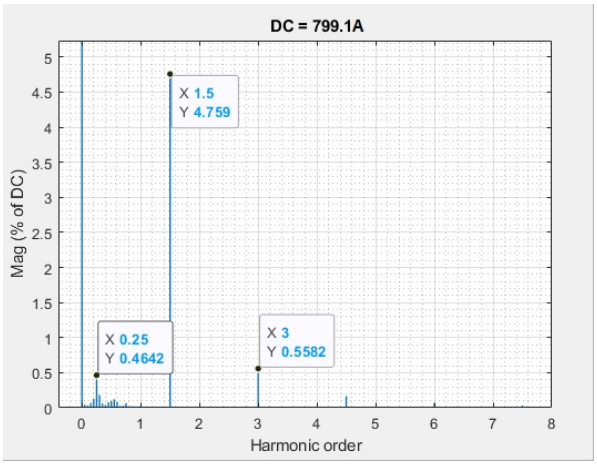

(a) Power cable current.

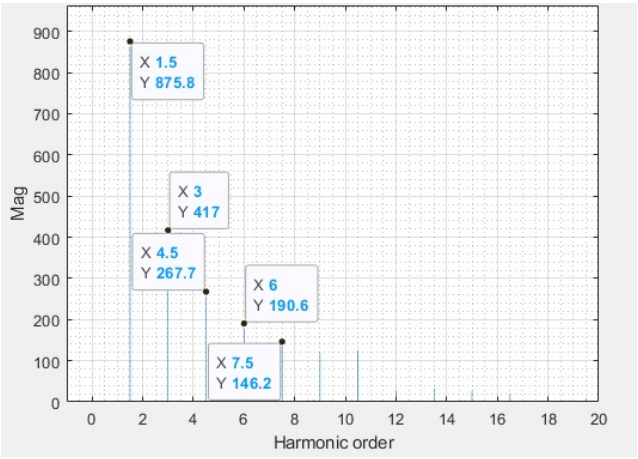

(b) VSC DC-link capacitor.

Figure 6.23: Harmonic spectrum of the DC currents.

Subsea converter (m_f=400)

Fig. 6.24a and 6.24b show that the increase of the line reactance causes a sizable improvement in the voltage and current of the subsea DC-link. Practically all high frequency components are removed. The high frequency components could generate Electromagnetic Interference (EMI) to the Printed Circuit Boards (PCB) and other power electronic components installed in the subsea vehicles.

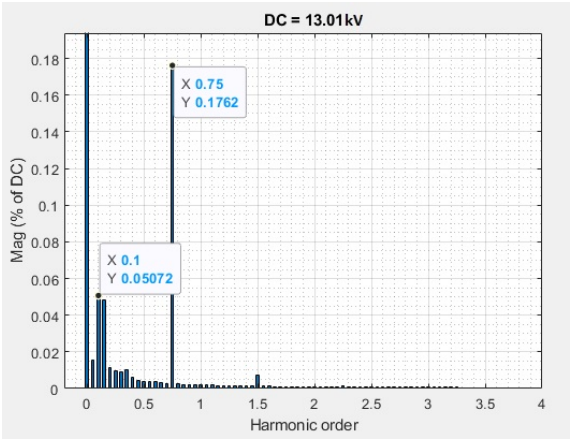

(a) Buck DC-link voltage.

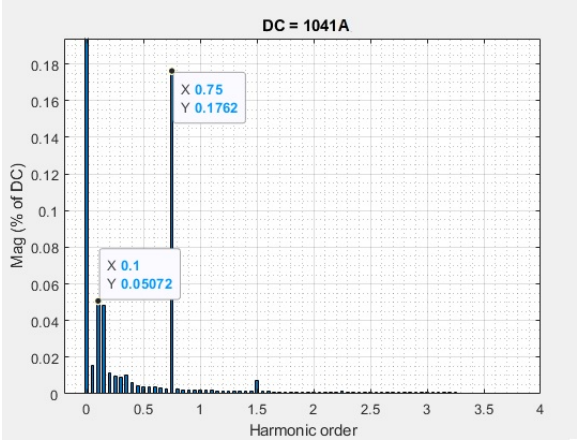

(b) Load current.

Figure 6.24: Harmonic spectrum of DC voltage and current to the loads.

Fig. 6.25 shows the harmonic spectrum for the ripple current in the subsea DC-link. The high frequency components are completely eliminated in the capacitor, except for the a component at 19.7 kHz. Despite the high frequency component, the main low frequency component remaining is the at 300 Hz with 7 A, originated form the VSC converter.

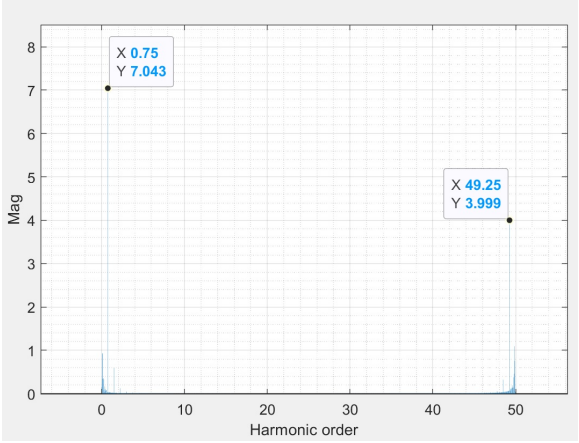

Figure 6.25: DC-link subsea harmonic currents in absolute Ampere values.

6.7 Non-ideal Source

This section evaluates the power quality in the system when a real source is employed. A real source, differently from the ideal source, has a limited short circuit capability and has an internal impedance. Consequently, limited short circuit capability will restrict the level of current harmonic distortion drawn by the source, generating distortions in the voltage.

In chapter 4.5.1 it was mentioned that the system upstream the PCC can be represented by a Thevenin equivalent. However, a good assumption is required regarding the Thevenin reactance.

The standard IEEE 242 [77] lists several common values for the reactance and X/R ratio for transformers and generators, and consequently, can be used as a reference.

In order to provide the required MVA to the power system the transformer, connecting the VSC converter, requires at least 16 MVA (assuming +15 % power margin). Now it is possible calculate the X_{base} for this transformer.

$$X_{base} = \frac{(11\,kV)^2}{16\,MVA} = 7.5625\Omega \tag{6.3}$$

Evaluating the standard [77], the closest transformer (15 MVA and 69 kV: 13.8 kV) has 8% of reactance. The author in [34] clearly exemplifies how important it is that the Thevenin impedance has a low reactance value. Either the Thevenin equivalent has a low reactance or a large short circuit level, otherwise the grid will behave like a "soft grid" and the voltage harmonic distortion will be above the limits.

Thus, using 8 % for the transformer the reactance will be

$$L_s = \frac{7.5625 \cdot 0.08}{2 \cdot \pi \cdot 50} = 1.924m\text{H} \tag{6.4}$$

The source connected upstream the VSC was changed from an ideal to non-ideal source and the simulation of the system was performed again. The results are presented throughout this chapter.

Figs. 6.26 and 6.27 depict the DC voltages and currents respectively. The system is stable, however a natural increase in the voltage ripple occurs.

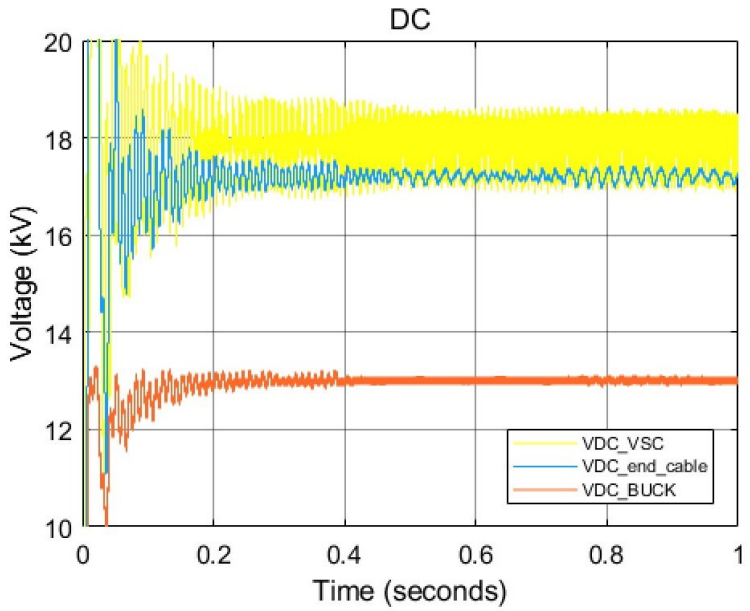

Figure 6.26: DC voltages with non-ideal source, topside DC-link voltage (yellow), voltage in the end of the power cable (blue), and subsea DC-link (red).

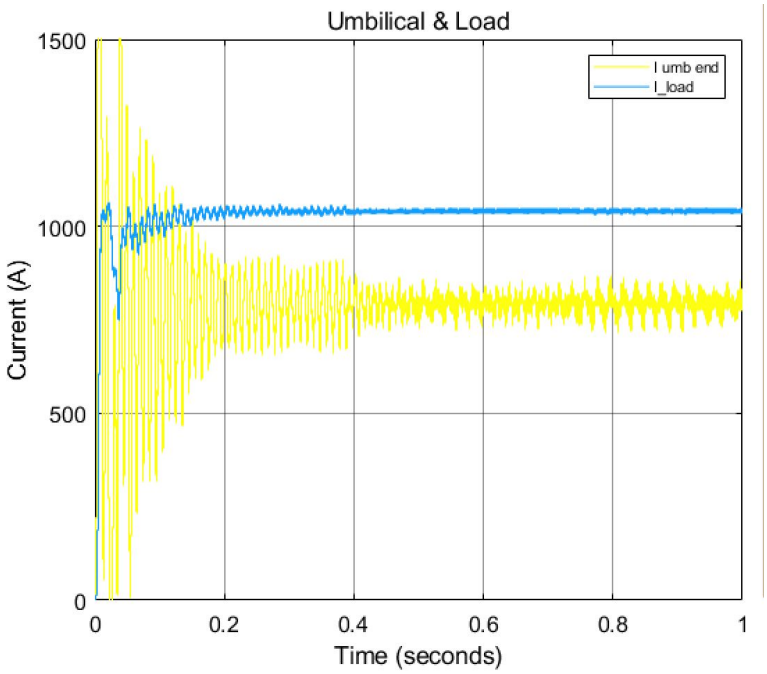

Figure 6.27: DC currents with non-ideal source, umbilical current (yellow) and load current (blue).

Table 6.9 presents the values for current and voltage in steady-state for the system simulated with the non-ideal source. A reduction in the voltage ripple in both DC-links can be observed while the current ripple shows a small increase. The I_{RMS} current in the DC-link capacitors

have reduced both topside and subsea.

Table 6.9: Voltage and current measurements on the DC-side.

Parameter	**Value**	**Ripple (pk-pk)**	**Ripple (%)**
DC-link VSC voltage	18 kV	1500 V	8.3 %
VSC capacitor I_{RMS} ripple	613 A	1800 A	-
Cable end voltage	17.3 kV	500 V	2.8 %
Cable current	791 A	160 A	20 %
DC-link buck voltage	13 kV	350 V	2.7 %
Buck capacitor I_{RMS} ripple	1728 A	3000 A	-
Buck load current	1040 A	17 A	16.3 %

6.7.1 AC Harmonic Content

This section discusses the results of the harmonic content in the AC-side of the system, when the non-ideal source is presented in the simulation. Figs. 6.28b and 6.28a portrait the AC harmonic spectrum and THD for the grid voltage and current respectively. Since the source is no longer ideal, the harmonic distortion appears in the line voltages with a THD_v of 15.76 %, which is high [59]. The reference states that the THD_v shall be maximum 8 % with no single harmonic order exceeding 5 %.

The plot in 6.28b also shows a high 5^{th} harmonic content that must be reduced.

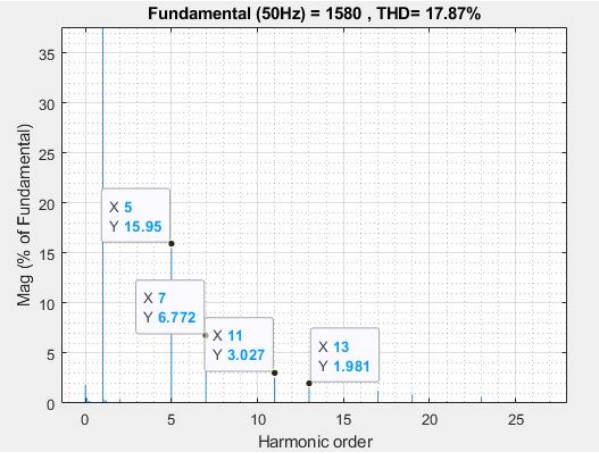

(a) AC current with L= 4.1 mH - non-ideal source.

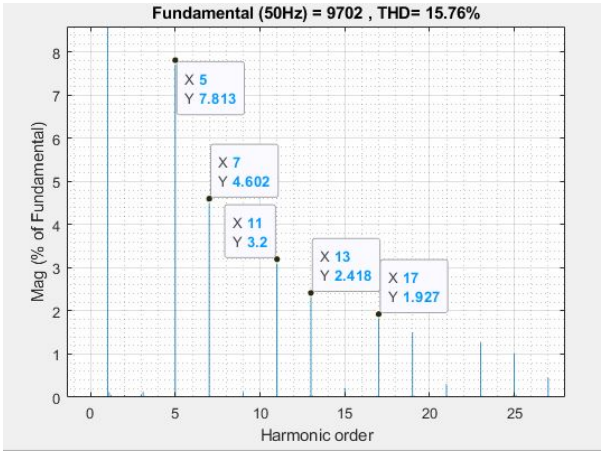

(b) AC voltage with L= 4.1 mH - non-ideal source.

Figure 6.28: Harmonic spectrum of the AC signals.

6.7.2 DC Harmonic Content

This section discusses the effects of a non-ideal source in the harmonic content of the DC-side of the system.

Topside converter and power cable (m_f=200)

Fig. 6.29a presents a natural increasing in all harmonic components when compared to an ideal source. Fig. 6.29b shows how the inductance in the power umbilical can filter most of the harmonic components, except for a low frequency 50 Hz which appear with a small amplitude of 153 V.

The 50 Hz-component is higher in the DC-current in the power umbilical, as can be seen in 6.30a. The component increased from 3.6 A to 23 A. All other components are reduced.

And at last, Fig. 6.30b presents the harmonic components in the DC-link capacitor. The plot shows a general reduction in the current harmonic content, which is expected since the harmonic content in the voltage has increased.

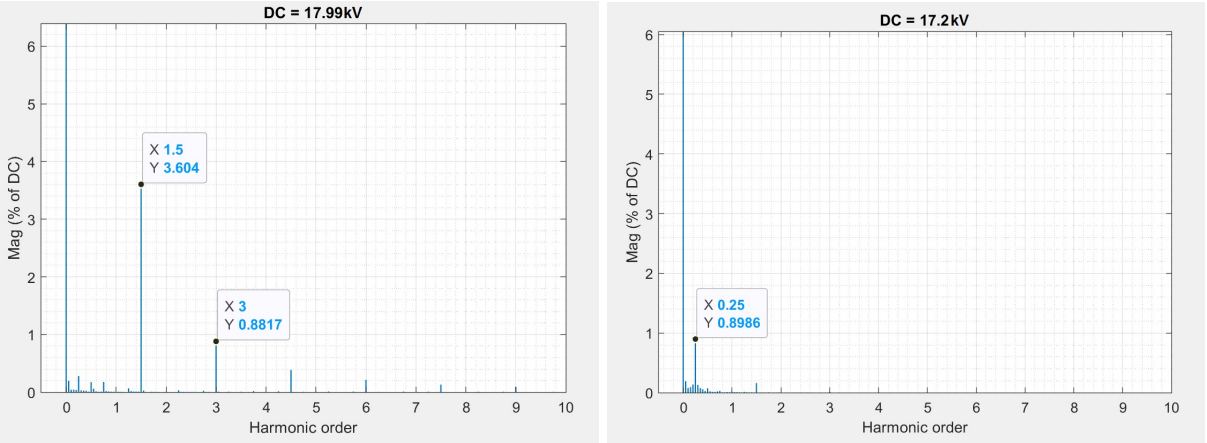

(a) VSC DC-link voltage.

(b) Voltage at the power cable end.

Figure 6.29: Harmonic spectrum of the DC voltages

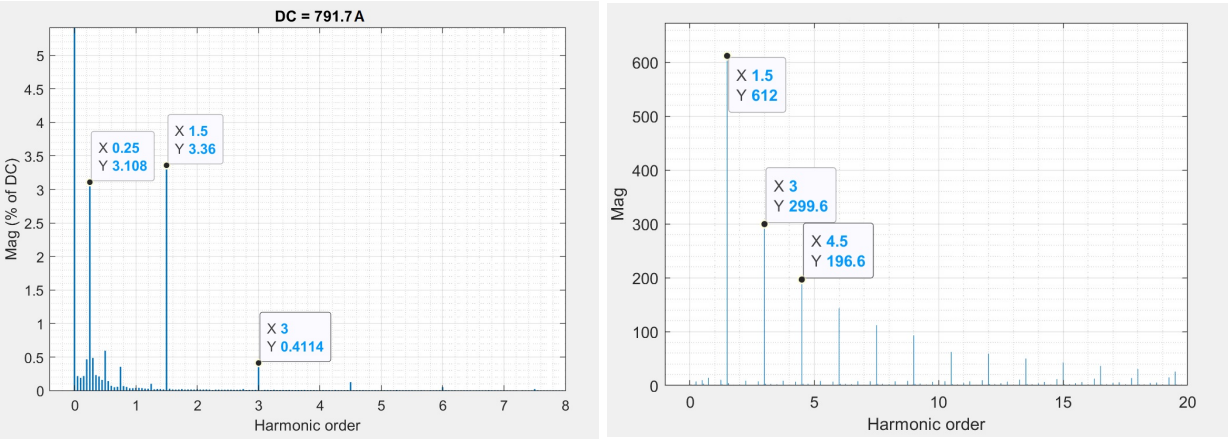

(a) Power cable current.

(b) VSC DC-link capacitor.

Figure 6.30: Harmonic spectrum of the DC currents.

Subsea converter (m_f=400)

Regarding the harmonic content in the subsea converter there is a change in the spectrum for both current and voltage. With an ideal source the spectrum was mostly DC with a small portion of 300 Hz (0.17 % of the DC quantity). With an non-ideal source this contribution has reduced to less then 0.1 %. Figs. 6.31a and 6.31b present the plots of voltage and current, respectively.

Fig. 6.32 presents the current in the capacitor with a main high frequency component at 19.8 kHz and several small components in basically the entire spectrum from 2 kHz to 20 kHz.

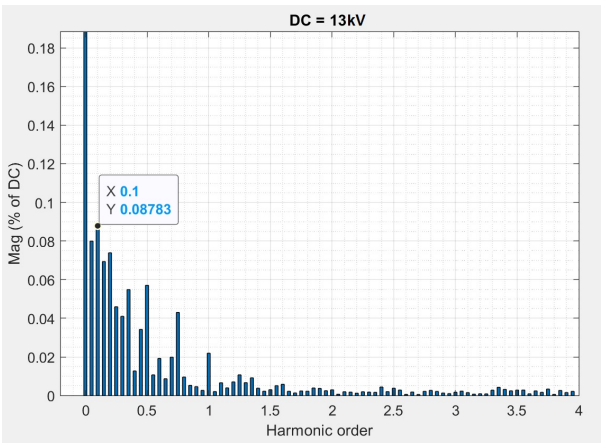

(a) Buck DC-link voltage.

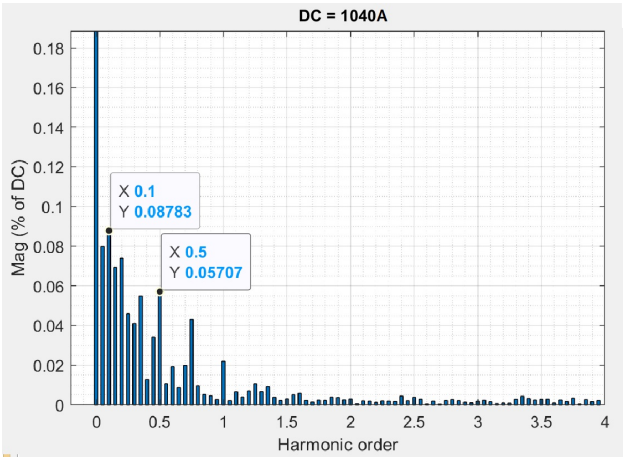

(b) Load current.

Figure 6.31: Harmonic spectrum of DC voltage and current to the loads.

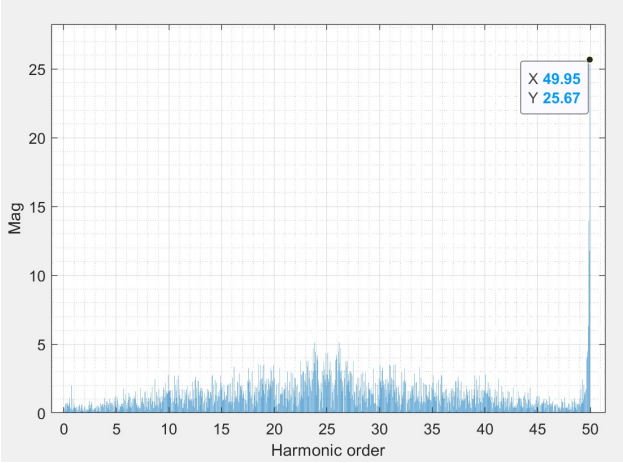

Figure 6.32: DC-link subsea harmonic currents in absolute Ampere values.

6.8 Non-ideal Source with passive filter

This section presents the results when a passive LC-filter is added to mitigate the harmonics in the AC voltage. The filter is connected to the PCC aiming to reduce the 5^{th} harmonic, which has the main contribution for the voltage distortion.

The passive compensation is an optimization method that may lead to interaction between the filter and the grid. Initially, trying one LC filter tuned at 250 Hz, a parallel resonance occurred at 175 Hz, see Fig. 6.33a. Then, a damping factor of R=1 Ω is added to the filter, reducing the parallel resonance, Fig. 6.33b.

However, with only one filter the harmonic content was still above 8 % for the THD_v, see Fig. 6.34a. Then, another passive filter is added to reduce the harmonic content to acceptable levels. The final impedance diagram can be seen in Fig. 6.34b.

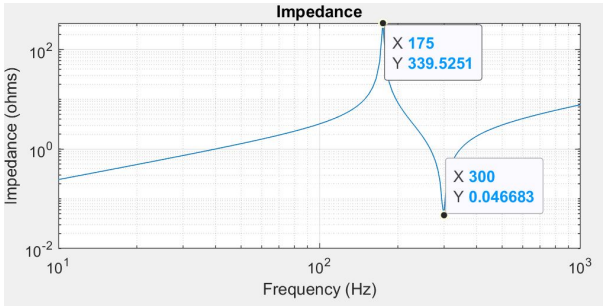

(a) Impedance diagram with one LC filter.

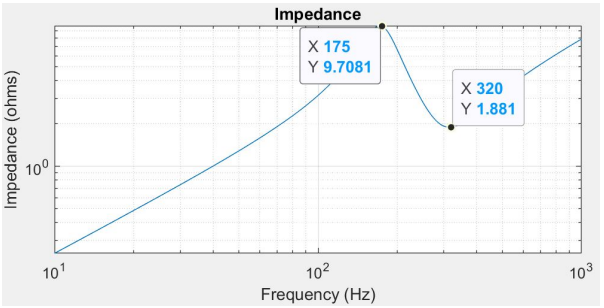

(b) Impedance diagram with one LCR filter.

Figure 6.33: Impedance diagrams.

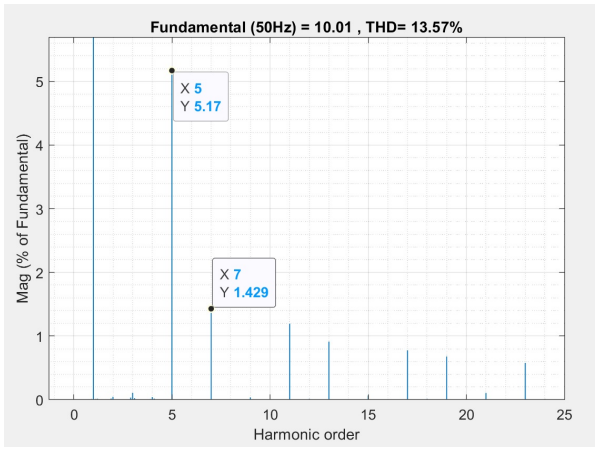

(a) AC voltage harmonic spectrum with 1 filter, up to 1250 Hz.

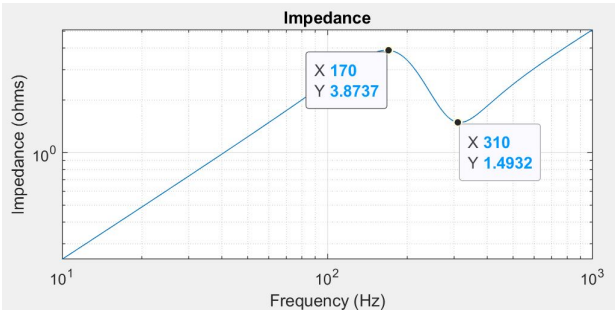

(b) Impedance diagram with two LCR filters.

Figure 6.34: Impedance diagrams (cont.).

The parameters of the filters implemented in the system are depicted in table 6.10. Fig. 6.35

shows how the filters are connected to the PCC.

Table 6.10: Filter parameters.

	R_f	L_f	C_f
Filter 1	1 Ω	1 mH	280 µF
Filter 2	3 Ω	1 mH	210 µF

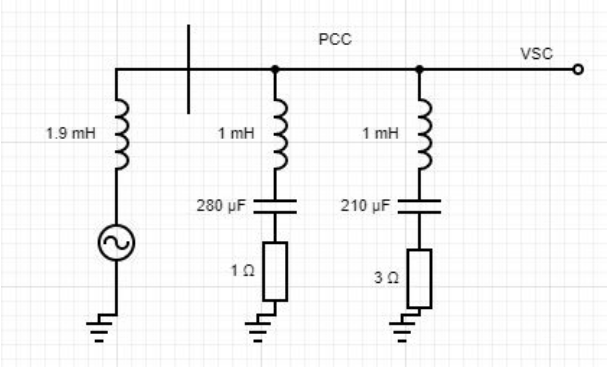

Figure 6.35: Single line diagram showing the filters connected to the PCC.

Figs. 6.36 and 6.37 show the DC voltages and currents for the system with the passive filters respectively. Table 6.11 presents the values for the DC system.

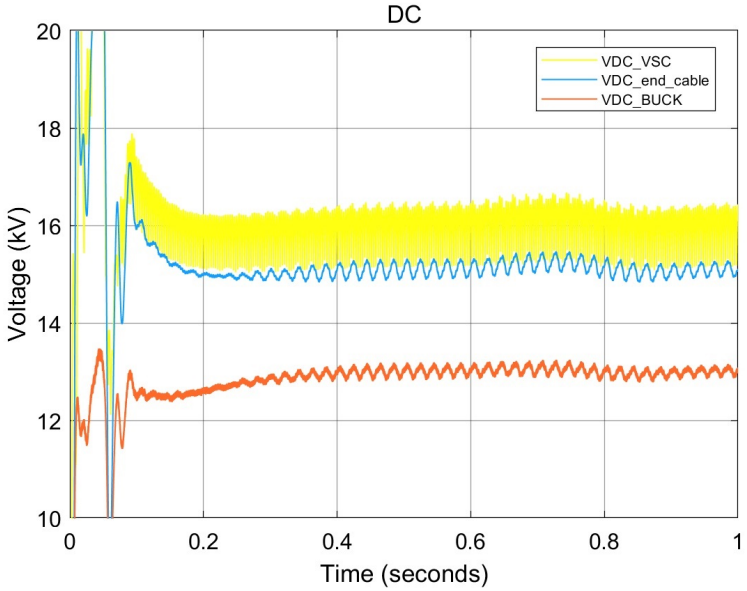

Figure 6.36: DC voltages with non-ideal source and passive filters, topside DC-link voltage (yellow), voltage in the end of the power cable (blue), and subsea DC-link (red).

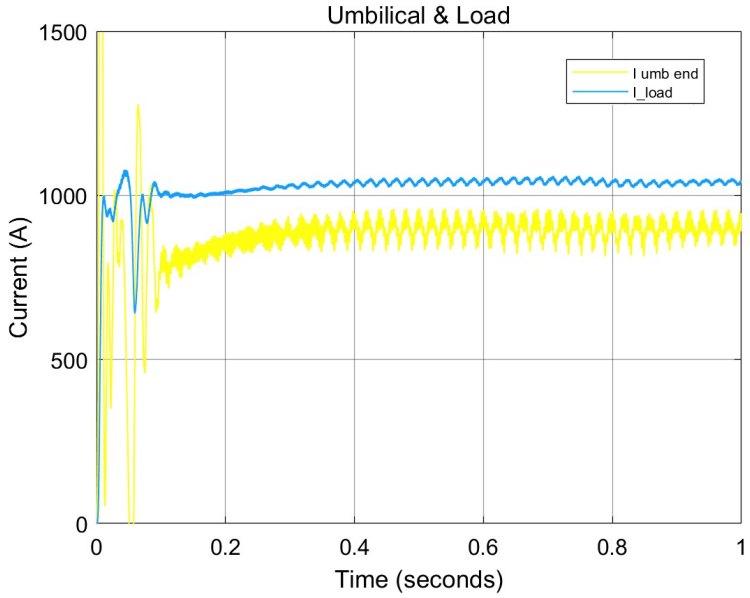

Figure 6.37: DC currents with non-ideal source and passive filters, umbilical current (yellow) and load current (blue).

Table 6.11: Voltage and current measurements on the DC-side.

Parameter	**Value**	**Ripple (pk-pk)**	**Ripple (%)**
DC-link VSC voltage	17.6 kV	1360 V	7.7 %
VSC capacitor I_{RMS} ripple	520 A	1600 A	-
Cable end voltage	16.8 kV	300 V	1.8 %
Cable current	813 A	100 A	11 %
DC-link buck voltage	13 kV	200 V	1.5 %
Buck capacitor I_{RMS} ripple	1643 A	3000 A	-
Buck load current	1045 A	12 A	1.1 %

6.8.1 AC Harmonic Content

Figs. 6.37 and 6.36 show the harmonic contents for the current and voltage respectively in the AC-side after the filter implementation. The THD_v reduced to 5.75 %, with individual harmonic content 3.74 % of the fundamental. Thus, the harmonic requirement at the PCC is fulfilled.

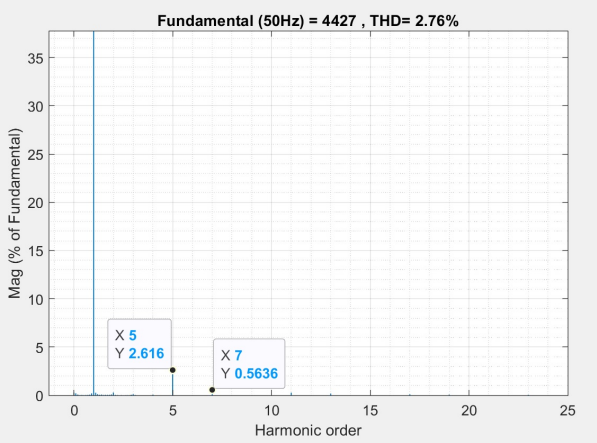

(a) AC current - non-ideal source with filter.

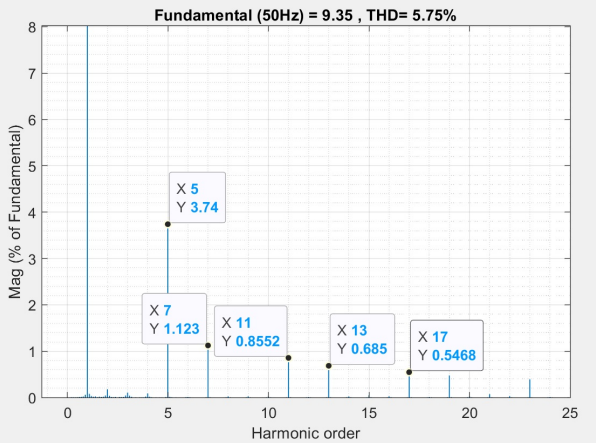

(b) AC voltage - non-ideal source with filter.

Figure 6.38: Harmonic spectrum of the AC signals.

6.8.2 DC Harmonic Content

Topside converter and power cable (m_f=200)

Figs. from 6.39a to 6.40b show the effects in the DC-side after the passive filters. There is a general minor harmonic reduction when compared to the scenario without the filters, see section 6.7.

A similar result occurs in the subsea load and DC-link voltage, Fig. 6.41a and 6.41b.

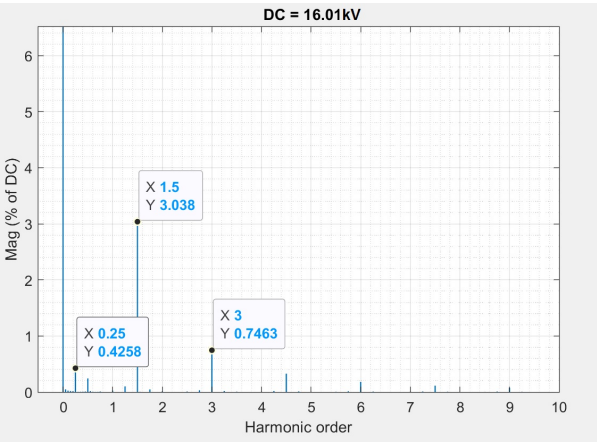

(a) VSC DC-link voltage.

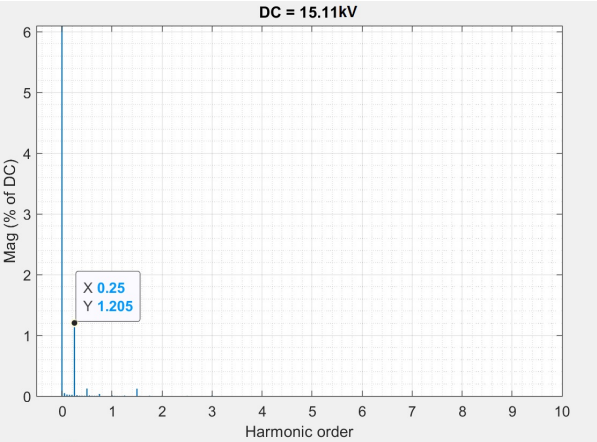

(b) Voltage at the power cable end.

Figure 6.39: Harmonic spectrum of DC voltages.

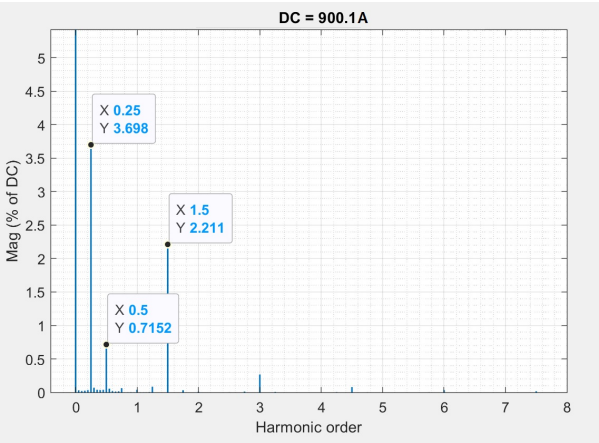

(a) Power cable current.

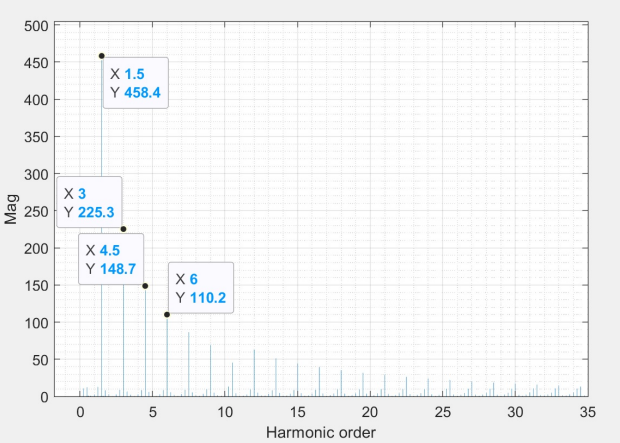

(b) VSC DC-link capacitor.

Figure 6.40: Harmonic spectrum of the DC currents.

Subsea converter (m_f=400)

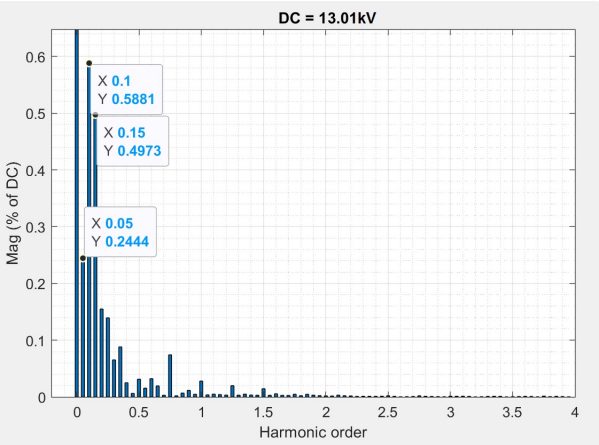

(a) Buck DC-link voltage.

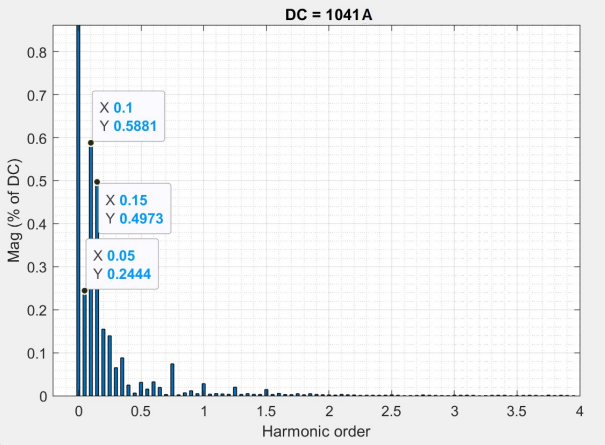

(b) Load current.

Figure 6.41: Harmonic spectrum of DC voltage and current to the loads.

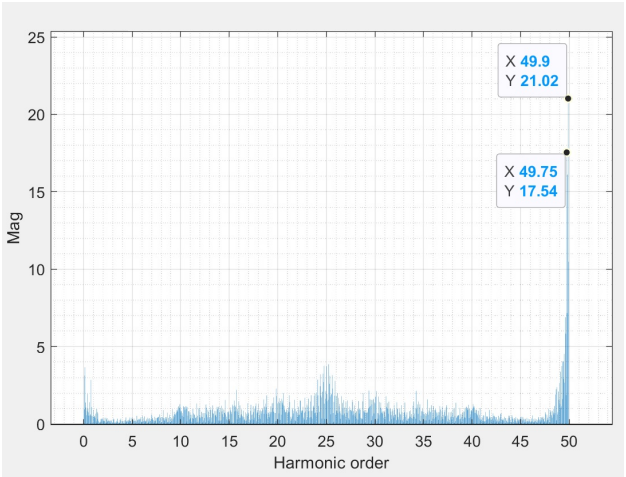

Figure 6.42: DC-link subsea harmonic currents in absolute Ampere values.

Chapter 7

Conclusion and Further Work

A DC power system for DSM applications is designed to investigate power quality aspects. Poor power quality may become an issue not only for the subsea loads but also for the topside grid, since diesel generation, often implemented in offshore vessels, are well-known as weak power sources. The system is designed with a Thevenin circuit representation of the topside system, two converters, one responsible for the topside DC-link and another responsible for the subsea DC-link, an umbilical cable and a resistive load representing the total system power demand. The topside converter is a VSC type while the subsea is a buck type. The control system for both converters are implemented by PWM technique and validated separately before being integrated into the power system.

The system is evaluated by testing two distinct aspects. The first is the evaluation of the system performance regarding different load operation conditions, start-up function, and load disturbances. The system shows a stable voltage at the subsea DC-bus; this was possible due to the decision of using a step-down DC converter together with two distinguished voltage levels for transmission (18 kV) and distribution (13 kV). As long as the transmission voltage holds the minimum voltage level of the buck converter output, which is 13 kV in this system, the subsea DC-link regulates the voltage properly without any excessive ripple or voltage dips. Thereby, the subsea loads are protected of any possible power variation from the topside system.

In scenarios presenting disturbances originated by the subsea loads, e.g., disconnection of one of the subsea consumers due to a fault, the system reacts quickly returning the voltage to the operation point in less than one second.

The second aspect evaluated was the power quality of the system focusing on the DC side, but also briefly checking the AC side.

Two well-known harmonic mitigation technique has been evaluated and their impact on the DC side of the grid. The results demonstrate that the line reactance upstream the topside converter

has a substantial effect on the power quality of the DC-grid. Increasing the reactance above the standard values used for AC harmonic mitigation, it can be seen that the high-frequency harmonic components are reduced considerably in both current and voltage. This action also improves the quality in the capacitor current in the DC-links, both topside and subsea, reducing drastically the high-frequency content, which is very harmful to PCB regards Electromagnetic Interferences due to the emission of noise from the DC-bus.

The passive filter has a marginal contribution to the quality in DC-grid, despite being very efficient to improve the quality of the voltage in the AC-grid. They reduce the harmonic content lightly in the currents and voltages of the DC-grid.

The thesis results look promising; however, the results are still preliminary since the further details regarding the topside power generation and the Voltage Source Inverters representing individual loads are not present in this model.

For further work, it is suggested replace the power cable from the pi-model to a traveling wave model to see any potential change due to the switching frequency of the converters. Besides, a proper inverter can be modeled and connected to the subsea DC-bus, this would allow a proper evaluation of the harmonics propagating from the subsea DC-bus to the AC subsea loads.

Bibliography

[1] E. Frimanslund. Feasibility of deep-sea mining operation within norwegian jurisdiction. Master's Thesis, NTNU, June 2016.

[2] R. Handschuh et al., "Innovative Deep Ocean Mining Concept based on Flexible Riser and Self-propelled Mining Machines", in *4th ISOPE Ocean Mining Symposium*, Polan, 2001.

[3] K. Richardson "A Perspective of Marine Mining Within De Beers. *The Journal of The Southern African Institute of Mining and Metallurgy*, pp. 393-402, June 2007.

[4] I. Lipton, "Mineral Resource Estimate - Nautilus Minerals, Technical Report, March 2012.

[5] http://www.nautilusminerals.com

[6] D. S. Silva. Power Quality Evaluation for Power System Design for Deep Sea Mining Application. Specialization Project, NTNU, January 2019

[7] Nautilus Minerals. General updates. April 2016.

[8] Y. C. Beaudoin, E. Baker, Deep Sea Minerals and the Green Economy. Book, December 2013

[9] F. Williksen. A Study of Deep Sea Mining Electrical Power System Topologies. Master's Thesis, NTNU, June 2017.

[10] R. N. Fard e E. Tedeschi, "Power System Design Considerations for a Seafloor Mining Vehicle", IEEE Energy Conversion Congress and Exposition (ECCE), pp. 1164 - 1171, 2018.

[11] R. N. Fard e E. Tedeschi, "Investigation of AC and DC power distributions to seafloor mining equipment", in *OCEANS 2017* - Aberdeen, Aberdeen, United Kingdom, 2017, p. 1–7.

[12] W. He, K. Uhlen, M. Hadiya, Z. Chen, G. Shi, and E. del Rio, "Case study of integrating an offshore wind farm with off-shore oil and gas platforms and with an onshore electrical grid," Journal of Renewable Energy, p. 10, 2013.

[13] "IEEE Recommended Practice for Electric Installations on Shipboard," IEEE Std 45-2002

[14] "IEEE Recommended Practice for 1 kV to 35 kV Medium-Voltage DC Power Systems on Ships", IEEE Std 1709-2018

[15] Margarida, A., J. Pimentel, E. Thibaut, and E. Cardoso. "High Voltage Subsea Pump–A Low Cost Subsea Boosting Enabler." In Offshore Technology Conference. Offshore Technology Conference, 2017.

[16] I. Lipton, E. Gleeson, p. Munro, "Preliminary Economic Assessment of the Solwara Project, Bismarck Sea, PNG - Nautilus Minerals, Technical Report, February 2018

[17] Jackson and D. Clarke, "Subsea Excavation of Seafloor Massive Sulphides," in OCEANS 2007, 2007, pp. 1-7.

[18] Liang, X. and Jackson, W.M., 2009. Influence of subsea cables on offshore power distribution systems. IEEE Transactions on Industry Applications, 45(6), pp.2136-2144.

[19] "Offshore Production System Definition and Cost Study - Nautilus Minerals, Study Report, June 2010.

[20] P. Jakobsen, G. Peck, and E. Snow, "Electrical power system challenges during the expansion of offshore oil & gas facilities," in Proc. of the 2012 Petroleum and Chemical Industry Conf. Europe (PCIC EUROPE), Prague, 2012, pp. 1-9.

[21] Offshore Energy Today, "Caterpillar Gensets for Russia's Largest Offshore Platform," Mar. 7, 2013.[Online].Available: https://www.offshoreenergytoday.com/caterpillar-gensets-for-russias-largest-off-shore-platform/

[22] K. Schipman, F. Delincé, "The importance of good power quality," ABB Review, 2010.

[23] Fard, R.N. and Tedeschi, E., 2018. Integration of distributed energy resources into offshore and subsea grids. CPSS Transactions on Power Electronics and Applications, 3(1), pp.36-45

[24] Herbich, J. B., 1978. Development of Offshore Mining. Houston, OTC.

[25] Knodt, S. et al., 2016. Development and Engineering of Offshore Mining Systems - State of the Art and Future Perspectives. Houston, OTC.

[26] Laugesen, J. et al., 2014. Seabed Mining - Guest Lecture at NTNU - TBA4145 Port and Coastal Facilities. Trondheim: DNV GL.

[27] D. S. Silva, Evaluation of the protection aspects of MVDC distribution to Subsea Grids, in ELK-23 Power Elctronics in Future Power Systems, June 2019, *not published.*

[28] A. Tessarolo, S. Castellan, R. Menis, and G. Sulligoi, "Electric generation technologies for all-electric ships with Medium-Voltage DC power distribution systems," in 2013 IEEE Electric Ship Technologies Symposium (ESTS), 2013, pp. 275-281

[29] Javaid, D. Dujić, and W. v. d. Merwe, "MVDC marine electrical distribution: Are we ready?," in IECON 2015 - 41st Annual Conference of the IEEE Industrial Electronics Society, 2015, pp. 000823-000828.

[30] Pei, O. Cwikowski, D. S. Vilchis-Rodriguez, M. Barnes, A. C. Smith, and R. Shuttleworth, "A review of technologies for MVDC circuit breakers," in IECON 2016 - 42nd Annual Conference of the IEEE Industrial Electronics Society, 2016, pp. 3799-3805.

[31] Williams, D. W., McBride, C. M., Kinnaman, S. C.: Deep ocean mining - technology transfer from and to the offshore drilling industry, Offshore Technology Conference, 2. – 5. May 1977, Houston, Texas, OTC-2775.

[32] B. Monsen, K. S. Rongve, T. Lægreid and C. Gutscher, "Åsgard Subsea Gas Compression—Technology Qualification Testing With High-Speed VSD and Very Long Step-Out Cable," in IEEE Transactions on Industry Applications, vol. 50, no. 2, pp. 1552-1561, March-April 2014.

[33] R. Roth, D. McLaurin, M. Paulin, M. McKee, S. Subramanian, C. Hume, V. Ponagandla, E. K. Albaugh, D. Davis, Status of Technologies and Systems - Worldwide Survey of Subsea Processing Conference, March 2018

[34] Control of Harmonics in Electrical Power Systems - ABS Guide notes, May 2006

[35] Giannoutsos, S.V. and Manias, S.N., 2015. A systematic power-quality assessment and harmonic filter design methodology for variable-frequency drive application in marine vessels. IEEE Transactions on industry applications.

[36] ABB XLPE Submarine Cable Systems - User guide, Revision 5.

[37] NEXANS Submarine cable 20kV 2XS(FL)2YRAA 3x1x120 RM/16 12/20(24)kV datasheet

[38] Beddard, A., and M. Barnes. "HVDC cable modelling for VSC-HVDC applications." In 2014 IEEE PES General Meeting Conference & Exposition, pp. 1-5. IEEE, 2014.

[39] National Grid, "2010 Offshore Development Information Statement Appendices," Company Report, 2010.

[40] T. Worzyk, Submarine Power Cables and Their Design Elements: Springer, 2009.

[41] Yang, J., O'Reilly, J. and Fletcher, J.E., 2010, December. An overview of DC cable modelling for fault analysis of VSC-HVDC transmission systems. In 2010 20th Australasian Universities Power Engineering Conference (pp. 1-5). IEEE.

[42] PSCAD/EMTDC online help, version 4.2.1, Manitoba, Canada.

[43] Fard, R.N., Eidsvik, O.A., Tedeschi, E. and Schølberg, I., 2018, May. Cable Selection Considerations for Subsea Vehicles. In 2018 OCEANS-MTS/IEEE Kobe Techno-Oceans (OTO) (pp. 1-8). IEEE.

[44] Song-Manguelle, J., Todorovic, M.H., Chi, S., Gunturi, S.K. and Datta, R., 2014. Power transfer capability of HVAC cables for subsea transmission and distribution systems. IEEE Transactions on Industry Applications, 50(4), pp.2382-2391.

[45] S. D'Arco, J. A. Suul and J. Beerten, "Analysis of accuracy versus model order for frequency-dependent Pi-model of HVDC cables," 2016 IEEE 17th Workshop on Control and Modeling for Power Electronics (COMPEL), Trondheim, 2016, pp. 1-8.

[46] ABB & Siemens Test Subsea Power Grids for Underwater Factories.
Available: https://spectrum.ieee.org/energy/fossil-fuels/abb-siemens-test-subsea-power-grids-for-underwater-factories

[47] Lendenmann, H., Laneryd, T., Virtanen, E., Cagienard, R., Wagner, T. and Missing, K., 2019, April. Shallow Water Testing of 9-12 MVA Variable Speed Drive for Subsea Installation. In Offshore Technology Conference. Offshore Technology Conference.

[48] T. Kalitjuka, Control of Voltage Source Converters for Power System Applications, Master Thesis, NTNU, June 2011.

[49] Bajracharya, C., Molinas, M., Suul, J. A., & Undeland, T. M. (2008). Understanding of tuning techniques of converter controllers for VSC-HVDC. In Nordic Workshop on Power and Industrial Electronics (NORPIE/2008), June 9-11, 2008, Espoo, Finland. Helsinki University of Technology.

[50] V. G. Agelidis, et al., "Recent Advances in High-Voltage Direct-Current Power Transmission Systems," in Industrial Technology, 2006. ICIT 2006. IEEE International Conference on, 2006, pp. 206-213.

[51] Du, Cuiqing. "The control of VSC-HVDC and its use for large industrial power systems", Licentiate thesis, Chalmers University of Technology, Goteborg. Sweden, April 2003.

[52] Shire, Tamiru Woldeyesus. "VSC-HVDC based network reinforcement", Master thesis, Delft University of Technology, Netherlands, May 2009, Delft.

[53] E. Tedeschi. "Lecture notes of the course ELK-23 Power Electronics in Future Power Systems", NTNU, August, 2018.

[54] Mohan, N. Underland, T.M. Robbins, W.P. "Power Electronics: Converters, Applications, and Design, 3rd edition, 2002.

[55] Asker, M. E., Kilic, H. "Modulation Index and Switching Frequency Effect on Symmetric Regular Sampled SPWM." European Journal of Technique 7.2 (2017): 102-109.

[56] Huang, A. Q., Zhu, Q., Wang, L., & Zhang, L. "15 kV SiC MOSFET: An enabling technology for medium voltage solid state transformers", CPSS Transactions on Power Electronics and Applications, 2(2), 118-130, (2017).

[57] Reddy, R., and B. Narasimharaju. "Enhanced closed loop voltage control of buck converter for improved performance", IEEE Annual IEEE India Conference (INDICON). 2014.

[58] Beerten, J., D'Arco, S., & Suul, J. A. "Frequency-dependent cable modelling for small-signal stability analysis of VSC-HVDC systems", IET Generation, Transmission & Distribution, 10(6), 1370-1381, (2016).

[59] Electromagnetic compatibility (EMC)—Part 4-7: Testing and Measurement Techniques General Guide on Harmonics and Interharmonics Measurements and Instrumentation, for Power Supply Systems and Equipment Connected Thereto, IEC Std. 61000-4-7, 2009.

[60] Zhang, H., N. Wheeler, and D. Grant. "Switching harmonics in the DC link current in a PWM AC-DC-AC converter." In IAS'95. Conference Record of the 1995 IEEE Industry Applications Conference Thirtieth IAS Annual Meeting, vol. 3, pp. 2649-2655. IEEE, 1995.

[61] Li, Lei, Puqi Ning, Zhuolin Duan, Dong Zhang, and Xuhui Wen. "A study on the effect of DC-link decoupling capacitors." In 2017 IEEE Transportation Electrification Conference and Expo, Asia-Pacific (ITEC Asia-Pacific), pp. 1-5. IEEE, 2017.

[62] Kolar, Johannw Walter, and Simon D. Round. "Analytical calculation of the RMS current stress on the DC-link capacitor of voltage-PWM converter systems." IEE Proceedings-Electric Power Applications 153, no. 4 (2006): 535-543.

[63] Chien, Chang Hsin, and Richard WG Bucknall. "Analysis of harmonics in subsea power transmission cables used in VSC–HVDC transmission systems operating under steady-state conditions." IEEE Transactions on Power Delivery 22, no. 4 (2007): 2489-2497.

[64] Wang, Wei. "The effect of ripple on the reliability of VSC-HVDC extruded cable systems." In 2018 12th International Conference on the Properties and Applications of Dielectric Materials (ICPADM), pp. 412-418. IEEE, 2018.

[65] Rendusara, D., E. Cengelci, P. Enjeti, and D. C. Lee. "An evaluation of the DC-link capacitor heating in adjustable speed drive systems with different utility interface options." In APEC'99. Fourteenth Annual Applied Power Electronics Conference and Exposition. 1999 Conference Proceedings (Cat. No. 99CH36285), vol. 2, pp. 781-787. IEEE, 1999.

[66] Beres, R. Narcis, X. Wang, M. Liserre, F. Blaabjerg, and C. L. Bak. "A review of passive power filters for three-phase grid-connected voltage-source converters." IEEE Journal of Emerging and Selected Topics in Power Electronics 4, no. 1 (2015): 54-69.

[67] Inductor Calculation for Buck Converter, ROHM Semiconductor.

[68] Shulin, L., Jian, L., Yinlin, Y., and Jiuming, Z. "Design of intrinsically safe buck dc/dc converters." In Proceedings of the Eighth International Conference on Electrical Machines & Systems (Vol. 9, pp. 1327-1331). Beijing: International Academic Publishers, World Publishing Corporation, 2005.

[69] Kumar, S., and Thakura, P. R. "Closed loop PI control of DC-DC Cascode Buck-Boost converter". In 2017 International Conference on Innovations in Information, Embedded and Communication Systems (ICIIECS) (pp. 1-6). IEEE.

[70] Blasko, Vladimir, and Vikram Kaura. "A new mathematical model and control of a three-phase AC-DC voltage source converter." IEEE transactions on Power Electronics 12, no. 1 (1997): 116-123.

[71] American Bureau of Shipping (ABS), Rules for Building and Classing Steel Vessels 2013 Part 4: Vessel Systems and Machinery.

[72] Mauseth, F., Amundsen, M., & Faremo, H. "Water tree growth of wet XLPE cables stressed with DC and high frequency AC voltage superimposed." In 2012 IEEE International Symposium on Electrical Insulation (pp. 266-269). IEEE. June 2012.

[73] Xu, L., Fan, L., and Miao, Z. "DC impedance-model-based resonance analysis of a VSC–HVDC system." IEEE Transactions on Power Delivery 30.3 (2014): 1221-1230.

[74] Bierhoff, M. H., Fuchs, F. W. "DC-link harmonics of three-phase voltage-source converters influenced by the pulsewidth-modulation strategy—An analysis." IEEE Transactions on Industrial Electronics 55.5 (2008): 2085-2092.

[75] Soltani, H., et al. "Effects of DC-link filter on harmonic and interharmonic generation in three-phase adjustable speed drive systems." 2017 IEEE Energy Conversion Congress and Exposition (ECCE). IEEE, 2017.

[76] Ayhan, U., Hava, A. M. "Analysis and characterization of DC bus ripple current of two-level inverters using the equivalent centered harmonic approach." 2011 IEEE Energy Conversion Congress and Exposition. IEEE, 2011.

[77] IEEE Std 242-2001, "Recommended Practice for Protection and Coordination of Industrial and Commercial Power Systems".

[78] W. Wang, "The effect of ripple on the reliability of VSC-HVDC extruded cable systems," 2018 12th International Conference on the Properties and Applications of Dielectric Materials (ICPADM), Xi'an, 2018, pp. 412-418.

[79] P. Romano et al., "Partial Discharge Measurements under DC Voltages Containing Harmonics Produced by Power Electronic Devices," 2018 IEEE Conference on Electrical Insulation and Dielectric Phenomena (CEIDP), Cancun, 2018, pp. 558-561

Appendix A

Per-Unit formulas

- S_{base}: Nominal 3-phase apparent power of the AC system.
- $V_{\text{LL,RMS}}$: Nominal phase-to-phase RMS voltage of the AC system.
- V_{base}: Nominal peak phase-to-ground voltage of the AC system
- I_{base}: Nominal peak phase current of the AC system.
- Z_{base}: Base impedance.
- ω_{base}: Base angular frequency.
- $V_{\text{DC,base}}$: Voltage at the converter DC-link
- $I_{\text{DC,base}}$: Base DC current.

$$\mathrm{V_{base}} = \frac{\sqrt{2}}{\sqrt{3}} \cdot \mathrm{V_{LL,RMS}} \tag{A.1}$$

$$\mathrm{I_{base}} = \frac{2}{3} \cdot \frac{\mathrm{S_{base}}}{\mathrm{V_{base}}} \tag{A.2}$$

$$\mathrm{Z_{base}} = \frac{\mathrm{V_{base}}}{\mathrm{I_{base}}} \tag{A.3}$$

$$\mathrm{V_{DC,base}} = 2 \cdot \mathrm{V_{base}} \tag{A.4}$$

$$\mathrm{I_{DC,base}} = \frac{\mathrm{S_{base}}}{\mathrm{V_{DC,base}}} \tag{A.5}$$

Appendix B

Simulink models

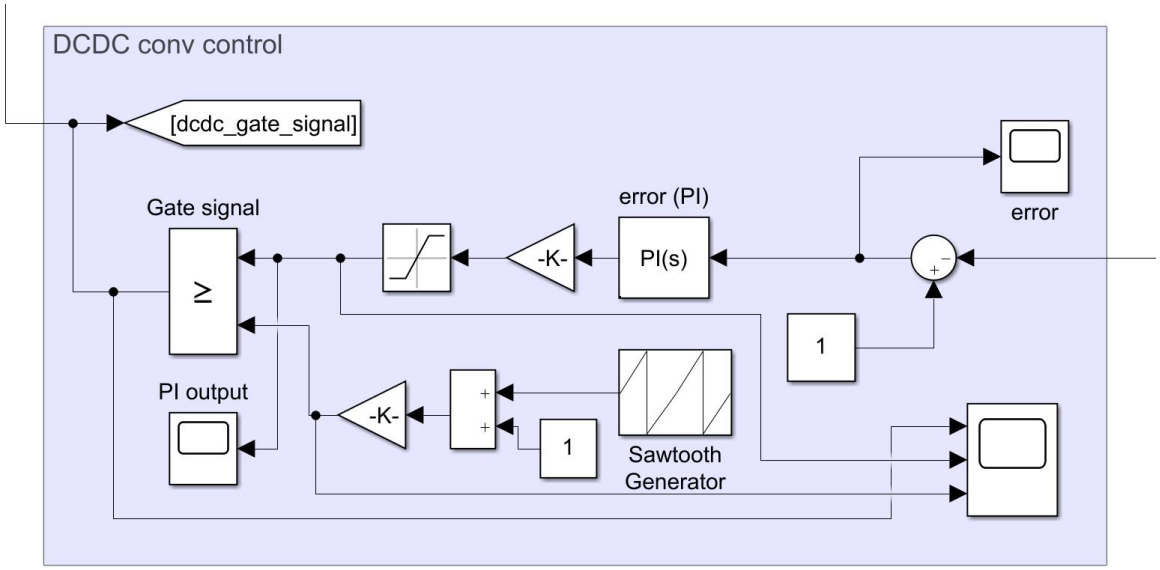

Figure B.1: Control loop for the buck converter

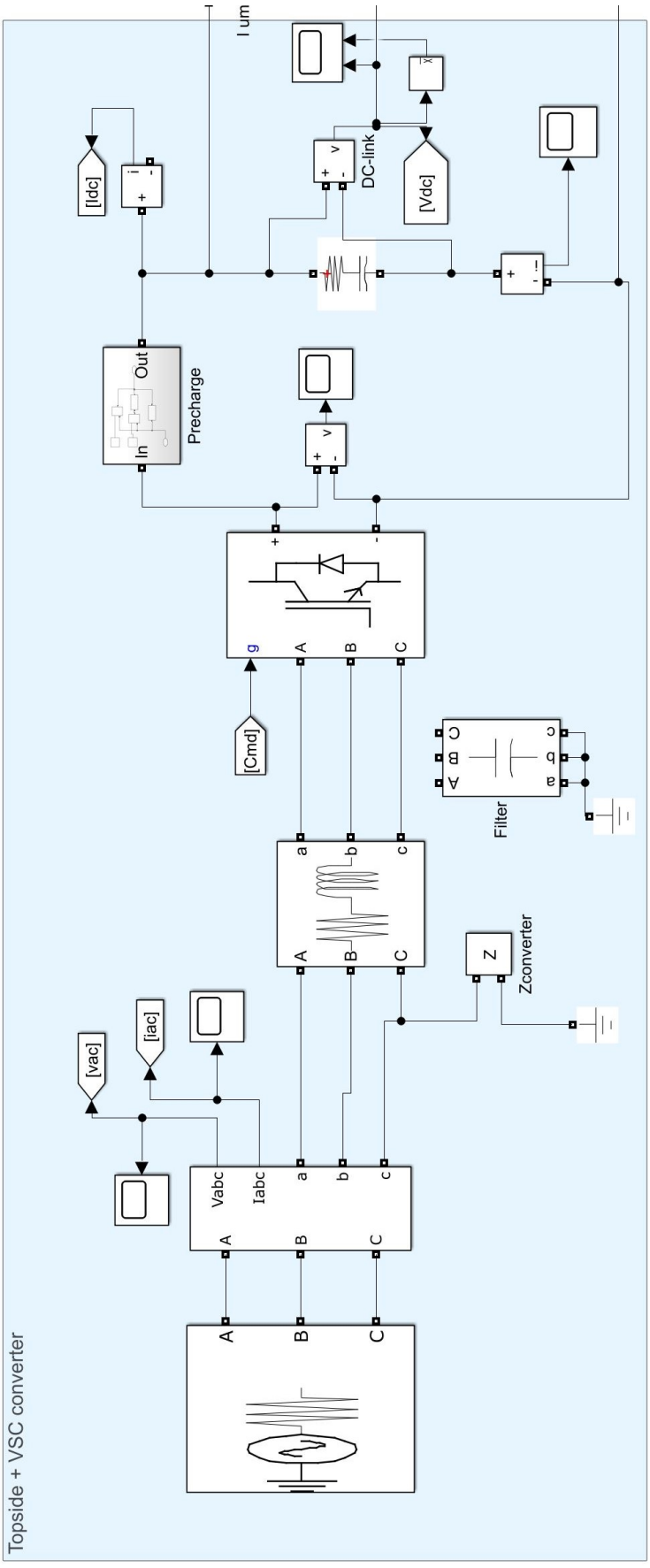

Figure B.2: Topside system

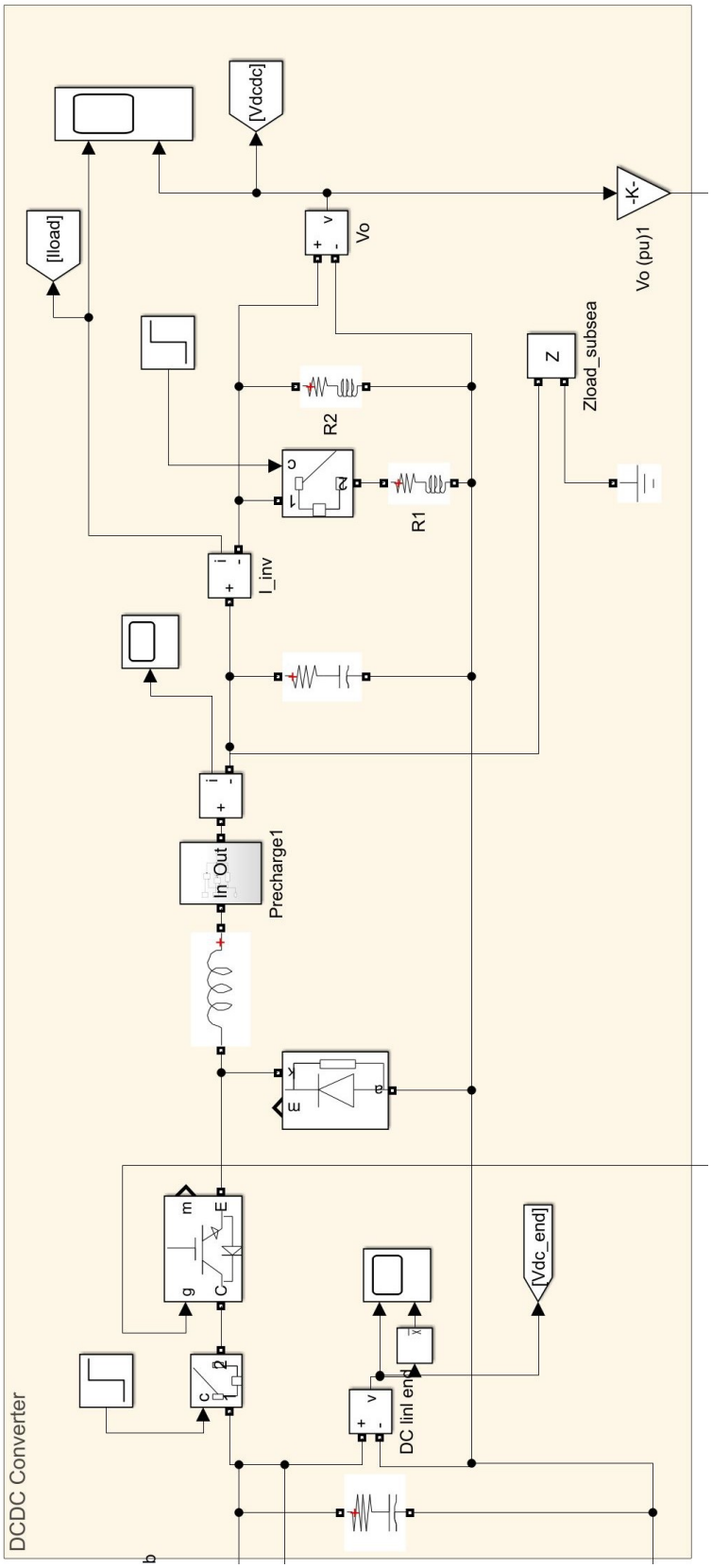

Figure B.3: Buck converter

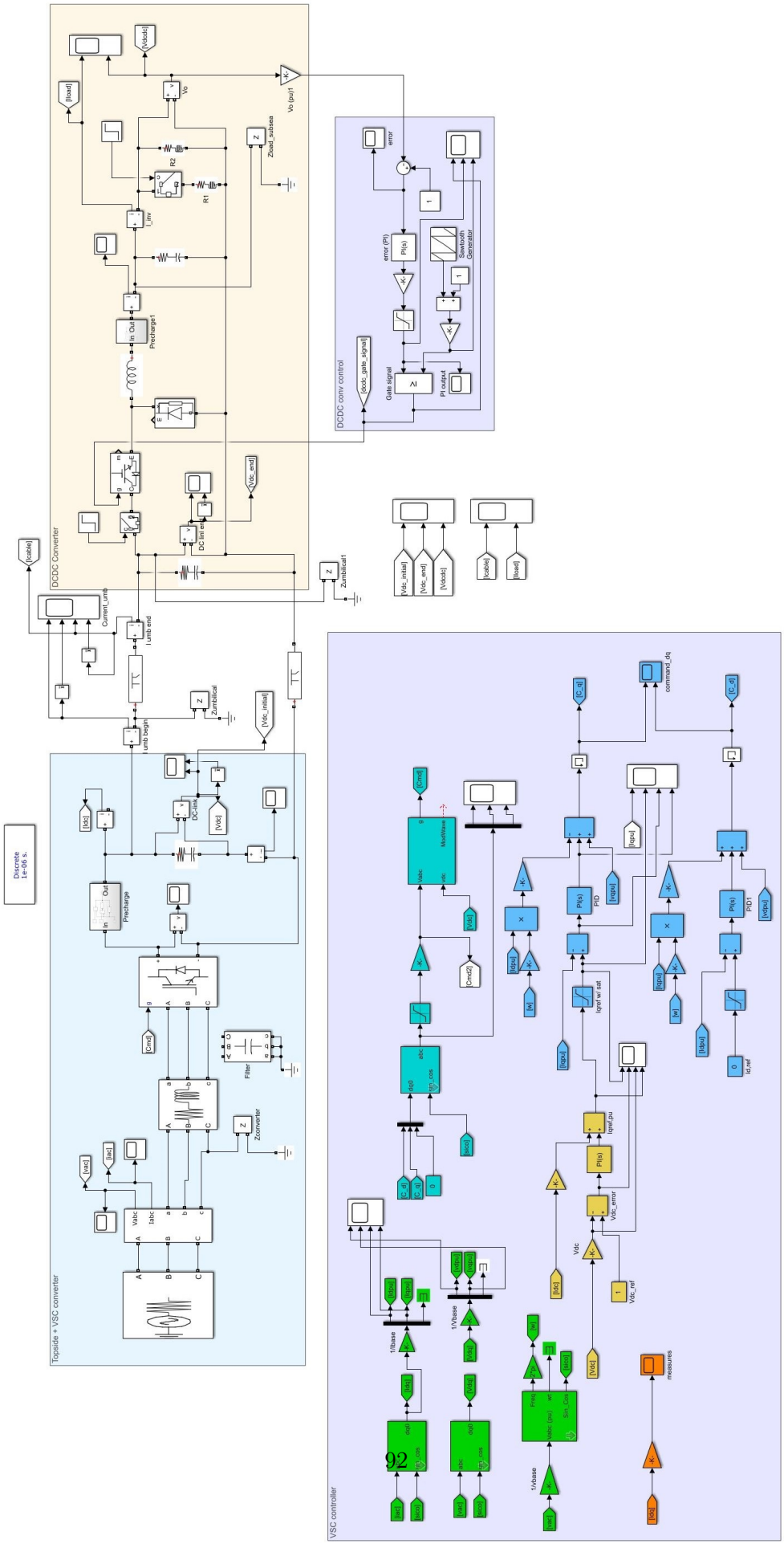

Figure B.4: Modeling of the total system

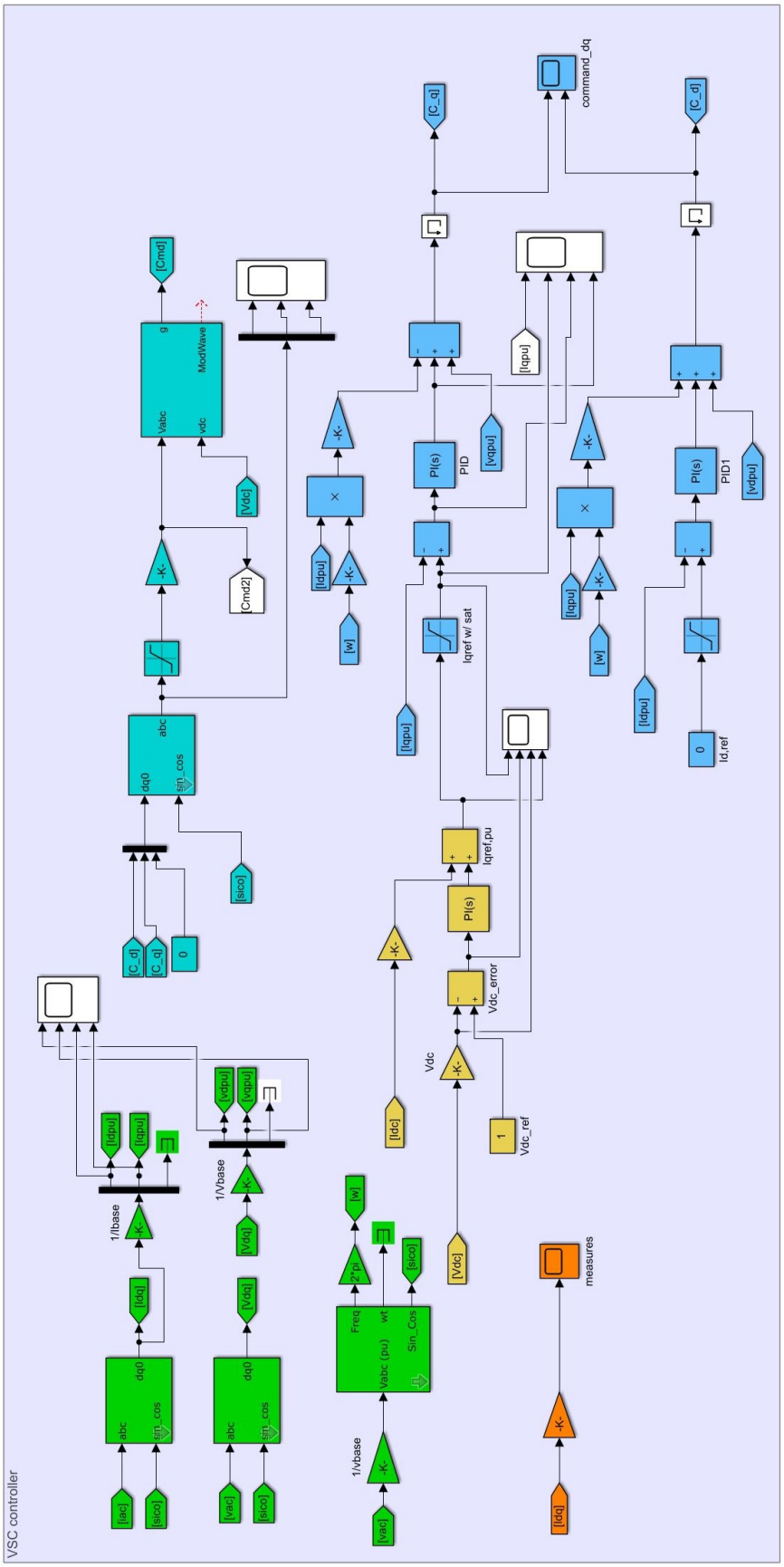

Figure B.5: 2L-VSC control

Appendix C

Bode plots for inner and outer control loops

C.1 Step response - Current control loop

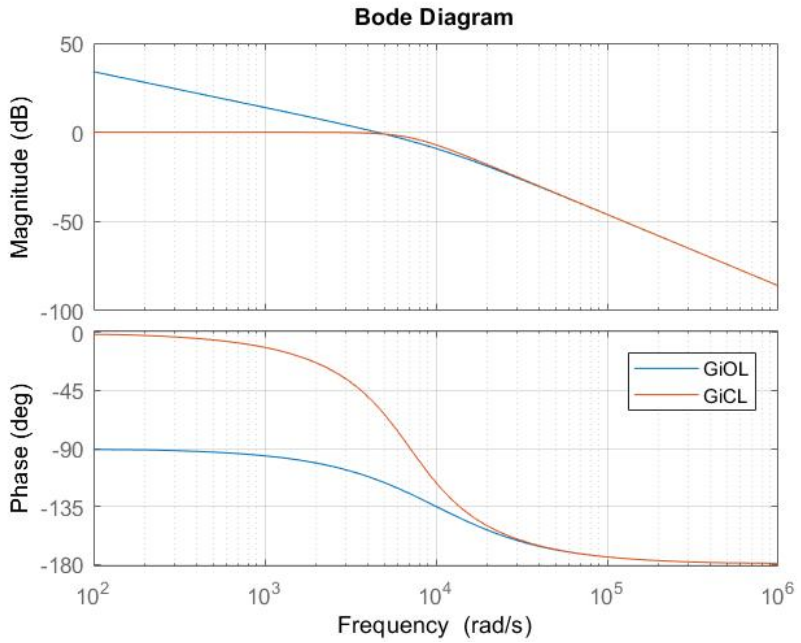

Figure C.1: Bode plot for the current control loop using Modulus Optimum.

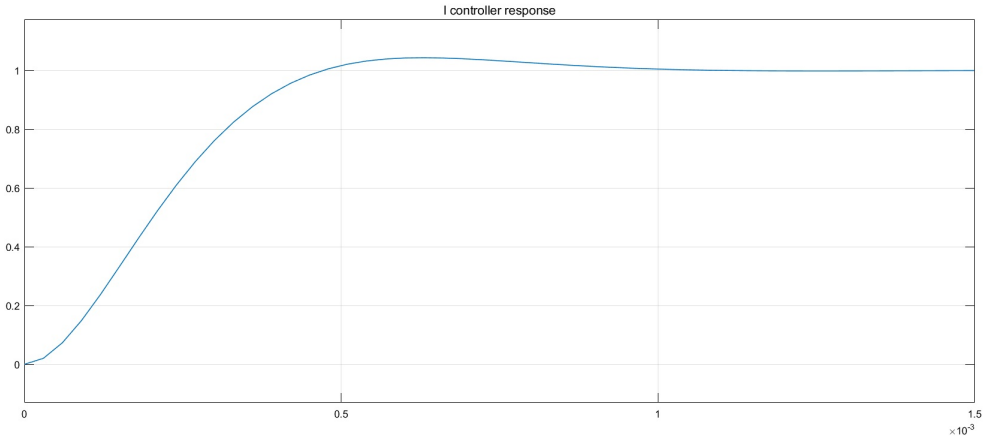

Figure C.2: Controller voltage response to a unity step signal.

C.2 Step response - Voltage control loop

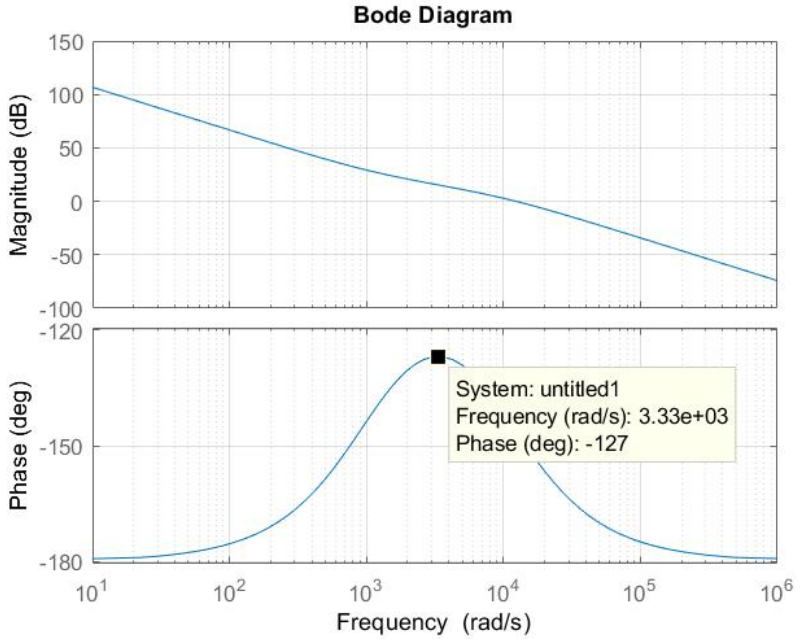

Figure C.3: Bode plot for the voltage control loop using Symmetrical Optimum.

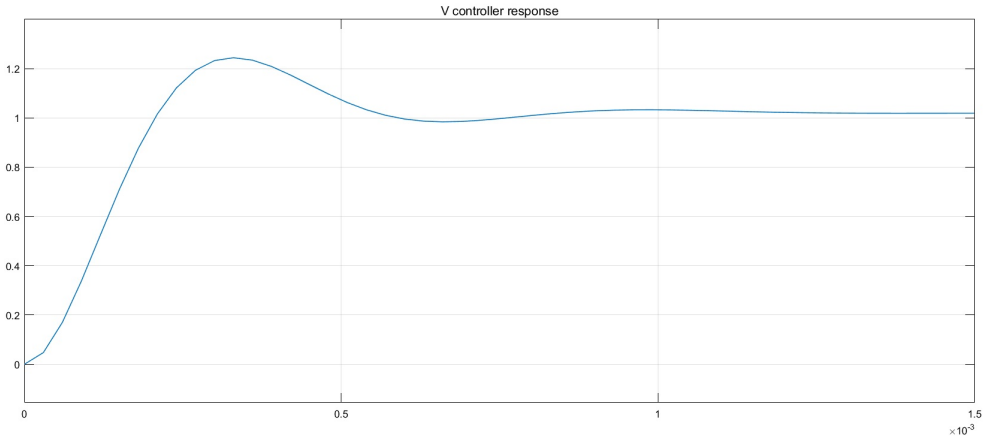

Figure C.4: Controller voltage response to a unity step signal.

Appendix D

Testing circuits for the VSC

D.1 VSC converter

The VSC converter control loops are tested before the implementation in the main system. The following sections elucidate how they have been tested.

D.1.1 Current control loop

The inner control loop must provide the signal to the PWM block, enabling the block to control the switching pattern of the converter switches. Once the PI parameters are defined, the current control loop can be tested by the circuit presented in the Figs. D.1 and D.3.

The command signals are transferred from dq rotating reference frame back to abc reference frame and used to control the voltage sources. The Fig. D.3 shows the output signals to be used in the PWM generator (see Fig. 4.13) when the input signals $I_{q,ref}$=1pu and $I_{d,ref}$=0 are used.

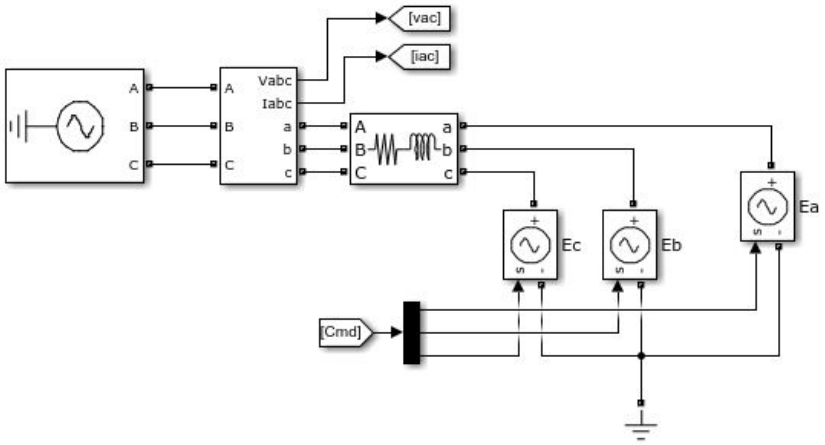

Figure D.1: Simulink testing model for the control loop.

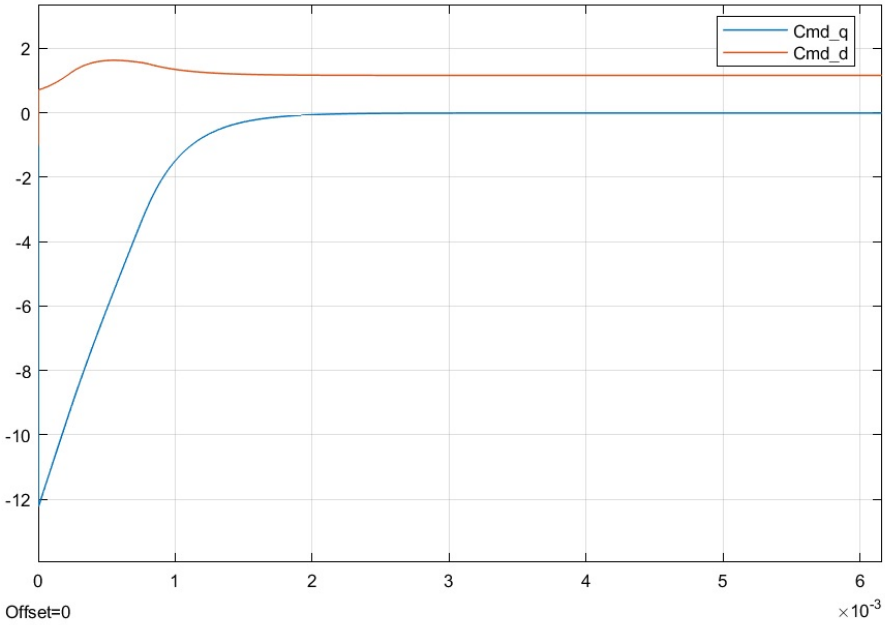

Figure D.2: Control signals from the current control loop as inputs to the PWM generator.

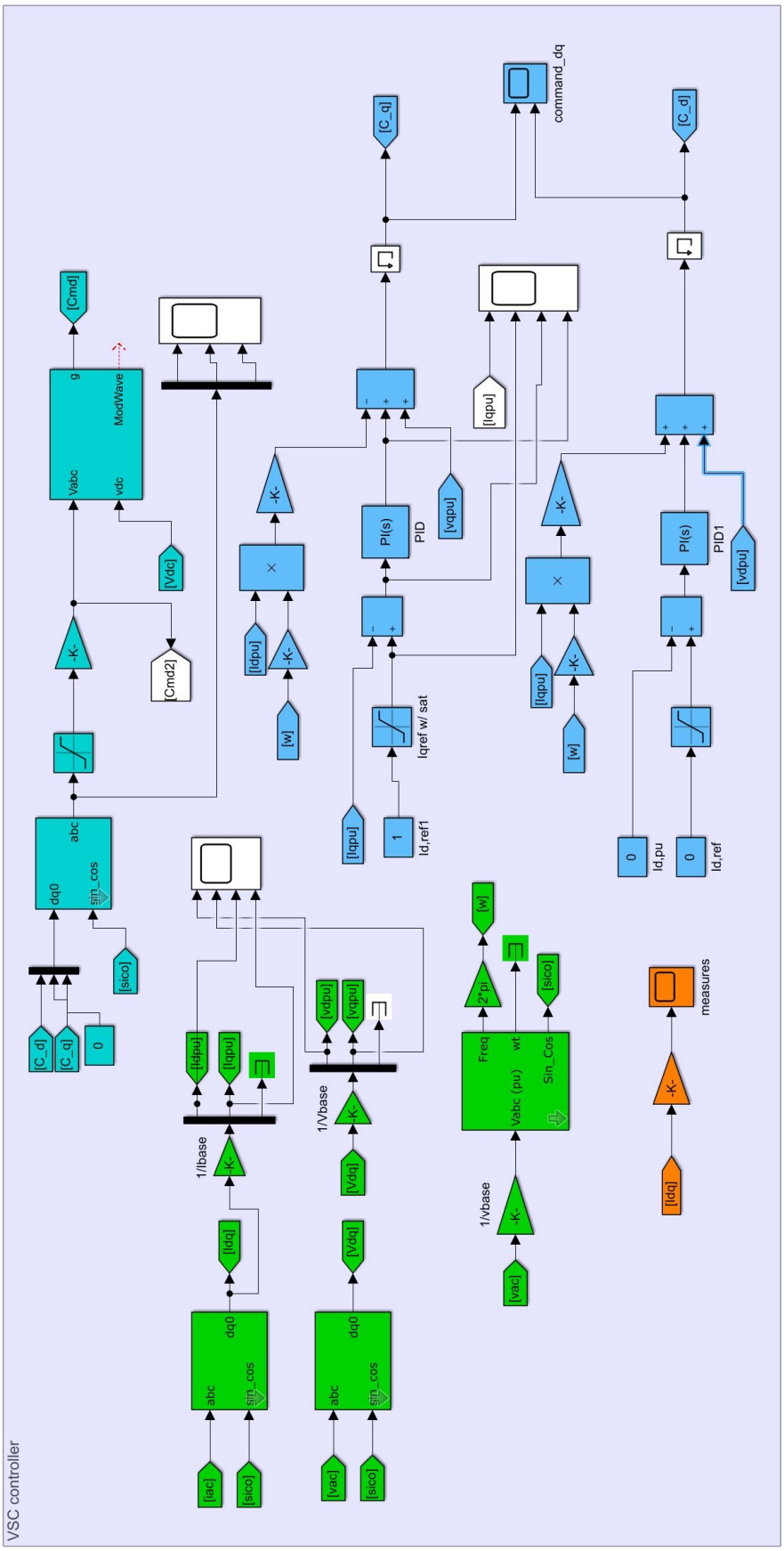

Figure D.3: Current loop test circuit (control.

D.1.2 Voltage control loop

The Fig. D.4 presents how to test the voltage control loop. A controlled DC current source, which is the output of the voltage controller, injects current towards the VSC DC-link capacitor in parallel with the load, which is a constant current source. The Fig. D.5 presents the control loop bringing the voltage at the DC-link successfully to the reference in per unit.

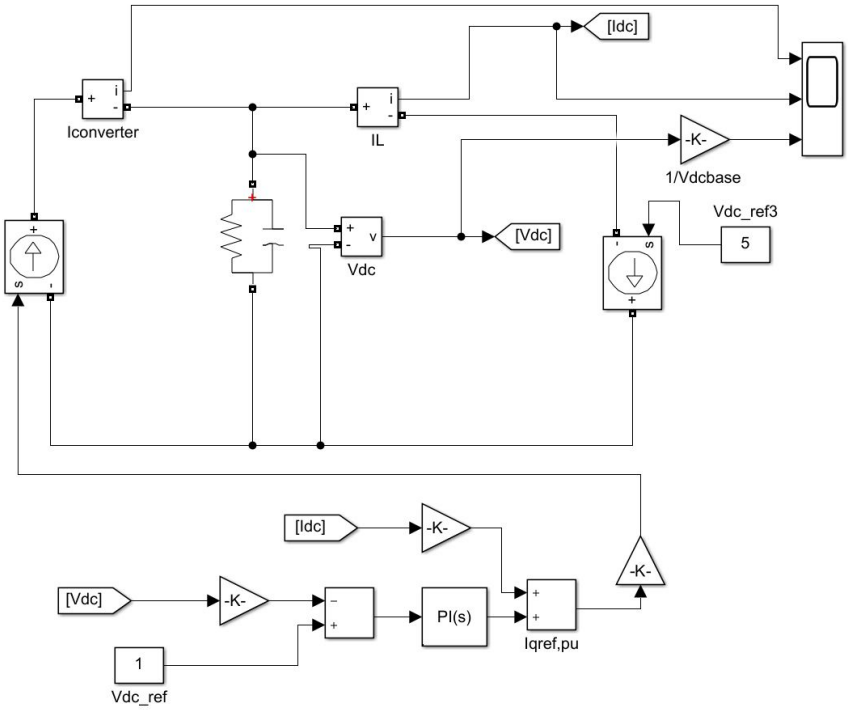

Figure D.4: Testing circuit for the voltage control loop.

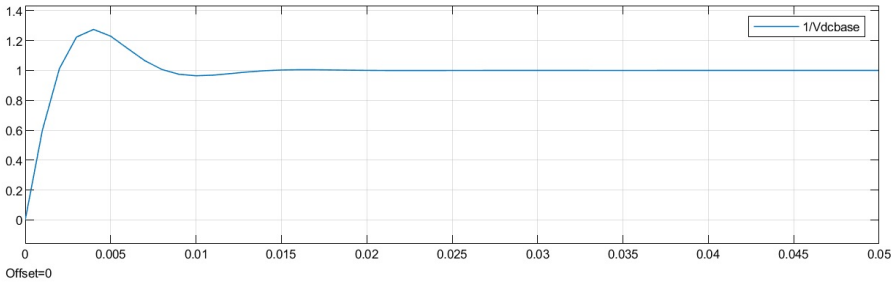

Figure D.5: Voltage control loop setting the voltage at the dc-link to the reference.

Appendix E

Submarine cable datasheet

CURRENT RATING FOR XLPE SUBMARINE CABLE SYSTEMS

The XLPE cable should at least have a conductor cross section adequate to meet the system requirements for power transmission capacity. The cost of energy losses can be reduced by using larger conductor.

Load losses in XLPE cables are primarily due to the ohmic losses in the conductor and the metallic screen. XLPE cables can be loaded continuously to a conductor temperature of 90°C.

The dielectric losses of XLPE insulation are present also at no load. Those losses depend on the operation voltage applied and shall be considered above 100 kV.

Dielectric losses in XLPE cables are lower than for EPR and fluid-filled cables.

The current rating of submarine cables follows the same rules as for land cables. However there are some differences:

- Three-core submarine cables usually have steel wire armour. Single-core cables have non-magnetic armour.
- Single-core cables can be laid separated or close. Close laying gives lower losses. Separation eliminates mutual heating but means higher losses in the armour. The induced current in the armour can be high, up to the same value as in the conductor.

Single-core cable with lead sheath and wire armour

Three-core cable with optic fibers, lead sheath and wire armour

Continuous current ratings for three-core submarine cables are given in Tables 33-34 and for single-core cables in Tables 35-36. The continuous current ratings are calculated according to IEC 60287 series of standards and with the following conditions:

- One three-core cable or one three-phase group of single-core cables
- Temperature in sea bed 20°C
- Laying depth in sea bed 1.0 m
- Sea bed thermal resistivity 1.0 K x m/W

Rating factors for sea bed temperature - see Tables 7-11 in the brochure "XLPE Land Cable Systems - User's guide".

Current rating for three-core submarine cables with steel wire armour

Table 33

10-90 kV XLPE 3-core cables		
Cross section mm²	Copper conductor	Aluminium conductor
	A	A
95	300	235
120	340	265
150	375	300
185	420	335
240	480	385
300	530	430
400	590	485
500	655	540
630	715	600
800	775	660
1000	825	720

Table 34

100-300 kV XLPE 3-core cables		
Cross section mm²	Copper conductor	Aluminium conductor
	A	A
300	530	430
400	590	485
500	655	540
630	715	600
800	775	660
1000	825	720

Figure E.1: Submarine Cable Datasheet 01

CURRENT RATING FOR XLPE SUBMARINE CABLE SYSTEMS

Current rating for single-core submarine cables

Table 35

Cross section Cu conductor	Rated voltage 10 - 90 kV	
	Wide spacing	Close spacing
mm²	A	A
95	410	315
120	465	355
150	520	395
185	585	435
240	670	495
300	750	545
400	840	610
500	940	670
630	1050	740
800	1160	805
1000	1265	870

Table 36

Cross section Cu conductor	Rated voltage 100 - 420 kV	
	Wide spacing	Close spacing
mm²	A	A
185	580	445
240	670	505
300	750	560
400	845	620
500	950	690
630	1065	760
800	1180	830
1000	1290	895

Note 1: Calculations were performed assuming single layer of 5 mm copper armour wire.
Note 2: Aluminium cables (conductor made of aluminum and armouring made of aluminium alloy) will have a rating of 75 to 80 % for the same conductor area.
Note 3: The rating data given in the above tables should be regarded as indicative only.
Note 4: Cross sections larger than 1000 mm² can be offered on request.

Figure E.2: Submarine Cable Datasheet 02

TECHNICAL DATA FOR XLPE SUBMARINE CABLE SYSTEMS

Single-core cables with lead sheath

Cross-section of conductor	Diameter of conductor	Insulation thickness	Diameter over insulation	Lead sheath thickness	Outer diameter of cable	Cable weight (Aluminium)	Cable weight (Copper)	Capacitance	Charging current per phase at 50 Hz	Inductance ●●●
mm²	mm	mm	mm	mm	mm	kg/m	kg/m	µF/km	A/km	mH/km

Table 37

Single-core cables, nominal voltage 220 kV (Um = 245 kV)										
500	26.2	24.0	77.6	2.9	111.0	19.1	29.3	0.14	5.8	1.42
630	29.8	23.0	79.2	3.0	112.8	20.0	31.2	0.16	6.4	1.40
800	33.7	23.0	83.1	3.1	117.5	21.9	34.5	0.17	6.9	1.37
1000	37.9	23.0	87.3	3.1	121.9	23.5	37.7	0.19	7.4	1.35
1200	41.2	23.0	90.6	3.1	125.2	24.8	40.4	0.20	7.8	1.33
1400	44.4	23.0	93.8	3.1	128.6	26.1	43.2	0.21	8.2	1.32
1600	47.4	23.0	96.8	3.1	131.8	27.5	46.0	0.22	8.6	1.31

Table 38

Single-core cables, nominal voltage 275 kV (Um = 300 kV)										
500	26.2	26.0	81.6	3.0	115.2	20.5	31.1	0.14	6.8	1.42
630	29.8	24.0	81.2	3.0	114.8	20.6	31.8	0.16	7.7	1.40
800	33.7	24.0	85.1	3.1	119.5	22.5	35.2	0.17	8.3	1.37
1000	37.9	24.0	89.3	3.1	123.9	24.1	38.4	0.18	9.0	1.35
1200	41.2	24.0	92.6	3.1	127.4	25.5	41.6	0.19	9.5	1.33
1400	44.4	24.0	95.8	3.1	130.6	26.8	44.4	0.20	10.0	1.32
1600	47.4	24.0	98.8	3.1	133.8	28.1	47.2	0.21	10.4	1.31

Table 39

Single-core cables, nominal voltage 330 kV (Um = 362 kV)										
630	29.8	28.0	89.2	3.1	123.4	23.3	35.2	0.14	8.8	1.40
800	33.7	27.0	91.1	3.1	125.9	24.3	37.5	0.15	9.7	1.37
1000	37.9	26.0	93.3	3.1	128.1	25.3	39.9	0.17	10.7	1.35
1200	41.2	25.0	94.6	3.1	129.4	26.1	42.0	0.18	11.1	1.33
1400	44.4	25.0	97.8	3.1	132.8	27.4	44.9	0.19	11.6	1.32
1600	47.4	25.0	100.8	3.1	135.8	28.7	47.7	0.20	12.1	1.31

Table 40

Single-core cables, nominal voltage 400 kV (Um = 420 kV)										
630	29.8	32.0	98.2	3.1	132.8	26.1	38.8	0.13	9.6	1.40
800	33.7	30.0	98.1	3.1	133.1	26.5	40.2	0.15	10.7	1.37
1000	37.9	29.0	100.3	3.1	135.3	27.5	42.6	0.16	11.7	1.35
1200	41.2	27.0	99.6	3.1	134.6	27.7	44.0	0.18	12.9	1.33
1400	44.4	27.0	102.8	3.1	138.0	29.0	46.9	0.19	13.5	1.32
1600	47.4	27.0	105.8	3.1	141.0	30.4	49.7	0.19	14.1	1.31

Figure E.3: Submarine Cable Datasheet 03

TECHNICAL DATA FOR XLPE SUBMARINE CABLE SYSTEMS

Three-core cables with copper wire screen

Cross-section of conductor	Diameter of conductor	Insulation thickness	Diameter over insulation	Cross section of screen	Outer diameter of cable	Cable weight (Aluminium)	Cable weight (Copper)	Capacitance	Charging current per phase at 50 Hz	Inductance
mm²	mm	mm	mm	mm²	mm	kg/m	kg/m	µF/km	A/km	mH/km
Table 41										
Three-core cables, nominal voltage 10 kV (Um = 12 kV)										
70	9.6	3.4	18.8	16	80.7	13.7	15.0	0.31	0.6	0.41
95	11.2	3.4	20.4	16	84.2	14.4	16.2	0.34	0.6	0.39
120	12.6	3.4	21.8	16	87.2	14.9	17.2	0.37	0.7	0.37
150	14.2	3.4	23.4	16	90.6	15.7	18.5	0.40	0.7	0.36
185	15.8	3.4	25.0	16	94.1	16.5	19.9	0.44	0.8	0.35
240	18.1	3.4	27.3	16	99.1	17.7	22.2	0.48	0.9	0.33
300	20.4	3.4	29.6	16	104.0	18.9	24.5	0.53	1.0	0.32
400	23.2	3.4	32.4	16	110.1	20.8	28.2	0.59	1.1	0.31
500	26.2	3.4	35.8	16	117.4	22.7	32.1	0.66	1.2	0.30
Table 42										
Three-core cables, nominal voltage 20 kV (Um = 24 kV)										
70	9.6	5.5	23.0	16	89.8	15.1	16.4	0.21	0.8	0.44
95	11.2	5.5	24.6	16	93.2	15.8	17.6	0.23	0.9	0.41
120	12.6	5.5	26.0	16	96.2	16.6	18.8	0.25	0.9	0.40
150	14.2	5.5	27.6	16	99.7	17.3	20.1	0.27	1.0	0.38
185	15.8	5.5	29.2	16	103.2	18.2	21.6	0.29	1.1	0.37
240	18.1	5.5	31.5	16	108.1	19.3	23.7	0.32	1.2	0.35
300	20.4	5.5	33.8	16	113.1	20.6	26.2	0.35	1.3	0.34
400	23.2	5.5	36.6	16	119.1	22.5	29.9	0.39	1.4	0.33
500	26.2	5.5	40.0	16	126.5	24.5	33.8	0.43	1.6	0.32
630	29.8	5.5	43.6	16	134.3	26.7	38.5	0.48	1.7	0.31
Table 43										
Three-core cables, nominal voltage 30 kV (Um = 36 kV)										
70	9.6	8.0	28.0	16	100.6	16.9	18.2	0.16	0.9	0.46
95	11.2	8.0	29.6	16	104.0	17.7	19.5	0.18	1.0	0.44
120	12.6	8.0	31.0	16	107.0	18.4	20.7	0.19	1.0	0.42
150	14.2	8.0	32.6	16	110.5	19.3	22.1	0.21	1.1	0.41
185	15.8	8.0	34.2	16	114.0	20.1	23.6	0.22	1.2	0.39
240	18.1	8.0	36.5	16	118.9	21.4	25.9	0.24	1.3	0.38
300	20.4	8.0	38.8	16	123.9	22.6	28.2	0.26	1.4	0.36
400	23.2	8.0	41.6	16	129.9	24.6	32.0	0.29	1.6	0.35
500	26.2	8.0	45.0	16	137.3	26.7	36.0	0.32	1.7	0.34
630	29.8	8.0	48.6	16	145.1	29.2	40.9	0.35	1.9	0.32
800	33.7	8.0	52.5	16	154.4	32.2	47.2	0.38	2.1	0.31

Figure E.4: Submarine Cable Datasheet 04

TECHNICAL DATA FOR XLPE SUBMARINE CABLE SYSTEMS

Three-core cables with lead sheath

Cross-section of conductor	Diameter of conductor	Insulation thickness	Diameter over insulation	Lead sheath thickness	Outer diameter of cable	Cable weight (Aluminium)	Cable weight (Copper)	Capacitance	Charging current per phase at 50 Hz	Inductance
mm^2	mm	mm	mm	mm	mm	kg/m	kg/m	µF/km	A/km	mH/km

Table 44

Three-core cables, nominal voltage 45 kV (Um = 52 kV)										
95	11.2	8.0	29.6	1.3	109.0	19.1	20.8	0.18	1.5	0.43
120	12.6	8.0	31.0	1.3	112.0	20.0	22.3	0.19	1.6	0.42
150	14.2	8.0	32.6	1.4	116.0	21.6	24.4	0.21	1.6	0.40
185	15.8	8.0	34.2	1.4	119.0	22.7	26.2	0.22	1.8	0.39
240	18.1	8.0	36.5	1.5	124.0	25.0	29.5	0.24	2.0	0.37
300	20.4	8.0	38.8	1.6	130.0	27.3	32.9	0.26	2.2	0.36
400	23.2	8.0	41.6	1.7	136.0	30.4	37.9	0.29	2.3	0.35
500	26.2	8.0	45.0	1.8	144.0	33.8	43.2	0.32	2.6	0.33
630	29.8	8.0	48.6	1.9	152.0	37.8	49.7	0.35	2.9	0.32
800	33.7	8.0	52.5	2.1	162.0	43.5	58.6	0.38	3.1	0.31
1000	37.9	8.0	57.3	2.2	173.0	49.3	68.1	0.42	3.5	0.30

Table 45

Three-core cables, nominal voltage 66 kV (Um = 72.5 kV)										
95	11.2	9.0	31.6	1.3	113.0	19.8	21.6	0.17	2.0	0.44
120	12.6	9.0	33.0	1.4	116.0	21.6	23.8	0.18	2.1	0.43
150	14.2	9.0	34.6	1.4	120.0	22.9	25.7	0.19	2.3	0.41
185	15.8	9.0	36.2	1.4	124.0	24.5	28.0	0.20	2.4	0.40
240	18.1	9.0	38.5	1.6	129.0	26.8	31.3	0.22	2.6	0.38
300	20.4	9.0	40.8	1.6	134.0	28.7	34.3	0.24	2.8	0.37
400	23.2	9.0	43.6	1.7	141.0	31.7	39.2	0.26	3.1	0.35
500	26.2	9.0	47.0	1.9	149.0	36.0	45.4	0.29	3.5	0.34
630	29.8	9.0	50.6	2.0	157.0	40.1	52.0	0.32	3.7	0.33
800	33.7	9.0	54.5	2.1	167.0	45.1	60.1	0.35	4.1	0.32
1000	37.9	9.0	59.3	2.3	178.0	51.8	70.7	0.38	4.6	0.31

Table 46

Three-core cables, nominal voltage 110 kV (Um = 123 kV)										
185	15.8	16.0	50.2	2.0	156.0	37.4	40.9	0.14	2.8	0.46
240	18.1	15.0	50.5	2.0	157.0	38.0	42.5	0.15	3.0	0.43
300	20.4	14.0	50.8	2.0	157.0	38.5	44.1	0.17	3.5	0.41
400	23.2	13.0	51.6	2.0	159.0	39.7	47.2	0.20	3.9	0.38
500	26.2	13.0	55.0	2.1	167.0	43.6	53.0	0.22	4.3	0.37
630	29.8	13.0	58.6	2.3	176.0	48.8	60.7	0.24	4.7	0.36
800	33.7	13.0	62.5	2.4	185.0	54.4	69.5	0.26	5.2	0.34
1000	37.9	13.0	67.3	2.6	197.0	61.6	80.5	0.28	5.6	0.33

Figure E.5: Submarine Cable Datasheet 05